Title: Characterization of the cellular components of mouse collecting lymphatic vessels reveals that lymphatic muscle cells are the innate pacemaker cells regulating lymphatic contractions

Authors: S.D. Zawieja[1], G.A. Pea[1], S.E. Broyhill[1], A. Patro[1], K.H. Bromert[1], C. E. Norton[1], H. J. Kim[1], S. K. Sivasankaran[2], M. Li[1], J.A. Castorena-Gonzalez[3], B.T. Drumm[4], and M.J. Davis[1]

[1]Dept. of Medical Pharmacology & Physiology, University of Missouri, Columbia, Missouri.
[2]Bioinformatics and Analytics Core, Division of Research, Innovation and Impact, University of Missouri, Columbia, Missouri.
[3]Dept. of Pharmacology, Tulane University, New Orleans, Louisiana.
[4]Smooth Muscle Research Centre, Dundalk Institute of Technology, Dundalk, Co. Louth, A91 K584, Ireland.

Correspondence:
Michael J. Davis, PhD
Department of Medical Pharmacology and Physiology
One Hospital Drive
MA415 Medical Sciences Building
University of Missouri
Columbia, MO 65212
Tel: 573-884-5181
Fax: 573-884-4276
davismj@health.missouri.edu

Co-Correspondence:
Scott Zawieja PhD
Department of Medical Pharmacology and Physiology
One Hospital Drive
MA415 Medical Sciences Building
University of Missouri
Columbia, MO 65212
Tel: 573-882-8069
Fax: 573-884-4276
zawiejas@health.missouri.edu

Running title: Lymphatic Muscle as Innate Pacemaker Cells

Impact: The presence and functionality of proposed pacemaker cells in collecting lymphatic vessels was tested with various mouse Cre models to drive expression of a recombination reporter ROSA26mT/mG, a genetically encoded Ca^{2+} sensor GCaMP6f, or the optogenetic tool channel-rhodopsin2. Lymphatic $CD34^{+}$ adventitial cells co-express $PDGFRa^{+}$ while vessel-associated $cKit^{+}$ cells are mast cells; and neither cell type demonstrated pacemaking capability. *Myh11CreER*^{T2} identified lymphatic muscle cells that exhibited pacemaker behaviors such as pressure-dependent depolarization and calcium events during diastole and propagated contraction waves induced by focal, optical stimulation of channel-rhodopsin2.

Abbreviations: Ano1, Anoctamin 1; ChR2, channel rhodopsin; cLV, collecting lymphatic vessel; IALV, Inguinal Axillary Lymphatic Collecting Vessel; ICC, Interstitial Cell of Cajal; ICLC, Interstitial Cell of

Cajal Like Cell; LEC, Lymphatic Endothelial Cell; LMC, Lymphatic Muscle Cell; STDs, Spontaneous transient depolarizations; STMs, Spatio-Temporal Maps

Keywords: Lymphatic collecting vessel, lymphatic muscle cell, pacemaking, interstitial cells of Cajal like cells, mesenchymal stem cells

Abstract

Collecting lymphatic vessels (cLVs) exhibit spontaneous contractions with a pressure-dependent frequency, but the identity of the lymphatic pacemaker cell is still debated. By analogy to pacemakers in the GI and lower urinary tracts, proposed cLV pacemaker cells include interstitial cells of Cajal like cells (ICLC) or the lymphatic muscle (LMCs) cells themselves. Here we combined immunofluorescence and scRNAseq analyses with electrophysiological methods to examine the cellular constituents of the mouse cLV wall and assess whether any cell type exhibited morphological and functional processes characteristic of pacemaker cells: a continuous if not contiguous network integrated into the electrical syncytium; spontaneous Ca^{2+} transients; and depolarization-induced propagated contractions. We employed inducible Cre (iCre) mouse models routinely used to target these specific cell populations including: c-kitCreER^{T2} to target ICLC; *PdgfrβCreER*^{T2} to target pericyte-like cells; *PdgfrαCreER*^{TM} to target CD34^{+} adventitial cells and ICLC; and *Myh11CreER*^{T2} to target LMCs directly. These specific inducible Cre lines were crossed to the fluorescent reporter ROSA26mT/mG, the genetically encoded Ca^{2+} sensor GCaMP6f, and the light-activated cation channel rhodopsin2 (ChR2). c-KitCreER^{T2} labeled both a sparse population of LECs and round adventitial cells that responded to the mast cell activator compound 48-80. *PdgfrβCreER*^{T2} drove recombination in both adventitial cells and LMCs, limiting its power to discriminate a pericyte-specific population. *PdgfrαCreER*^{TM} labeled a large population of interconnected, oak leaf-shaped cells primarily along the adventitial surface of the vessel. Of these cells, only LMCs consistently, but heterogeneously, displayed spontaneous Ca^{2+} events during the diastolic period of the contraction cycle, and whose frequency was modulated in a pressure-dependent manner. Optogenetic depolarization through the expression of ChR2 under control of *Myh11CreER*^{T2}, but not *PdgfrαCreER*^{TM} or c-KitCreER^{T2}, resulted in propagated contractions upon photo-stimulation. Membrane potential recordings in LMCs demonstrated that the rate of diastolic depolarization significantly correlated with contraction frequency. These findings support the conclusion that LMCs, or a subset of LMCs, are responsible for mouse cLV pacemaking.

Introduction

The spontaneous contractions of collecting lymphatic vessels (cLV) are an integral component to fluid and macromolecule homeostasis as they provide the force to transport fluid from the interstitial spaces back to the blood circulation (Scallan et al., 2016). In humans, spontaneous contractile activity is estimated to account for 2/3 of lymph transport (Engeset et al., 1977) and this function is significantly compromised in patients suffering from lymphedema, whose cLVs typically display weak and irregular or entirely absent contractile activity (Olszewski, 2002). *Ex vivo* studies, in which the intraluminal pressure can be precisely controlled, have refined our understanding of the pressure-dependent regulation of contraction frequency (Benoit et al., 1989; Gashev et al., 2004), with some mouse cLVs displaying a 10-fold increase in contraction frequency over a 10 cmH_2O pressure gradient (Scallan and Davis, 2013; Zawieja et al., 2018a). The observation that cLVs, often cannulated at various lengths for *ex vivo* preparations, retain a consistently tunable contraction frequency points to the presence of a pacemaker cell(s) innate to the structure of the cLV wall and with a seemingly ubiquitous presence along the length of the vessel (Zawieja et al., 1993; Castorena-Gonzalez et al., 2018b). Furthermore, isolated cLVs typically display single pacemaker initiation sites unless damaged or electrically uncoupled by pharmacological inhibition of gap junctions or genetic deletion of *Gjc1* (Connexin 45, Cx45) (Behringer et al., 2017; Castorena-Gonzalez et al., 2018b; Castorena-Gonzalez et al., 2020). In sum, this suggests the pacemaker cell(s) is(are) likely both ubiquitous and continuous, to allow for electrical conduction via gap

junctions, along the length of the cLV and prevent colliding contractile waves which would impair lymph transport.

Investigations into the cLV pacemaker identity have focused largely on cells termed interstitial cells of Cajal like cells (ICLC; or telocytes) (McCloskey et al., 2002; Briggs Boedtkjer et al., 2013), as they display some morphological and cell marker expression profiles similar to the interstitial cells of Cajal (ICC), which are bona fide pacemakers in the gastrointestinal (GI) tract. ICC are classically identified by either methylene blue staining and expression of cKit, and coordinate GI smooth muscle contraction (Maeda et al., 1992; Ward et al., 1994; Ordog et al., 1999). ICC also express the canonical Ca^{2+} activated chloride channel Anoctamin 1 (Ano1) (Gomez-Pinilla et al., 2009), which is required for pacemaker activity (Hwang et al., 2009; Zhu et al., 2009; Singh et al., 2014). Previous reports in sheep mesenteric lymphatic vessels identified a population of $cKit^{+}$, $vimentin^{+}$, ICLC in the vessel wall between the endothelial and LMC layer and running along the axis of the vessel (McCloskey et al., 2002). Investigations in the human thoracic duct also identified a significant population of ICLC in close proximity to the lymphatic muscle cells (LMCs) evident by methylene blue staining, immunostaining for CD34, vimentin, and cKit, as well as the gold standard of electron microscopy (Briggs Boedtkjer et al., 2013). However, neither study could determine if these cells had functional electrical communication with the LMCs or demonstrate either a membrane electrical clock or internal Ca^{2+} clock to drive the rhythmic lymphatic vessel contractions observed *ex vivo*. LMCs share a functional similarity to ICC in that they also display the *Ano1* mediated Ca^{2+} activated chloride current (Van Helden, 1993; Toland et al., 2000; Mohanakumar et al., 2018) (Zawieja et al., 2019), that regulates pacemaking. Spontaneous transient depolarizations, presumably Ano1 dependent, were recorded in mesenteric cLVs from guinea pigs (Van Helden, 1993; von der Weid et al., 2008) providing a mechanism for membrane potential instability to drive AP initiation. Furthermore, computational models have proposed LMC sarcoplasmic reticulum (SR) Ca^{2+} release as the oscillator mechanism driving pacemaking (Imtiaz et al., 2007). SR Ca^{2+} release has also been implicated in pericyte regulation of arterioles (Hashitani et al., 2015; van Helden and Imtiaz, 2019), in microvascular vasomotion (Boedtkjer et al., 2008; Aalkjaer et al., 2011; van Helden and Imtiaz, 2019), and in the contraction waves of atypical muscle cells of the lower urinary tract (Grainger et al., 2022).

Presently, no investigations have clearly identified the cellular identities of possible pacemaker cells within the cLVs of the mouse. Mouse cLVs exhibit contractile parameters and conduction speed equivalent to those of human vessels (Castorena-Gonzalez et al., 2018b) and their simplified architecture, compared to larger mammals, in combination with the genetic tools developed for the mouse model, allowed us to test for a fundamental pacemaker cell in the cLV. In this study we utilized multiple genetic mouse models, confocal imaging of fluorescent reporters, cell specific expression of GCaMP6f for Ca^{2+} imaging, and optogenetic light-activated depolarization to both visualize and test the functional aspects of putative pacemaker cells, and membrane potential recordings in LMCs in pressure-challenged cLVs. We also performed immunostaining and single cell RNA sequencing (scRNAseq) of isolated cLVs to provide greater detail to the heterogenous cellular populations found within the mouse cLVs. Despite identifying a significant population of $CD34^{+}Pdgfr\alpha^{+}$ adventitial cells along the length of mouse cLVs, the results of our functional studies support a myogenic origin of pacemaking in cLVs.

Results

Methylene Blue Staining Reveals a Minor Population of Cells in Mouse cLVs

Methylene blue staining was used to identify an ICLC population in the human lymphatic thoracic duct (Briggs Boedtkjer et al., 2013). In our isolated and cleaned lymphatic inguinal axillary collecting vessels (IALVs), methylene blue stained a significant number of cells with variable density along the length of the IALV and heterogenous cell morphologies (Figure 1A-C). A significant portion of the stained cells resembled lymphatic vessel-associated macrophages with an elongated shape, while other cells were smaller and circular (Figure 1D-F). Methylene blue also appeared to stain mast cells as there were large ovoid cells on the adventitia of the vessel with intracellular granules. In addition, methylene blue stained a minor population of cells that exhibited long and thin axon-like extensions

154 which appeared to have a slight helical orientation, with a small central body and nucleus (Figure 1C).
155 None of these cell populations were aligned with the longitudinal axis of the vessel that would permit
156 efficient coupling or regulation across the circumferential LMCs required for coordinated propagation
157 along the length of the vessel.
158
159 **Immunofluorescence Imaging of IALVs Stained for ICLC, LEC, and LMC Markers**
160 We next stained IALVs for the putative telocyte/ICLC markers cKIT, CD34, and the intermediate
161 filament Vimentin, which have been previously utilized for ICLC identification in human and sheep
162 lymphatic tissues (McCloskey et al., 2002; Briggs Boedtkjer et al., 2013). Additionally, an antibody to the
163 intermediate filament Desmin was used to label muscle cells (McCloskey et al., 2002). IALVs stained
164 with cKIT (Figure 2B) showed robust signal in large ovoid cells with a non-segmented circular nucleus
165 (Figure 2A), characteristic of mast cells that were located in the outer part of the adventitia. Similarly,
166 cKIT stained populations of elongated cells as well as circular cells with variable densities throughout the
167 IALV wall, similar to methylene blue^{+} cell populations (Figure 2B, J). Staining for CD34 revealed a large
168 population of cells that were seemingly contiguous along the length of the vessel. The CD34^{+} cells
169 generally had multiple lobular processes and a "oak leaf" like appearance, typically a characteristic of
170 fibroblasts, though some contained short, thin dendrite-like extensions (Figure 2C, G, K). The CD34^{+}
171 cells were negative for Desmin [Figure 2H), which primarily stained the circumferential LMCs (Figure
172 2F; note that the largely non-circumferential cell organization in this region is typical for a lymphatic
173 endothelial valve site (Bridenbaugh et al., 2013a)]. Furthermore, CD34^{+} cells and cKIT^{+} cells were
174 separate populations (Figure 2D, L). A Vimentin antibody labeled lymphatic endothelial cells (LECs)
175 which exhibited a horizontal cobblestone morphology in parallel with the vessel axis (Figure 2E, I), while
176 also co-labeling the majority of the CD34^{+} cells (Figure 2H) and cKIT^{+} cells (Figure 2L). Videos of the
177 half vessel z-stacks are provided (Supplemental Movies 1-3 for Figure 2D, H, and L respectively).
178 Of the cells stained in Figure 2, the CD34^{+} population was intriguing due to its high density and
179 distribution throughout the length of the IALV, which potentially would be conducive to effective
180 regulation of LMC excitability. In addition to CD34 and Vimentin, PDGFRα staining is also commonly
181 ascribed to both telocytes (Vannucchi et al., 2013; Xiao et al., 2013; Zhou et al., 2015) as well as
182 fibroblasts (Kimura et al., 2021; Clayton et al., 2022). We performed immunofluorescence imaging for
183 PGDFRα counterstained with CD34 and markers for LMCs, LECs, and pericytes. As noted in Figure 2,
184 CD34^{+} cells (Figure 3A) did not co-label LMCs (Figure 3D) which were smooth muscle actin^{+} (SMA,
185 Figure 3B) and Calponin^{+} (Figure 3C). However, nearly all CD34^{+} (Figure 3E) cells were also PDGFRα^{+}
186 (Figure 3F, H). Occasionally some overlap of PDGFRα and SMA^{+} signal was noted (Figure 3G, H).
187 LECs staining with CD31 (PECAM, Figure 3I) revealed the expected rectangular elongated cobblestone
188 morphology that was distinct from the PDGFRα+ cells (Figure 3J, L). Staining for Calponin also
189 specifically labeled LMCs (Figure 3K) but not PDGFRα^{+} cells (Figure 3L). Lastly, we stained for
190 PDGFRα, CD34, and PDGFRβ, a commonly used pericyte marker (Figure 3 M-P). As above, CD34 and
191 PDGFRα were highly colocalized (Figure 3Q, R, T), and many of the CD34^{+} and PDGFRα^{+} cells were
192 also PDGFRβ^{+} (Figure 3P). PDGFRβ also stained some circumferential LMCs (Figure 3Q). During the
193 imaging of mouse IALVs for these markers, we also observed that the lymphatic secondary endothelial
194 valves were populated by elongated cells that stretched the length of the valve leaflet and were positive
195 for CD34, PDGFRα, and PDGFRβ, with varying intensities. These cells could be observed in most, if not
196 all, the valves we assessed and found within both leaflets of the valve (Figure 3R,S). These cells had long,
197 thin extensions that were branched, along with apparent dendrite extensions with a morphology that
198 closely resembled those described of pericytes or telocytes (Popescu and Faussone-Pellegrini, 2010).
199 PDGFRα^{+} or CD34^{+} cells with this morphology were only observed in the valve leaflets, and thus seemed
200 insufficient to regulate pacemaking as normal contractions are observed in cLVs without secondary
201 valves (Van Helden, 1993; Gashev et al., 2002). Representative z-stacks demonstrating these valve-
202 located "telocyte" shaped cells (Figure 3R,S) are provided as Supplemental Movies 4 and 5.
203 We next determined the degree of colocalization between the CD34 and PDGFRα signal given
204 the significant overlap in their staining profile. Colocalization analysis of PDGFRα (SuppFigure 1A) and

205 CD34 (SuppFigure 1B) and their colocalization (SuppFigure 1C) was determined with the FIJI BIOP-
206 JACoP tool. The Pearson's coefficient was 0.83 (SuppFigure 1D) and Mander's coefficient of overlap
207 0.80 was for the PDGFRα$^+$ signal and 0.87 for the CD34 signal (SuppFigure 1E). Colocalization between
208 Myh11 and PDGFRα was significantly lower (SuppFigure 1D-F) with a Pearson's coefficient of 0.30
209 (SuppFigure 1G), whereas the Mander's coefficient for Myh11 overlap with PDGFRα was 0.077 and
210 PDGFRα signal overlap with Myh11 was 0.043 (SuppFigure 1H). The high degree of colocalization
211 CD34 and PDGFRα signal informed our use of the commercially available transgenic *PdgfrαCreER^{TM}*
212 mouse model to target these cells. The vast majority of the PDGFRα$^+$ cells were located in the adventitial
213 layer (SuppFigure 2A-D), which varied between 1-3 PDGFRα$^+$ cells thick (SuppFigure 2E). Under this
214 layer, we observed only a single layer of largely circumferential LMCs stained by Myh11 (SuppFigure
215 2B) sitting atop a single layer of CD31$^+$ LECs (SuppFigure 2A). We also observed occasional PDGFRα$^+$
216 cells or their extensions located in the sub-endothelial space (SuppFigure 2 E', E") positioned between the
217 LECs and the LMCs.
218
219 **Use of iCre-Mediated Recombination of Rosa26mT/mG to Delineate and Characterize Specific**
220 **IALV Cell Types**
221 After confirming the presence of Vimentin$^+$, cKit$^+$, and CD34$^+$ PDGFRα$^+$ positive cells within the
222 mouse IALV, we sought to further investigate these cell populations by using constitutive and inducible
223 Cre recombinase expressing mouse lines. IALVs from the constitutively active *PdgfrαCre*-
224 ROSA26mTmG and *Ng2Cre*-ROSA26mTmG mice had GFP fluorescence in the majority of LMCs as
225 well as in the fibroblast-shaped cells found within the IALV wall (Figure 4 A,B). While informative of
226 expression of the LMC progenitor cells, neither constitutive Cre would be useful in delineating cell types.
227 In contrast to the constitutively active *PdgfrαCre*, the tamoxifen inducible *PdgfrαCreER^{TM}* line drove
228 significant recombination in only the fibroblast-shaped cells previously stained with CD34 and PDGFRα
229 but not in LMCs or LECs (Figure 4C). *PdgfrβCreER^{T2}*, commonly used to label pericytes, drove
230 recombination in both a minor population of the LMCs and the fibroblast-shaped cells. *cKitCreER^{T2}*,
231 which capably drives recombination in the ICC of the GI (Baker et al., 2016), drove recombination only
232 in a small population of irregularly spaced large ovoid cells on the surface of the IALV (Figure 4E),
233 although recombination in 1 or 2 LECs could occasionally be detected (not shown). Finally,
234 *Myh11CreER^{T2}* drove recombination in nearly all LMCs which were largely circumferentially oriented
235 with dendrite-like, cell-cell contacts visible between them and without significant GFP fluorescence in
236 either LECs or the fibroblast-shaped CD34$^+$ PDGFRα$^+$ cell population (Figure 4F). Additionally, some
237 LMCs maintained the bipolar shape but had secondary extensions forming a "Y" shape in which an
238 adjacent LMC typically filled the inner void. A very minor population of recombined cells in the
239 *Myh11CreER^{T2}*-ROSA26mTmG IALVs were smaller and irregularly patterned with multiple fine axon-
240 like projections or ruffled edges (Figure 4F).
241 To complement the morphological and cell density findings obtained with confocal microscopy,
242 we digested IALVs from the iCre-ROSA26mTmG lines, and the *Prox1-eGFP* line as a control, into
243 single cell suspensions and sorted the respective GFP$^+$ populations (Figure 4G-J) for RT-PCR profiling
244 (Figure 4K). We first focused on determining the molecular fidelity of the sorted cells based on the gene
245 promoters used to drive each "iCre" model to discern cellular overlap. In agreement with the confocal
246 images, sorted GFP$^+$ cells from *PdgfrβCreER^{T2}*-ROSA26mT/mG IALVs expressed *Pdgfrβ* but also
247 *Myh11* and *Pdgfrα*. In contrast, GFP-sorted cells from *PdgfrαCreER^{TM}* IALVs expressed *Pdgfrα* and
248 *Pdgfrβ*, but with no detectable expression of *Myh11*. GFP$^+$ cells from sorted *Myh11CreER^{T2}*-
249 ROSA26mTmG IALVs had high expression for *Myh11* as well as *Pdgfrβ*, but did not express *Pdgfrα*.
250 IALVs from *cKitCreER^{T2}*-ROSA26mTmG mice were not pursued for FACS due to the exceptionally
251 sparse recombination observed along the IALV.
252
253 **Characterization of the cellular constituents of the mouse IALVs by scRNAseq and FACs-RT-PCR**
254 The results from the immunofluorescence staining, ROSA26mTmG reporter imaging, and FACs-
255 RT-PCR experiments suggested both LMCs and AdvCs express *Pdgfrβ*. To provide further clarity and

detail to the cellular populations within the mouse cLV wall, and potential subsets within those broad cell types we performed scRNAseq on our isolated and cleaned inguinal axillary cLVs from male and female mice. The resulting UMAP projection (Figure 5A) revealed a host of cell types which had 3 main clusters which corresponded to LECs, LMCs and AdvCs (Figure 5A). We assessed the expression of genes that correspond to the markers from our earlier immunofluorescence staining as well as cell identification markers commonly used within the literature to identify each cell cluster (Figure 5B). Cell identity was confirmed by commonly used markers (Figure 5B) and the top differentially expressed genes (SuppFigure 3A). Dot plots for the LEC markers *Prox1 (*Figure 5*C)* and *Flt4 (*Figure *5D)*, LMC markers *Myh11* (Figure 5E) and *Cnn1* (Figure 5F), and the AdvCs markers *Pdgfrα* (Figure 5G) and *Lumican* (Figure 5H) were quite specific for labelling their respective cell clusters. Very few *Kit* (Figure 5I) expressing cells were observed in accordance with our imaging results. *Pdgfrβ* was observed in both LMC and AdvC clusters (Figure 5J) while the remaining cell clusters were of immune origin as they expressed the gene encoding the hematopoietic marker *CD45* (Figure 5K). Notably, the previous genes suggested to identify LMCs in a previous scRNASeq study (Kenney et al., 2022), *Dpt*, *Pi16*, and *Ackr3*, were largely absent in LMCs and instead were expressed in a minor population of AdvCs (SuppFigure3B). We provide a further sub-clustering breakdown of the LECs (SuppFigure 4), LMCs (SuppFigure5), AdvCs (SuppFigure 6), and a detailed expression profile of the immune cell clusters (SuppFigure7). Further assessment of the LEC subcluster included a putative lymphatic endothelial "up valve" cell population in sub cluster 8 which expressed high levels of *Prox1*, *Cldn11*, *Itga9*, *Gja4*, and *Neo1* and "down valve" population in cluster 6 which expressed Clu, Adm, Gja4 and Lypd6 (SuppFigure 4C) which map well to a previous RNAseq dataset (Gonzalez-Loyola et al., 2021; Petkova et al., 2023; Yoon et al., 2024). The top differentially expressed genes in the putative down valve population in cluster 8 included *Irx3*, *Neo1*, *Tub*, *Ano4*, and *Fxyd2* and we noted Cacna1e, Fgf14, and Irf1 in the up-valve cluster 6. Analysis of the LMC subclusters did not reveal any significant differences in known pacemaking associated genes *Ano1* or *Itpr1* expression. However, we provide an overview of the typical ion channel families expressed in LMCs in SuppFigure 5B-I. The AdvC cells could be further subclustered into multiple populations (SuppFigure 6A,C) with little evidence of LMC gene contamination as these cells lacked *Myh11*, *Kcnma1*, and *Tagln* though despite expression of *Cacna1c*, *Ano1*, and *Cx45*. Over 75% of AdvCs expressed *Pdgfrα* (SuppFigure 6) and 65% of the total AdvCs expressed both *Pdgfrα* and *CD34.* Our immunofluorescent colocalization of *Pdgfrα* and *CD34 was also supported as* 72% of *Pdgfrα expressing* AdvCs also co-expressed *CD34* (SuppFigure 6D). The vast majority of AdvCs expressing *Pdgfrβ* (SuppFigure 6E) or *Cspg4* (SuppFigure 6F) also expressed *Pdgfrα.* Expression of *Ano1*, *Cx45*, and *Cacna1c*, was also observed in some of the AdvCs and most of these cells also co-expressed *Pdgfrα* supporting further use of the *PdgfrαCreER*^{TM} line (SuppFigure 6G-I).

While scRNASeq highlighted the depth of heterogeneity of the cellular composition of the mouse cLV, we wanted to validate the actual recombined cell populations from our iCre-ROSA26mTmG models. We profiled each iCre driven recombination of ROSAmTmG via FACs-purified cells and RT-PCR for common markers for endothelial cells, muscle cells, and pericytes. *Nos3* (eNOS) expression was observed only in the *Prox1-eGFP* sorted cells, and LECs also expressed *Vim*, *Mcam*, and had weak but detectable signal for *CD34* (Figure 6A). *Myh11CreER*^{T2} sorted cells showed expression of smooth muscle actin (*Acta2*), the alpha subunit of the L-type voltage gated Ca^{2+} channel *Cacna1c* (*Cav1.2*), *Desmin* (*Des*), *M*cam, and *Vimentin* (*Vim*, Figure 6B). In addition to the genes expressed under *Myh11CreER*^{T2} recombination, *Cdh5*, *CD34*, and *Cspg4* (*Ng2*) were detected in cells sorted from *PdgfrβCreER*^{T2} IALVs (Figure 6C). As expected, the GFP^{+} cells sorted from *PdgfrαCreER*^{TM} IALVs expressed mRNA for *CD34*, weak signal for *Cspg4*, and *Vimentin*, but not *Desmin*, *Acta2*, nor the pericyte marker *Mcam* (Figure 6D). The *Cacna1c* was expressed in cells FACS purified from both *PdgfrβCreER*^{T2} and *Myh11CreER*^{T2} IALVs and sorted cells from *PdgfrαCreER*^{TM} IALVs without any evidence that *Myh11* expressing muscle cells contaminated the latter. These findings confirmed the separate cell populations achieved with *PdgfrαCreER*^{TM} and *Myh11CreER*^{T2} mediated recombination, at least as it pertains to the ROSA26mTmG reporter. These findings were largely validated by our scRNASeq dataset. *Cdh5* (Figure

6E) and *Nos3* (Figure 6F) were almost exclusively expressed in our LEC clusters while *Acta2* (Figure 6G) was highly expressed in the LMC cluster. We also observed that *Cacna1c* was highly expressed in the LMCs (Figure 6H) and some AdvCs. *Cd34* was highly expressed in the AdvCs but was also observed in LECs (Figure 6I) although we did not observe a signal in our earlier immunofluorescence staining (Figure 3). *Cspg4* was observed in a minor population of AdvCs (Figure 6J). The intermediate filament *Vim* (Figure 6K) was ubiquitously across all clusters expressed but *Des* was primarily expressed in LMCs and some subsets of AdvCs (Figure 6K,L). The endothelial and pericyte marker *Mcam* (also referred to as CD146) was expressed in LECs and LMCs but was largely absent in AdvCs (Figure 6M). We followed up the identification of Cav1.2 expression in the *PdgfrαCreER*^{TM} sorted cell population by assessing the expression of other genes involved in either electrical conduction (Cx45) (Figure 6N) or pacemaking (Ano1) (Figure 6O) of IALVs. Expression of *Ano1* and *Cx45* was observed in Pdgfr*αCreER*^{TM} ROSA26mtmG FACS-purified cells (Figure 6P).

Inducible Deletion of Either Cav1.2, Ano1, and Cx45 with *PdgfrαCreER*^{TM} Did Not Affect cLV Pacemaking

The expression of the genes critically involved in cLV function—Cav1.2, Ano1, and Cx45—in the *PdgfrαCreER*^{TM}-ROSA26mTmG purified cells and scRNAseq data prompted us to generate *PdgfrαCreER*^{TM}-*Ano1*$^{fl/fl}$, *PdgfrαCreER*^{TM}-*Cx45*$^{fl/fl}$, and *PdgfrαCreER*^{TM}-*Cav1.2*$^{fl/fl}$ mice for contractile tests. We isolated popliteal cLVs and tested their pacemaker and contractile function in response to a physiological pressures range of 0.5-10 cmH_2O, under normal conditions. However, we did not detect any significant differences in pacemaking nor contractile function as assessed by contraction frequency, ejection fraction, and vessel tone in popliteal cLVs studied from *PdgfrαCreER*^{TM}-*Ano1*$^{fl/fl}$ mice (Figure 7A-C) or *PdgfrαCreER*^{TM}-*Cx45*$^{fl/fl}$ mice (Figure7D-F). There was no difference in contraction frequency in cLVs from *PdgfrαCreER*^{TM}-*Cav1.2*$^{fl/fl}$ mice, however, we noted a mild but statistically significant increase in ejection fraction at the lowest pressure, 0.5 cmH_2O (Figure 7H). Additionally, vessels isolated from *PdgfrαCreER*^{TM}-*Cav1.2*$^{fl/fl}$ mice also had a statistically significant increase in vessel tone (Figure 7I) noted at the 2-way level although we did not resolve significance at any specific pressure with this sample. No difference in normalized contraction amplitude, fractional pump flow, or diastolic diameters were observed (SuppFigure 8). In total, despite the presence of transcript for these critical genes in *Pdgfrα*$^{+}$ cells, *PdgfrαCreER*^{TM} mediated deletion of *Cx45*, *Cav1.2* or *Ano1* failed to recapitulate previous reports of the significant contractile defects using the *Myh11CreER*^{T2} line (Castorena-Gonzalez et al., 2018b; Zawieja et al., 2019; To et al., 2020; Davis et al., 2022).

PDGFRα^{+} Adventitial Fibroblasts Express Markers Associated with Multipotency

Despite the lack of cLV pacemaking deficits in the *PdgfrαCreER*^{TM} genetic knockout lines, we were curious to discern further insight into the role or function of the PDGFRα^{+} CD34^{+} cells since they comprise a significant portion of the lymphatic cLV wall. We performed RT-PCR on FACS purified cells from *Prox1-eGFP*, *Myh11CreER*^{T2}-ROSA26mTmG, and *PdgfrαCreER*^{TM}-ROSA26mTmG IALVs for markers multipotency including Krüppel-like factor 4 (*Klf4*), stem cell antigen 1 (*Sca1*, also referred to as *Ly6a*), and *Gli1 with CD34* and *Pdgfrα* used to assess purity. Recombined (GFP^{+}) cells from *Myh11CreER*^{T2}-ROSA26mTmG had weak expression of *Klf4* and *Gli1 but* were negative for *Ly6a* (SuppFigure 9A). *PdgfrαCreER*^{TM} recombined cells strongly expressed *Klf4, Ly6a,* and *Gli1 (*SuppFigure 9A). LECs sorted from *Prox1-eGFP* IALVs were positive for *Klf4*, weak for *Ly6a*, and positive for *CD34* but negative for *Gli1* and *PDGFRα* (SuppFigure 9B). The unrecombined population (tdTomato^{+}) cells in the *Myh11CreER*^{T2}- ROSA26mTmG IALVs (SuppFigure 9B) showed expression for all the markers as expected. *PdgfrαCreER*^{TM} *recombined cells* also expressed the mesenchymal stromal cell markers *CD29*, *CD105*, and CD44 (SuppFigure 9C, positive control in 9D). However, expression of these genes was not homogenous across all the AdvCs population based on our scRNAseq analysis (SuppFigure 9E-J). We performed immunofluorescence staining for one of these multipotent markers, Ly6a (SuppFigure 9K) in the adventitial cells with PDGFRα (SuppFigure 9L) and counter staining for LMCs with MYH11

357 (SuppFigure 9M). The morphology and staining pattern of Sca1 overlapped significantly with PDGFRα
358 staining and not Myh11 staining (SuppFigure 9N, Supplemental Movie 6).
359
360 **Optogenetic Stimulation of iCre-driven Channel Rhodopsin 2 to Induce Test Light-Stimulated**
361 **Depolarization Induced Lymphatic Contraction**
362 We next used optogenetic methods to test whether the cell populations recombined by either
363 *cKitCreER^{T2}*, *PdgfrαCreER^{TM}*, or *Myh11CreER^{T2}* could elicit a coordinated contraction. The ChR2-
364 tdTomato construct appeared more sensitive to recombination than ROSA26mTmG, in some cases
365 resulting in LMC expression of ChR2-tdTomato in *PdgfrαCreER^{TM}* and *CkitCreER^{T2}* popliteal cLVs
366 based on morphology. Care was taken to image each vessel for tdTomato (Figure 8A,C,E) prior to
367 stimulation at its respective sites under brightfield conditions for diameter tracking (Figure 8B,D,F) to
368 ensure fidelity of the cell types and morphologies observed in Figure 3 and Figure 4. As with
369 ROSA26mTmG, *CkitCreER^{T2}* drove the ChR2-tdTomato expression primarily in large ovoid cells found
370 on the adventitia of the vessel. Cells were stimulated by positioning an optical laser fiber (tip diameter 2-3
371 mm) near a ChR2+ cell, with an illumination field of 10-50 mm. Localized photo-stimulation of these
372 cells did not initiate coordinated contractions (Figure 8G-J,S). Similarly, photo-stimulation of ChR2-
373 tdTomato expressing cells driven by *PdgfrαCreER^{TM}* failed to initiate a coordinated contraction (Figure
374 8K-N, T). In contrast, localized photo-stimulation of LMCs, using *Myh11CreER*T2 to express Chr2-
375 tdTomato, resulted in a propagated contraction in the popliteal vessel (Figure 8O-R, U). In total, only
376 3.25% of photo-stimulation events for *cKitCreER^{T2}*-ChR2-TdTomato and 3.03% of photo-stimulation
377 events for *PdgfrαCreER^{TM}*-ChR2-tdTomato were associated with a contraction, while 88.5% of photo-
378 stimulation events for *Myh11CreER^{T2}*-ChR2-tdTomato induced contractions (Figure 8V). The
379 optogenetic triggering of contractions observed in *PdgfrαCreER^{TM}*-ChR2-tdTomato and *cKitCreER^{T2}*-
380 ChR2-TdTomato vessels is likely due to the happenstance of spontaneous contractions occurring during
381 the time and proximity of optogenetic stimulation (see Methods). As a control, we also used non-induced
382 (no tamoxifen) *Myh11CreER^{T2}*-ChR2-tdTomato cLVs and contractions were associated with only 7% of
383 photo-stimulation events, in line with the *PdgfrαCreER^{TM}* and *cKitCreER^{T2}* results (Figure 8V). As mast
384 cells are not ascribed any tissue specific pacemaking behavior, these similar low percentages observed
385 between these three groups are suggestive of random coincidence. Brightfield videos of the photo-
386 stimulation and representative traces for *cKitCreER^{T2}*-ChR2-TdTomato, *PdgfrαCreER^{TM}*-ChR2-
387 tdTomato, *Myh11CreER^{T2}*-ChR2-tdTomato are provided in Supplemental Movies 7-9.
388
389 **Confocal Ca^{2+} Imaging of GCaMP6f Expression Driven by *cKitCreER^{T2}*, *PdgfrαCreER^{TM}*, and**
390 ***Myh11CreER^{T2}* Over the Lymphatic Contraction Cycle**
391 Subcellular calcium transients are observed in many pacemaker cells. We imaged IALVs from
392 *cKitCreER^{T2}*-GCaMp6f mice, which primarily resulted in expression of GCaMp6f in the large ovoid cells
393 in the adventitia (Figure 9A), although we occasionally observed GCaMP6f expression in both LEC and
394 LMCs (Figure 9A) as depicted in the maximum projection of the acquisition period (Supplemental Movie
395 10) and the spatio-temporal maps (STMS). The aberrant expressions of GCaMP6f in cells that
396 demonstrated the typical cobblestone morphology of LECs or the circumferential LMCs that exhibited
397 Ca^{2+} flashes and diastolic Ca^{2+} transients (Figure 9D,E green arrows) prior to contraction were not
398 included in the *cKitCreER^{T2}*-GCaMp6f analysis. Of 39 *cKitCreER^{T2}*-GCaMp6f cells analyzed, only 1
399 *cKitCreER^{T2}*-GCaMP6f cell exhibited a spontaneous Ca^{2+} transient during the recording period (Figure
400 9B,C Cell 7). However, the Ca^{2+} transient in that cell did not align temporally with the "Ca^{2+} flash" of the
401 LMC with incidental GCaMp6f expression (Figure 9C,D). Despite the lack of Ca^{2+} transients under the
402 baseline conditions throughout the IALV contraction cycle, many *cKitCreER^{T2}*-GCaMP6f cells exhibited
403 a robust and prolonged Ca^{2+} event in response to stimulation with the mast cell activator compound 48-80
404 (Figure 9F, G, H). Notably, the Ca^{2+} events in the ovoid cells elicited by administration of compound 48-
405 80 did not acutely alter the LMC Ca^{2+} activity (Figure 9I,J). Like *cKitCreER^{T2}*-GCaMp6f, the majority of
406 PDFR□CreER^{TM}-GCaMP6f expressing cells also largely lacked Ca^{2+} transients and resulted in incidental
407 LMC GCaMP6f expression (Figure 10B, Supplemental Movie 11). Some cells exhibited high basal Ca^{2+}

408 levels (Figure 10A,D) sustained throughout the recording, but without oscillations (Figure 10B,C). In
409 contrast, spurious GCaMP6f expression in a circumferentially oriented LMC displayed Ca^{2+} flashes
410 associated with contraction (Figure 10B,C). Of the 21 PDGFRα-GCaMP6f cells assessed, only 3
411 exhibited Ca^{2+} transients that were singular events with limited spatial spread within the 20 sec imaging
412 period (Figure 10E,F). The lack of either global or consistent Ca^{2+} transients within either *cKitCreER*^{T2}-
413 GCaMP6f or *PdgfrαCreER*^{TM}-GCaMP6f IALVs was in stark contrast to Ca^{2+} imaging of *Myh11CreER*^{T2}-
414 GCaMP6f IALVs. *Myh11CreER*^{T2} drove GCaMp6f expression in the circumferential LMCs (Figure
415 11A), which had global and nearly synchronous Ca^{2+} flashes in 100% of the analyzed cells (Figure 11B,
416 C). Additionally, non-synchronous stochastic and localized Ca^{2+} transients during diastole were
417 commonly observed in the LMCs (Figure 11D, E, Supplemental Movie 12). Many LMCs exhibited Ca^{2+}
418 transients during each diastolic period while other LMCs displayed few Ca^{2+} transients or lacked diastolic
419 Ca^{2+} transients during the recording period (Figure 11B). In aggregate, of the 39 *cKitCreER*^{T2}-GCAMP6f
420 cells only 1 displayed a Ca^{2+} transient during recording, 3 of 21 *PdgfrαCreER*^{TM}-GCaMP6f cells, while
421 20 of 43 LMCs displayed at least one diastolic transient apart from 43 of 43 LMCs with global flashes.
422
423 **Pressure Dependency of Subcellular Ca^{2+} Transients in LMCs**
424 We next sought to test whether diastolic Ca^{2+} transients were pressure-dependent, given that
425 cLVs exhibit pressure dependent chronotropy (Zawieja et al., 2019). GCaMP6f expressing LMCs were
426 studied at intraluminal pressures of 0.5 -5 cmH_2O in the presence of nifedipine, which blocks the Ca^{2+}
427 flashes but not local Ca^{2+} transients (Figure 12A). As intra-luminal pressure was increased, there was a
428 marked increase in the occurrence of Ca^{2+} transients (Figure 12B, Supplemental Movies 13-15). We
429 converted these calcium transients into particles (PTCLs) for further analysis as previously described. We
430 generated activity maps of Ca^{2+} PTCL activity (Figure 12C) and determined PTCL area (Figure 12D) and
431 frequency at each pressure (Figure 12E). The maps show that as pressure increased, the activity of PTCLs
432 across the vessel also increased (as evident by the increase in PTCL area activation). Across 11
433 experiments, the area of the field of view activated by PTCLs/frame increased from 73.2 ± 17.7 μM
434 ^{2}/frame at 0.5 cmH_20 to 108.6 ± 20.5 μM ^{2}/frame at 2 cm H_20 and further enhanced to 139.2 ± 26.9 μM
435 ^{2}/frame at 5 cm H_2O (Figure 12F). The number of PTCLs per frame also increased with pressure, from 2.9
436 ± 0.4 at 0.5 cmH_20 to 4.1 ± 0.5 and 5.2 ± 0.6 PTCL/frame at 2 and 5 cmH_20 respectively (Figure 12G).
437
438 **Contraction Frequency is Set by the Diastolic Depolarization Rate**
439 To assess how pressure regulates LMC membrane potential we first recorded membrane potential
440 in cells exhibiting action potentials (APs) using a microelectrode filled with biocytin-AF488 to label the
441 cell. In each case (n=3 IALVs) the labeled cell were LMCs wrapping circumferential around the vessel
442 (Figure 13A, B) and as these recordings were made over the course of many minutes the neighboring
443 circumferential LMCs also exhibited fluorescence, albeit weaker in intensity, as expected (Figure 13A).
444 In all the recorded cells exhibiting APs, we noted a diastolic depolarization preceding the sharp upstroke
445 achieved once threshold was met at each pressure (Figure 13C). The AP frequency and rate of the
446 diastolic depolarization increased with pressure (Figure 13D, E). Linear regression of a plot of each AP
447 frequency and diastolic depolarization rate at each pressure demonstrated a tight associated between the
448 two parameters. However, we did not observe a significant effect of pressure on minimum membrane
449 potential (Figure 13G), threshold potential (Figure 13H), the AP upstroke (Figure 13I), AP peak potential
450 (Figure 13J), plateau potential (Figure 13K), or the time spent over threshold (Figure 13L).
451
452 **Discussion**
453 The identification of the cellular origin and signaling mechanisms underlying cLV pacemaking
454 will reveal novel targets for pharmacological intervention in treating lymphedema and the associated
455 lymphatic contractile dysfunction. In this study we tested proposed pacemaker cell types based on 3
456 parameters: 1) that the pacemaker cells are located along the entire length of the cLV, to accommodate
457 spontaneous contractions and coordinated electrical conduction despite progressive shortening of cLVs;
458 2) that depolarization of the pacemaker cell can drive a coordinated and propagated contraction of the

459 vessel; and 3) that the presence of Ca^{2+} transients precedes or coincides with contraction, as commonly
460 observed in other pacemaker cells. We used confocal microscopy and a combination of
461 immunofluorescence and fluorescent reporters under the control of various inducible Cres to identify and
462 target both muscle and non-muscle cells, previously labeled as ICLCs, that coexpress the markers CD34
463 and PDGFRα. Our cell characterizations were supplemented by scRNAseq analysis of isolated and
464 cleaned mouse IALVs which supported our finding of 3 major cell types including LECs, LMCs, and
465 AdvCs each of which could be further sub-clustered into transcriptionally unique populations. From our
466 initial fluorescence imaging studies, a role for intrinsic pacemaking by LMCs (Van Helden, 1993; von der
467 Weid et al., 2008), or by a novel population of $CD34^+$ lymphatic ICLC (McCloskey et al., 2002; Briggs
468 Boedtkjer et al., 2013), also referred to as telocytes, were further examined and found to co-express
469 *Pdgfrα*. We utilized *PdgfrαCreER*^{TM} to further test whether these cells exhibited pacemaker capabilities.
470 However, these $Pdgfrα^+$ cells had minimal Ca^{2+} activity despite ongoing contractions and optogenetic
471 stimulation of ChR2 in these cells failed to drive a spontaneous contraction. In contrast, photo-stimulation
472 of LMCs expressing ChR2 elicited robust, propagated contractions with similar characteristics and
473 propagation to spontaneous contractions in the same vessels. Furthermore, Ca^{2+} imaging in LMCs
474 revealed diastolic Ca^{2+} transients in diastole that increased in frequency and spatial spread as pressure was
475 elevated. We also demonstrated that the primary component of the AP driving the frequency change with
476 pressure is the diastolic depolarization, which we have previously reported to be dependent on Ano1
477 (Zawieja et al., 2019) and IP3R1 (Zawieja et al., 2023). Notably, we recently reported that diastolic Ca^{2+}
478 transients are abrogated in IALVs from Myh11CreER^{T2}-Itpr1 inducible knockout mice, supporting a
479 IP3R1-Ano1 axis as the pressure dependent pacemaker mechanism in LMCs. These results, in addition to
480 the recent findings using targeted deletion of Cx45 (Castorena-Gonzalez et al., 2018b) or Cav1.2 (To et
481 al., 2020; Davis et al., 2022) in lymphatic muscle support the model of LMCs as the intrinsic pacemaker
482 as has been previously proposed (Van Helden, 1993; Van Helden et al., 1996; Van Helden and Zhao,
483 2000).
484
485 **Pacemaking in Smooth Muscle**
486 In many smooth muscle organs, regulation of a coordinated contraction is a complex and
487 multicellular phenomenon. Multiple cell types integrate physical and biological information into electrical
488 activity to be transmitted to the force-producing smooth muscle cells, sometimes across great distances
489 relative to cell size, to regulate Ca^{2+} influx by voltage dependent Ca^{2+} channels required for contraction.
490 The intestine is one such documented tissue in which $cKit^+$ ICCs and interstitial $PDGFRα^+$ cells form an
491 electrical syncytium to regulate intestinal motility (Sanders et al., 1999; Sanders et al., 2014). The
492 pacemaking function of intestinal ICCs relies heavily on Ano1, a Ca^{2+} activated Cl^- channel, which is
493 required for slow wave activity in the ICCs. Both cKit and Ano1 can be used as a marker for ICCs in the
494 intestine (Hwang et al., 2009; Cobine et al., 2017; Malysz et al., 2017), $cKit^+$ and $vimentin^+$ ICLCs have
495 been observed in sheep lymphatic vessels (McCloskey et al., 2002), yet these cell populations did not
496 form gap junctions with the smooth muscle to form electrical connections (Briggs Boedtkjer et al., 2013)
497 as occurs in the intestinal ICCs. Our cKit staining and *CkitCreER*^{T2}-ROSA26mTmG reporter studies on
498 mouse IALVs revealed a sparse population of large ovoid cells previously classified as mast cells
499 (Chatterjee and Gashev, 2012; Zawieja et al., 2019). Their identity as mast cells was further supported by
500 a sustained global Ca^{2+} event after stimulation with the mast cell degranulating agent compound 48-80.
501 However, both vimentin and CD34 showed robust staining throughout the mouse lymphatic vessel wall.
502 Vimentin stained LECs, as well as non-muscle stellate shaped cells, with many co-expressing CD34, and
503 other smaller circular cells some of which were $cKit^+$ as well and some whose morphology was similar to
504 that of the macrophage staining profile of the GFP^+ cells in IALVs from MacGreen mice, consistent with
505 previous reports of macrophage staining in cLVs (Bridenbaugh et al., 2013b; Chakraborty et al., 2015;
506 Zawieja et al., 2016). While $vimentin^+$ cells had a perinuclear staining profile, CD34 demarcated the cell
507 membrane and was useful for assessing the morphology of these cells. Of particular interest, the
508 $vimentin^+CD34^+$ cells densely populated the length of the mouse IALV, with a majority displaying a
509 flattened stellate morphology characterized by the classic rounded oak leaf appearance, although some

510 displayed fine dendrite extensions. Contrasting with the previous findings in the human thoracic duct
511 (Briggs Boedtkjer et al., 2013), we did not observe a significant population of $CD34^+$ cells with a bipolar
512 morphology oriented axially along the vessel. However, z-stack reconstructions of sections of the mouse
513 IALV that included the secondary valves revealed interstitial $CD34^+PDGFR\alpha^+$ cells that resembled the
514 bipolar cells with multiple axon-like extensions throughout the endothelial leaflets similar to interstitial
515 cells that were reported in in collecting vessel valves (Leak and Burke, 1968) and lymphovenous valves
516 (Geng et al., 2016). While these cells have not been frequently described in the peripheral cLV valves, we
517 observed these cells in each of the valve regions imaged in addition to labeling them with other Cre
518 drivers, including *NG2Cre-ROSA26mTmG* and *PdgfrβCreER*^{T2}*-ROSA26mTmG* (data not shown).
519 Whether these cells regulate leaflet extracellular matrix deposition or lymphatic valve integrity is
520 unknown, but a role as a critical pacemaker can be excluded as vessel segments without valves display
521 normal contractile behavior (Van Helden, 1993; Gashev et al., 2002). Instead, the majority of the
522 $CD34^+PDGFR\alpha^+$ cells were found in the adventitia with 2-3 layers overtop the LMCs and were
523 consistently observed in high density along the IALV. Some $CD34^+PDGFR\alpha^+$ cells or their extensions
524 were present between the lymphatic endothelial and muscle layers as had been previously reported with
525 electron microscopy of human lymphatic vessels (Briggs Boedtkjer et al., 2013). Thus while some of
526 these AdvCs may be contained within the extracellular matrix in the immediate vicinity of the lymphatic
527 vessel, and thus collected during dissection, many others are intimately dispersed within the vessel wall.
528
529 **$PDGFR\alpha^+CD34^+$ Cells are Not Involved in cLV Pacemaking Under Physiological Conditions**
530 Co-expression of CD34 and PDGFRα has recently been ascribed as a delineating feature of
531 telocytes, although PDGFRα routinely labels fibroblasts and specific interstitial cells in the GI tract
532 involved in purinergic neurotransmission (Kurahashi et al., 2011; Kurahashi et al., 2013; Clayton et al.,
533 2022), and CD34 expression has been observed in multipotent cell populations of various origins (Sidney
534 et al., 2014). In the intestinal villi, $PDGFR\alpha^+$ fibroblasts appear to be the progenitors of the smooth
535 muscle fibers associated with the lacteal, the lymphatic capillary in the villi (Sanketi et al., 2024). Of
536 course, mesenchymal stromal cells (Andrzejewska et al., 2019) and fibroblasts (Muhl et al., 2020;
537 Buechler et al., 2021; Forte et al., 2022), and it remains controversial to what extent telocytes are distinct
538 from or are components/subtypes of either cell type (Clayton et al., 2022), are not monolithic in their
539 expression patterns displaying both organ directed transcriptional patterns as well as intra-organ
540 heterogeneity (Lendahl et al., 2022) as readily demonstrated by recent single cell RNA sequencing studies
541 that provided immense detail about the subtypes and activation spectrum within these cells and their
542 plasticity (Luo et al., 2022a). We were able to distinguish up to 10 subclusters of AdvCs, the majority of
543 which expressed or co-expressed CD34 and PDGFRα. These cells were consistently negative for smooth
544 muscle markers such as *Des*, *Cnn1*, *Acta2*, *Myh11* or the pericyte marker *Mcam*. However, PDGFRβ
545 expression was noted in our scRNAseq and sorted *PdgfrαCreER*^{TM}-ROSA26mTmG cells, in addition to
546 the staining of LMCs. PDGFRβ protein expression was confirmed with variable immunofluorescence
547 staining amongst the PDGFRα stained cells as well as LMCs. The *PdgfrβCreER*^{T2}*ROSA26mTmG* mice
548 had only modest recombination in both the LMC and $PDGFR\alpha^+$ cell population, but potentially
549 highlighted a myofibroblast-like cell subpopulation, cells that might lie on the spectrum of differentiation
550 from lymphatic muscle and $PDGFR\alpha^+$ cells, or perhaps a cell with pacemaker activity as PDGFRβ is
551 widely used as a pericyte marker and some pericytes display pacemaker activity (Hashitani et al., 2015).
552 Adding to this intrigue, the *PdgfrαCreER*^{TM} sorted cells expressed transcripts for *Cacna1c*, the voltage-
553 gated L-type Ca^{2+} channel critical for lymphatic contractions (Zawieja et al., 2018a; To et al., 2020);
554 *Ano1*, the ion channel underlying pressure dependent chronotropy (Mohanakumar et al., 2018; Zawieja et
555 al., 2019); and *Cx45*, the primary connexin mediating electrical conduction in mouse lymphatic collecting
556 vessels (Castorena-Gonzalez et al., 2018b; Hald et al., 2018). Expression of these genes in certain sub-
557 populations of the AdvCs was also apparent in our scRNAseq analysis. Thus, the presence of those gene
558 transcripts does not appear to be due to muscle cell contamination or incidental recombination in LMCs
559 as we did not detect LMC markers in the RT-PCR profiling of the sorted $PDGFR\alpha^+$ cells nor were GFP-
560 expressing cells with an LMC morphology observed in imaging of *PdgfrαCreER*^{TM}-ROSA26mTmG

561 vessels. Critically, however, deletion of *Cav1.2*, *Cx45*, or *Ano1* through *PdgfrαCreER*^{TM}-mediated
562 recombination neither recapitulated the previous phenotypes achieved with *Myh11CreER*^{T2} (Castorena-
563 Gonzalez et al., 2018b; Zawieja et al., 2019; To et al., 2020; Davis et al., 2022) nor significantly affected
564 pacemaking in mouse popliteal cLVs. This is in stark contrast to the complete lack of contractions
565 observed in *Myh11CreER*^{T2}-*Cav1.2*$^{fl/fl}$ vessels (To et al., 2020) or the vessels from vascular muscle
566 specific *Itga8CreER*^{T2}-*Cav1.2*$^{fl/fl}$ mice (Davis et al., 2022; Warthi et al., 2022), and the significant loss in
567 pressure-induced chronotropic modulation of pacemaker function in IALVs with *Myh11CreER*^{T2}-
568 mediated deletion of Ano1 that we have previously reported (Zawieja et al., 2019) . While a sub-
569 population of CD34^{+}PDGFRα^{+} cells may share expression of critical pacemaker genes identified in the
570 LMCs, they do not appear to be involved in cLV pacemaking or contractile function under physiological
571 states. Instead, CD34^{+}PDGFRα^{+} cells co-stained significantly with Sca1^{+}, suggesting they may be primed
572 to act as resident multipotent cells (Song et al., 2020; Kimura et al., 2021). To this point, the
573 *PdgfrαCreER*^{TM} FACS purified cells also expressed markers associated with "stemness" such as *CD34*,
574 *Klf4*, *Gli1*, *CD29*, *CD105*, *CD44*, and *Vimentin*, in addition to *Sca1*, and it is likely that the
575 *PdgfrαCreER*^{TM} population includes various distinct subpopulations (Jolly et al., 2022) expressing these
576 markers. These cells may play a role in rebuilding the lymphatic collecting vessel vasculature following
577 collecting vessel damage or lymph node resection and further studies are required to assess their
578 functional multipotency.
579
580 **SR Ca^{2+} Cycling in Pacemaking**
581 The use of the mouse model, in addition to the simplicity of the vessel architecture, provided the
582 use of genetic tools that previously had been instrumental in identifying the cKit^{+} ICC as the pacemaker
583 cells of the GI tract (Ward et al., 1994; Huizinga et al., 1995; Torihashi et al., 1995). Through the use of
584 the respective *PdgfrαCreER*^{TM} and *Myh11CreER*^{T2} models, we were able to specifically image Ca^{2+} in
585 each cell type in pressurized, contracting vessels. Pacemaking initiating cells have an inherently unstable
586 membrane potential, oftentimes utilizing the oscillatory nature of Ca^{2+} release from the sarcoendoplasmic
587 reticulum coupled to Ca^{2+} sensitive electrogenic exchangers and ion channels to drive depolarization (Van
588 Helden, 1993; Hashitani et al., 2015; Baker et al., 2021b; Sanders et al., 2022). One such example is the
589 pacemaker ICC in the gastric corpus which exhibits abundant Ca^{2+} transients that couple to Ano1-
590 mediated chloride currents in both the intervening period between slow waves as well as the plateau phase
591 of the slow wave (Baker et al., 2021a), although such activity is not characteristic of all pacemaker ICC
592 types. The identification of a Ca^{2+} activated chloride current in LMCs (Van Helden, 1993; Toland et al.,
593 2000) and its correspondence with subcellular Ca^{2+} transients (Van Helden, 1993; Ferrusi et al., 2004; von
594 der Weid et al., 2008) led Van Helden to postulate that LMCs had an intrinsic pacemaking capability
595 (Van Helden, 1993; Van Helden et al., 1996). We have previously reported that mouse LMCs in
596 pressurized vessels routinely display subcellular Ca^{2+} release events that reflect the kinetics and
597 characteristics of Ca^{2+} puffs and waves in addition to the coordinated global Ca^{2+} flash associated with
598 Ca^{2+} influx during an AP (Castorena-Gonzalez et al., 2018b; Zawieja et al., 2018a; Zawieja et al., 2019).
599 Here we confirmed the consistent presence of subcellular Ca^{2+} transients only in LMCs with GCaMP6f
600 driven by *Myh11CreER*^{T2} but not in the cells with GCaMP6f driven by *PdgfrαCreER*^{TM}. Critically, we
601 also demonstrated that the Ca^{2+} transients increased in both frequency and spatial spread as pressure was
602 elevated in the vessel, as would be expected to account for the pressure dependent chronotropy observed
603 in lymphatic collecting vessels. This underscores the recent finding that the genetic deletion of Ano1 in
604 the LMCs dramatically reduced contraction frequency and abolished pressure-dependent chronotropy in
605 those vessels (Zawieja et al., 2019). This phenotype was largely replicated with a similar reduction in
606 frequency and loss of pressure dependent chronotropy in our recent study utilizing *Myh11CreER*^{T2} to
607 drive deletion of IP3R1 from LMCs (Zawieja et al., 2023) in which these diastolic Ca^{2+} transients were
608 absent. This fits with the central role of IP3R and subcellular Ca^{2+} release as critical components of
609 intrinsic LMC pacemaking (Van Helden et al., 1996; von der Weid et al., 2008). In addition to the
610 transcriptional heterogeneity identified by scRNASeq, we also noted heterogeneity in the propensity of
611 LMCs to display diastolic Ca^{2+} transients under control conditions or the sustained Ca^{2+} oscillations that

occur in the presence of nifedipine. We did not detect and significant difference in the expression of *Itpr1*, the gene encoding the IP3R1, across our LMCs subclusters. However, the LMC cluster "0" had significantly increased expression of *Itprid2* which encodes the KRas-induced actin-interacting protein (KRAP). KRAP has recently been implicated in IP3R1 immobilization and licensing and was required for IP3R1-mediated Ca^{2+} puffs (Thillaiappan et al., 2021; Atakpa-Adaji et al., 2024). Whether the higher expression of KRAP results in a greater probability of these LMCs to display IP3R1-dependent Ca^{2+} oscillations in LMCs requires further investigation.

The membrane potential recordings we made in this work suggest that the regulation of pressure dependent chronotropy is through modulation of the diastolic depolarization rate in LMCs, as previously demonstrated in rat mesenteric lymphatic vessels (Zawieja et al., 2018b). The appearance of the diastolic depolarization may depend on the method of stretch employed as it is not always observed in preparations using a wire myograph (von der Weid et al., 2014). Notably, in this study *PdgfrαCreER*^{TM} mediated deletion of Ano1 had no effect on contractile parameters. The lack of Ca^{2+} transients in PDGFRα^{+} cells across any stage of the lymphatic contraction cycle diminishes any expected role for this cell type to perform as the pacemaker for the mouse IALV. In the pacemaker ICCs, slow wave activity is dependent on calcium transient clusters Instead pressure-dependent Ca^{2+} mobilization from the SR, through IP3R1 (Zawieja et al., 2023), appears to set the basis for LMC pacemaking as previously proposed (Van Helden, 1991; von der Weid et al., 2008). However, the mechanisms driving IP3R1 activation and Ca^{2+} oscillations remain to be fully addressed.

A pacemaker cell would be expected to be electrically coupled to the LMC layer to permit the nearly synchronous conduction velocity of the contraction wave (Zawieja et al., 1993; Castorena-Gonzalez et al., 2018b; Hald et al., 2018) and to transmit depolarization into coupled LMCs to activate the voltage dependent Ca^{2+} channels that are responsible for lymphatic muscle APs. Connexins are the molecular constituents of gap junctions and, as stated above, we detected Cx45 expression in the *PdgfrαCreER*^{TM} sorted cells. However, we did not detect any impairment in pacemaking, nor were contraction conduction speed deficits or multiple pacemakers noted in the *PdgfrαCreER*^{TM} -Cx45fl/fl popliteal cLVs, in contrast to the development of multiple pacemaker sites and the lack of entrainment that characterize cLVs from *Myh11CreER*^{T2}-Cx45fl/fl mice (Castorena-Gonzalez et al., 2018b). Admittedly, we did not perform an exhaustive assessment of the connexin expression profile of the CD34^{+}PDGFRα^{+} cells, and Cx45 may not be the dominant connexin expressed in the CD34^{+}PDGFRα^{+} cells, or heterotypic connexons could exist (Koval et al., 2014). However, electron microscopy studies of the putative ICLC in the human thoracic duct did not detect any gap junctions, although peg-and-socket connections were observed (Briggs Boedtkjer et al., 2013). We utilized optogenetics to directly depolarize the specific cell populations in both the *PdgfrαCreER*^{TM} and *Myh11CreER*^{T2} mouse models in an attempt to drive contractions. Local photo-stimulation of the PDGFRα cells failed to initiate contraction while the stimulation of *Myh11CreER*^{T2} recombined cells resulted in contractions that were indistinguishable from the spontaneously occurring contractions. These results give functional credence to the lack of hetero-cellular coupling via gap junctions that was previously reported (Briggs Boedtkjer et al., 2013). Just as critically, they also highlight the regenerative nature of the lymphatic muscle AP as local depolarization was sufficient to drive a coordinated contraction along the vessel and that a single or few LMCs reaching threshold for AP initiation are sufficient to drive the conducted activity observed at the tissue level.

Conclusions

Our present findings lend further support to the hypothesis that the LMCs are intrinsic pacemakers (van Helden et al., 2006; Mitsui and Hashitani, 2020) and mouse cLVs do not require an ICC-like cell network to drive propagated contractions. These findings also underscore the significance of lymphatic muscle Ca^{2+} handling as the driver of lymphatic pacemaking, which can be compromised in disease states leading to impaired lymphatic contractile activity (Stolarz et al., 2019; Lee et al., 2020; Van et al., 2021). Further studies delineating the specific SR Ca^{2+} release and influx pathways, and the contributions of Ca^{2+} sensitive ion channels are required to develop sophisticated in silico models and

identify potential therapeutic targets to rescue lymphatic pacemaking in lymphedema patients (Olszewski, 2002, 2008).

Limitations

One fundamental assumption underlying our conclusions is that there is a conserved pacemaking pathway and cell type regulating lymphatic collecting vessel contractions across species, specifically pertaining to the capability of lymphatic muscle to maintain pacemaking and coordination despite changes in tissue complexity and cLV wall thickness. It is worth noting that lymphatic collecting vessels in mice have similar pressure-dependent chronotropy and contraction conduction velocity as recorded in rats and human vessels (Castorena-Gonzalez et al., 2018b). These similarities exist despite the fact that mouse lymphatic collecting vessels are typically encircled by a single layer of lymphatic muscle while larger species may have multiple layers of LMCs in the wall. It is possible that vessels with multiple layers of LMCs need a network of ICLC to coordinate their activity. The simplicity in the makeup of the mouse cLV and the use of cell targeting Cre models provide great control over experimental variables, but other cell types may provide coordination of LMC pacemaking in other species where the lymphatic cLV walls are larger and thicker and contain multiple muscle cell layers. Our scRNAseq analysis also is likely biased using ROSAmTmG mice with FACS purification to remove debris and concentrate specific cell types from these pooled small vessels. Larger and more complex cells, with attributes that can be ascribed to ICCs, are more likely to be lost in this methodology (e.g.., depending on the FACS gating parameters) and this procedure can also elicit a stress response in the transcriptome of the analyzed cells. However, we also did not observe long and complex cells, aside from the circumferential LMCs, in our immunofluorescence and recombination reporter imaging experiments. Immediate and early gene expression motifs driven by a stress response may be a component of the differences in sub-clusters that were identified. Future scRNAseq or snRNAseq studies with deeper sequencing will be required to ensure the full transcriptomic heterogeneity is accounted under different cellular stress conditions.

Our data demonstrate that limited staining of a few cell markers alone is insufficient to identify discrete cell populations in the mouse cLVs. Additionally, mRNA expression does not equal protein translation nor guarantee specific function as we did not readily detect endothelial CD34 with immunofluorescence despite detecting transcript; additionally, *PdgfrαCreER*^{TM} mediated deletion of Ano1, Cx45, or Cav1.2 had no effect on cLV pacemaking. Hence, further experimentation is also required to fully characterize expression of multipotent cell markers and function of CD34^{+}PDGFRα^{+}Sca1^{+} cells invested within the mouse cLVs, although this was beyond the scope of this study assessing pacemaker identity. Tangentially, another limitation of our approach pertains to the specificity and recombination efficiency of inducible Cre recombinase models, which can be a notable confounding variable (Chakraborty et al., 2019). We observed that our inducible Cre models led to a degree of nonspecific recombination within the mouse cLV, with the GCaMP6f and ChR2 particularly susceptible to recombination compared to the ROSA26mT/mG reporter. Recombination in multiple cell types was expected with the constitutive Cre models we employed (*Ng2Cre* and *PdgfrαCre*), as vascular and lymphatic muscle precursor cells can transiently express *Nestin*, *Pdgfrα*, and *Ng2* (Hill et al., 2015; Castorena-Gonzalez et al., 2018b; Kenney et al., 2020). We also observed that *PdgfrβCreER*^{T2} drove recombination in a sub population of LMCs and PDGFRα^{+} cells. These appeared to be two distinct populations that only share expression for PDGFRβ based on our scRNAseq dataset but may exist along a continuum of differentiation. PDGFB-PDGFRβ signaling is critical for normal mural cell recruitment to both the blood and lymphatic vasculature (Gaengel et al., 2009; Wang et al., 2017) and proliferating vascular smooth muscle cells and pericytes have both been documented to express PDGFRβ (Andrae et al., 2008; Pitulescu and Adams, 2014). Ideally, novel Cre or combinatorial Cre models that specifically target LMCs or sub populations of LMCs may be developed to further tease out the functional role of these cells.

Materials and Methods

714 **Mice**
715 Wild-type (WT) male mice (25-35 g) on the C57BL/6J background , ROSA26mT/mG reporter
716 (Muzumdar et al., 2007) (Strain#007676), transgenic *PdgfrαCre* (Strain#013148), CSFR1-EGFP
717 (MacGreen) (Sasmono et al., 2003)(Strain#018549), genetically encoded Ca^{2+} sensor GCaMP6f (Chen et
718 al., 2013) (Strain#028865), transgenic *PdgfrαCreER*^{TM} (Kang et al., 2010) (Strain#018280), NG2-Cre (Strain
719 #:008533)(Zhu et al., 2008), and ChR2 /tdTomato fusion mice (Madisen et al., 2012) (Strain#012567) were
720 purchased from The Jackson Laboratory (Bar Harbor, MA, USA). *PdgfrβCreER*^{T2} (Gerl et al., 2015) mice
721 were a gift from Ralf Adams (Mac Planck Institute) and kindly provided by Lorin Olson (Oklahoma
722 Medical Research Foundation) and are currently available at Jax (Strain#029684). The *Myh11CreER*^{T2} mice
723 (Wirth et al., 2008) were a gift from Stefan Offermanns, Max-Planck-Intstitut fur Herz-und
724 Lungendforschung, Bad Nauheim, Germany, and are currently available at Jax (Strain #019079, Y-Linked).
725 c-KitCreER^{T2} mice (Heger et al., 2014) were a gift from Dieter Saur (Technical University of Munich).
726 Prox1-eGFP mice (Choi et al., 2011) were a gift from Young-Kwon Hong (University of Southern
727 California. For genotyping, we isolated genomic DNA from mouse tail clips using the HotSHOT method
728 (Truett et al., 2000). Specific mouse genotypes were confirmed via PCR using 2x PCR Super Master
729 Polymerase Mix (Catalog # B46019, Bimake, Houston, TX) performed as specified by the provider. Mice
730 used for this study were 3-8 months of age. All animal protocols were approved by the University of
731 Missouri Animal Care and Use Committee and conformed to the US Public Health Service policy for the
732 humane care and use of laboratory animals (PHS Policy, 1996).
733
734 **iCre Tamoxifen Induction**
735 Mice harboring *PdgfrαCreER*^{TM}, *PdgfrβCreER*^{T2}, *Myh11CreER*^{T2}, and *cKitCreER*^{T2} were crossed
736 with ROSA26mT/mG mice to generate *PdgfrαCreER*^{TM}-ROSA26mT/mG, *PdgfrβCreER*^{T2}-
737 ROSA26mT/mG, *Myh11CreER*^{T2}-ROSA26mT/mG, and *cKitCreER*^{T2}-ROSA26mT/mG mice,
738 respectively. The resulting iCre-ROSA26mT/mG mice were induced with tamoxifen 2-4 weeks after
739 weaning. Tamoxifen induction was performed via consecutive 100 µL i.p. injections of tamoxifen ranging
740 from 1 to 5 days at concentrations ranging from 0.2 -10 mg/mL in safflower oil, using a titrated induction
741 protocol to determine the extent of recombination in specific cell populations. We used our maximal
742 induction protocol, 100 µL of tamoxifen at 10 mg/mL over 5 consecutive days, for *cKitCreER*^{T2}-GCaMP6f,
743 *Myh11CreER*^{T2}-GCaMP6f, and *PdgfrαCreER*^{TM} -GCaMP6f mice. Due to the paucity of recombined cells
744 in the *cKitCreER*^{T2}-ROSA26mT/mG reporter mice, we used our maximal tamoxifen induction protocol for
745 *cKitCreER*^{T2}-ChR2 mice as this still resulted in the ability to excite single recombined cells.
746 *Myh11CreER*^{T2}-ChR2/tdTomato mice were induced with one 100 µL i.p. injection of tamoxifen at 0.2
747 mg/mL while *PdgfrαCreER*^{TM}-ChR2/tdTomato were induced with 1 injection at 0.4 mg/mL tamoxifen to
748 get mosaic induction sufficient for single cell stimulation. All mice, regardless of induction duration, were
749 given at least 2 weeks to recover following tamoxifen injection.
750
751 **Lymphatic Vessel Isolation**
752 We utilized both popliteal and inguinal-axillary lymphatic collecting vessels (IALVs) in this study,
753 which were isolated as described previously (Zawieja et al., 2018a). In brief, mice were anaesthetized with
754 a cocktail of 100/10 mg/mL ketamine/xylazine and shaved along the flank or the legs for IALVs and
755 popliteal cLVs respectively. The IALV (also referred to as the flank cLV) is located adjacent to the
756 thoracoepigastric vein and connects the inguinal and axillary lymph nodes. A cut was made along the dorsal
757 midline and the skin retracted and pinned out to reveal the thoracoepigastric vascular bed. The
758 thoracoepigastric vascular bed and connected perivascular adipose containing the IALVs vessel was
759 dissected out and pinned onto a Sylgard coated dish in Krebs buffer. Popliteal lymphatic vessels were
760 exposed through a superficial incision in the leg, removed and transferred to the Krebs-albumin filled
761 dissection chamber. After removal, the vessel was carefully cleaned of adipocytes and excess matrix using
762 fine forceps and scissors through micro-dissection. For immunofluorescence, sections containing 2-3 valves
763 were isolated, while smaller IALV sections consisting of 1-2 valves were isolated for GCaMP6f Ca^{2+}
764 imaging. Similarly, popliteal cLVs were isolated (Castorena-Gonzalez et al., 2018a) following an incision

765 along the skin overlying the saphenous vein for contractile function analysis and for ChR2 optogenetic
766 depolarization experiments.

767 **Lymphatic Vessel Isobaric Function**

768 *PdgfrαCreER*^{TM} mice were crossed with *Ano1*$^{fl/fl}$, *Cx45*$^{fl/fl}$, and *Cav1.2*$^{fl/fl}$ mice to generate
769 *PdgfrαCreER*^{TM}*-Ano1*$^{fl/fl}$*, PdgfrαCreER*^{TM}*-Cx45*$^{fl/fl}$*,* and *PdgfrαCreER*^{TM}*-Cav1.2*$^{fl/fl}$ mice. These mice and
770 their respective fl/fl controls were injected with tamoxifen as described above for 5 days and given two
771 weeks to recover. The popliteal vessels were isolated, cleaned, and prepared for isobaric contractile tests
772 as previously reported (Davis et al., 2023). Once equilibrated, inner diameter was tracked over a
773 physiological pressure range (stepped from 3 to 2, 1, 0.5, 3, 5, 8, and 10 cmH_2O) with 2min of recording
774 at each pressure. Following the pressure step protocol the vessels were equilibrated in with Ca^{2+}-free
775 Krebs buffer (3mM EGTA) and diameter at each pressure recorded under passive conditions (DMAX).
776 The contractile parameters end diastolic diameter (EDD), end systolic diameter (ESD), and contraction
777 frequency (FREQ) were recorded with a custom LabVIEW program and the following contractile
778 parameters assessed:

779 1) Contraction Amplitude (AMP) = EDD−ESD

780 2) Normalized Contraction Amplitude = ((EDD−ESD)/DMAX) × 100

781 3) Ejection Fraction (EF) = $(EDD^2-ESD^2)/EDD^2$

782 4) Fractional Pump Flow (FPF) = EF × FREQ

783 5) Tone = ((DMAX−EDD)/DMAX) × 100

784

785 **Methylene Blue Staining**

786 Isolated IALVs sections were transferred into a Krebs-BSA buffer filled 3-mL observation
787 chamber, with a cover slip bottom, and cannulated onto two glass micropipettes (30-80 µm, outer diameter)
788 held in place by pipette holders on a Burg-style V-track mounting system. The pipette holders were attached
789 to a 3-way valve stop cock with polyethylene tubing filled with Krebs-BSA buffer. Vessels were
790 pressurized to approximately 5 cmH_2O by raising the 3-way valve and the vessels were stretched to remove
791 any slack. For methylene blue staining, IALVs from wild type C57Bl6 mice were stained with 50 µM
792 methylene blue in Krebs-BSA buffer for two hours at room temperature and covered in foil to limit light-
793 induced phototoxicity. After the staining period, the vessel chambers were washed three times with Ca^{2+}
794 free PSS to remove methylene blue. Brightfield images and manual Z-stack videos were collected on an
795 inverted Leica DMi1 4X or 20X air objective, or a Leica DMi8 with a 25X water objective or an inverted
796 DMi8 using a Leica Flexacam C1 color camera for image acquisition. Some Methylene blue images were
797 also collected using a color Nikon DS-Fi3 camera. The collected z-stacks were analyzed using Image J and
798 the "Stack Focuser" plugin (https://imagej.nih.gov/ij/plugins/stack-focuser.html). To accentuate the
799 methylene blue stained cells, the color image stack was split into red, green, and blue channel stacks. The
800 blue channel stack was then divided by the green channel stack using the "Image Calculator" function. The
801 resulting 32-bit image was then converted into 16-bit image to permit the use of the Stack Focuser plugin
802 with the 'n kernel value' set to 11.
803

804 **Fluorescence Confocal Imaging**

805 IALVs vessels from each respective iCre-ROSA26mT/mG mouse were prepared in a similar
806 manner (excluding the addition of methylene blue). We performed confocal imaging to acquire z-stacks of
807 7-10 overlapping regions of interests to allow for manual stitching, with 1 µM z-steps (20X) or 0.5 µM

808 steps at 40X. We imaged through to the midpoint of the vessel except when imaging the valve interstitial
809 cells, in which case the entire vessel was imaged. Max projections were made using FIJI. Following live
810 imaging, the vessels were pressurized to 5 cmH_2O and fixed with 4% paraformaldehyde for 30 min at room
811 temperature. IALVs were then washed with PBS containing 0.1% Triton X-100 (PBST) 3 times and
812 blocked for a minimum of 2 hr with Blockaid® (B-10710, ThermoFisher Scientific). IALVs were then
813 stained with the corresponding primary antibodies in BlockAid® Solution: anti-smooth muscle actin
814 (SMA) 1:500 (Sigma, A2547), anti-GFP 1:200 (ThermoFisher, A11122), anti-cKit 1:100 (Cell Signaling,
815 3074), anti-Vimentin 1:100 (Thermofisher , OMA1-06001), anti-desmin 1:200 (Invitrogen, PA5-16705),
816 anti-GFP 1:200 (Abcam, ab13970, anti-CD34 1:200 (Invitrogen, 14-0341-82), anti-PDGFRA 1:200
817 (R&DSystems, AF1062), anti-PDGFRβ 1:200 (eBiosciences, 14-1402-82), anti-calponin 1:500 (Abcam,
818 AB46794), anti-MYH11 1:500 (Abcam, AB124679), anti-Sca1 1:200 (Biolegend, 108101). IALVs were
819 then washed in PBS and incubated overnight with the corresponding donkey secondary antibodies
820 (ThermoFisher®) at 1:200. After a final wash, IALVs were re-cannulated and pressurized for imaging using
821 the aforementioned spinning disk confocal and Hamamatsu Orca Flash4 camera using a 20X air objective
822 (Olympus UplanApo, 0.75) or 40X (Olympus UApo A340, 1.15) water objective. Images were taken as
823 described above, and the resulting stacks were turned into a max projection using FIJI. Colocalization
824 analysis of the max projections of CD34 and PDGFRα was performed using the BIOP JACoP colocalization
825 plugin (Bolte and Cordelieres, 2006) with both Pearson's and Mander's coefficients reported.
826
827 **LMC Dissociation and FACS Collection-**
828 IALVs vessels *PdgfrαCreER^{TM}*-ROSA26mT/mG, *PdgfrβCreER^{T2}*-ROSA26mT/mG,
829 *Myh11CreER^{T2}*-ROSA26mT/mG, Macgreen, and *Prox1-eGFP* mice were dissected and cleaned of excess
830 adventitia and adipose tissue in Krebs buffer. Isolated vessels were then transferred into a low Ca^{2+} PSS
831 solution supplemented with 0.1 mg/mL bovine serum albumin (BSA, Amersham Life Science, Arlington
832 Heights, IL). Primary LMCs were collected by enzymatic dissociation of IALVs. The dissected vessels
833 were cleaned in room temperature Krebs-BSA buffer and then transferred into a 1-mL tube of low-Ca^{2+}
834 PSS on ice, washed, and equilibrated for 10 min. Vessels were then digested in low-Ca^{2+} PSS with 26 U/mL
835 papain (Sigma, St. Louis, MO) and 1 mg/mL dithioerythritol for 30 min at 37°C with gentle agitation every
836 few minutes. This solution was then decanted and replaced with low-Ca^{2+} PSS with containing 1.95
837 collagenase H (U/mL, Sigma), 1.8 mg/mL collagenase F (Sigma), and 1mg/mL elastase (Worthington
838 LS00635) and incubated for 3 - 5 min at 37°C. The mixture was then spun down at 1000 rpm for 4 min, the
839 digestion buffer removed, and replaced with low-Ca^{2+} PS. This process was repeated twice to remove
840 residual digestion buffer. The vessel was then triturated with a fire-polished Pasteur pipette to dissociate
841 the cells into a single cell suspension, passed through a Falcon cap strainer (35 µm), and resuspended in
842 ice-cold low-Ca^{2+} PSS for sorting. For iCre-ROSA26mT/mG mice, GFP^+RFP^- cells or GFP^+ cells from
843 Macgreen and *Prox1-eGFP* mice were then FACS purified straight into RNA isolation buffer for RT-PCR
844 analysis. FACs was performed with a Beckman-Coulter MoFlo XDP instrument using an excitation laser
845 (488 m) and emission filter (530/40 m). Sorting was performed using 70-µm nozzle at a sheath pressure of
846 45 p.s.i. and sort rate of 100 events/s and with an efficiency of >90%. To maximize cell yield, we isolated
847 both the left and right full-length IALVs vessels from 2 mice for digestions and subsequent FACS
848 collection. For *Myh11CreER^{T2}*-ROSA26mT/mG and *PdgfrαCreER^{TM}*-ROSA26mT/mG, the yield averaged
849 1000-2000 cells per mouse. For *Prox1-eGFP* mice, LEC yield was typically 1500-2000 cells per mouse.
850
851 **RT-PCR Profiling of FACS Purified Cells-** Total RNA was extracted from FACS purified GFP^+
852 cells from the isolated IALVs vessels using the Arcturus PicoPure RNA isolation kit (ThermoFisher
853 Scientific, Waltham, MA) per the listed instructions. Prior to elution in 20 µl of water, on-column DNAse
854 digestion (Qiagen, Valencia, CA) was performed to ensure removal of genomic DNA contaminants. RNA
855 was converted into cDNA using SuperScript III First-Strand Synthesis System (Thermo Fisher Scientific,
856 Waltham, MA) using oligo (dT) and random hexamer priming following the manufacturer's protocol. Each
857 RT reaction used approximately 50-100 cells worth of RNA based on the sorted cells count number. Our
858 PCR reaction mixture contained first-strand cDNA as the template, 2 mM $MgCl_2$, 0.25 µM primers, 0.2

859 mM deoxynucleotide triphosphates; and GoTaq® Flexi DNA polymerase (Promega, Madison, WI). The
860 PCR program comprised an initial denaturation step at 95°C for four min; followed by 35 repetitions of the
861 following cycle: denaturation (94° C, 30 s), annealing (58° C, 30 s), and extension (72° C, 30 s). This was
862 followed by a final elongation step for 5 min at 72° C. PCR amplification products were separated on a 2%
863 agarose gel by electrophoresis, stained with SYBR-Safe (Thermo Fisher Scientific, Waltham, MA), and
864 visualized by UV trans-illumination. All primers were designed to amplify an intron-spanning region.
865 Endpoint RT-PCR Primer sequences, amplicon size, accession numbers, and source are listed in Table 1.
866
867 **scRNASeq Analysis of Mouse IALVs**
868 For scRNASeq analyses of isolated IALVs we used a total of 10 *Rosa26mTmG* mice, without Cre
869 and without tamoxifen treatment, with equivalent representation of sex (5 males and 5 females). Full length
870 IALVs from both the left and right side of each *ROSA26mTmG* mouse were isolated and cleaned of
871 excessive matrix and adipose tissue. Isolated vessels were digested into single cell suspensions as described
872 above and the cells were kept on ice following single cell suspension until all the tissues had been processed.
873 Cells from all vessels were combined and sorted for tdTomato expression to remove debris and concentrate
874 the cells for downstream single cell 3' RNA-Seq libraries creation with 10x Genomics Chromium Chip and
875 Chromium Next GEM Single Cell 3' RNA-Seq reagents. Samples were sequenced with the NovaSeq 6000
876 S4-PE100 flow cell.
877
878 Mus musculus genome GRCm39 and annotation GTF (v106) from Ensembl
879 (https://useast.ensembl.org/Mus_musculus/Info/Index) were used to build the reference index and the reads
880 were processed using Cell Ranger (v7.0.1; Zheng et al., 2017) with default parameters. The quality control
881 and filtering steps were performed using R (v4.2.1; https://www.r-project.org/). Ambient RNA was
882 removed from the Cell Ranger output with SoupX (Young and Behjati, 2020). Doublet score for each cell
883 was estimated using scDBlFinder (v1.12.0; Germain et al., 2021). Non-expressed genes (sum zero across
884 all samples) and low-quality cells (>10% mitochondrial genes, < 500 genes, < 1,000 UMIs per cell and
885 doublet score <0.5) were removed with custom R scripts. Cells passing filtering were normalized/scaled
886 (SCTransformation), dimensionally reduced (t-distributed stochastic neighbor embedding (t-SNE) and
887 uniform manifold approximation and projection (UMAP)) clustered, and hierarchically analyzed with
888 Seurat (Hao et al., 2021; Hao et al., 2024) with default parameters. Marker gene expression profile on cell
889 clusters and gene co-expression was visualized using Seurat and ShinyCell R application (Ouyang et al.,
890 2021). The full scRNAseq raw dataset has been uploaded to the NIH GEO under the accession number
891 GSE277843.. Differential gene expression within subclusters of LECs, LMCs, and AdvCs was performed
892 using Seurat's "Find Markers" function and with a minimum of either 40% or 50% cell expression and log
893 fold change minimum of 1. In the volcano plot for LEC subcluster 8 differential gene expression, listed
894 genes were had a cutoff of a log fold change of 2 or -2 to be displayed on the plot.
895
896 ***Ex vivo* Ca^{2+} imaging with the genetically encoded GCaMP6f Indicator**
897 *cKitCreER^{T2}*, *Myh11CreER^{T2}*, and *PdgfrαCreER^{TM}* mice were crossed with GCaMP6f mice in a
898 similar manner as described for ROSA26mT/mG. *cKitCreER^{T2}*-GCaMP6f, *PdgfrαCreER^{TM}*-GCaMP6f, and
899 *Myh11CreER^{T2}*-GCaMP6f were induced with tamoxifen (10 mg/mL) for 5 consecutive days by i.p.
900 injection. IALVs isolated from *cKitCreER^{T2}*-GCaMP6f, *PdgfrαCreER^{TM}*-GCaMP6f, and *Myh11CreER^{T2}*-
901 GCaMP6f were cannulated as described above. The cannulated vessel, with micropipette holders,
902 observation chamber and V-track mounting system, was transferred to the stage of the spinning disk
903 confocal with a Prime95B scMOS camera (Photometrics), a Cascade II EMCCD (Photometrics), or an
904 Ixon888 EMCCD camera (Andor) for Ca^{2+} imaging (Castorena-Gonzalez et al., 2018b). Pressures for the
905 input and output cannula were connected to a T-junction which was set briefly to 8 cmH_2O and the vessel
906 lengthened to remove axial slack. A peristaltic pump maintained constant perfusion of the observation
907 chamber with Krebs buffer at a rate of 0.5 mL/min while the vessel equilibrated at 37°C for 30-60 min with
908 pressures set to 3 cmH_2O. Spontaneous contractions were allowed to stabilize over a period of 30 min and
909 then were blunted with 2 μM wortmannin to limit movement associated with contractions during Ca^{2+}

910 imaging. A Windows-based computer was used to digitize the pressure transducer signals and video image
911 of the vessel from a firewire camera at 30-40 Hz (Davis et al., 2012). A custom-written LabVIEW program
912 (National Instruments; Austin, TX) detected the inner diameter of the vessel from the video (Davis et al.,
913 2011). Once contractions were <5 µm in amplitude, Ca^{2+} recordings were made at 20FPS for 20-40 s.
914
915 **Ca^{2+} Imaging and Analysis in IALVs Over the Contraction Cycle**
916 Background noise was determined by using the histogram feature of FIJI in a rectangle in a region
917 of the field of view without sample. This value was subtracted from the entire field of view. In some cases,
918 the vessel movement due to contraction was offset with video stabilization with the FIJI plugin Image
919 Stabilizer. A max projection was used to create non-overlapping ROIs of $GCaMP6f^{+}$ cells for each iCre-
920 GCaMp6f IALV. From these cell ROIs, the "reslice z" function was used to create pseudo-linescan STMs,
921 which were divided by their baseline values to obtain F/F_0 values for each individual cell. At least 3 cells,
922 except in the case of 1 *cKitCreER^{T2}*-GCaMp6f IALV, in which only two cells were observed, were analyzed
923 in this manner for each vessel segment. Max projections of the image stack were then used to create non-
924 overlapping cell masks of 3-5 muscle cells per field of view of one vessel. Ca^{2+} traces for those cells
925 contained 5-10 contraction cycles and Ca^{2+} transients and were characterized for peak intensity (expressed
926 as a baseline-referenced ratio, F/F_0), frequency, and duration in seconds.
927
928 **Analysis of Subcellular Ca^{2+} Transients in *Myh11CreER^{T2}*-GCaMP6f IALVs**
929 For *Myh11CreER^{T2}*-We performed Ca^{2+} imaging as above in the presence of 1 µM nifedipine to
930 stop the "Ca^{2+} flashes" associated with APs (Zawieja et al., 2018a) and focus on the subcellular activity at
931 3 different experimental pressures of 0.5, 2, and 5 cmH_2O. For this protocol, we used a particle analysis
932 approach to analyze all Ca^{2+} transients in the field of view. Ca^{2+} transients in intact vessels were quantified
933 by particle analysis as previously described (Drumm et al., 2017; Drumm et al., 2019). Movies of Ca^{2+}
934 transients in intact vessels were imported into custom built Volumetry software (version G8d) and
935 background subtracted. Movies were smoothed using a Gaussian filter: 1.5 x 1.5 mM, StdDev 1.0). Raw
936 Ca^{2+} transients were converted to Ca^{2+} particles (PTCLs) using a flood-fill algorithm as previously
937 described (Drumm et al., 2017; Drumm et al., 2019). PTCLs <10 μM^2 were rejected to facilitate the removal
938 of noise and then the total PTCL area and PTCL count could be tabulated for each recording.
939
940 **Membrane Potential Recordings in IALVs**
941 Mouse IALVs were isolated and cleaned as described above. IALVs were pressurized in our
942 isobaric myography apparatus and allowed to equilibrate to ensure typical contractile activity was evident.
943 A bolus of wortmannin at 2 µM was then applied to the bath to blunt contraction amplitude below 5 microns.
944 Intracellular recordings of lymphatic muscle were made with microelectrodes (250–300 MΩ) filled with 1
945 M KCl and an SEC-05x amplifier (NPI) connected to a Grass S48 stimulator, viewed with a Tektronix
946 TDS3052 digital oscilloscope. Membrane potential and diameter were simultaneously recorded using a
947 custom Labview program. Membrane potential and APS were allowed to stabilize and then pressure was
948 slowly raised from 0.5 cmH_2O to 2 cmH_2O and then 5cmH_2O. In some cases, the electrode dislodged due
949 to the intrinsic contractions of the vessel or wall displacement as pressure was modulated. In these
950 situations, we attempted to re-impale the cell or one of the neighboring cells. Only vessels in which a
951 recording with a minimum of 3 stable APs was successfully made at 2 of the 3 experimental pressures were
952 used for subsequent analysis.
953
954 We also confirmed LMC impalement using microelectrode filled with 1 M KCl and (100 µg/ml) Biocytin-
955 AF488 (A12924, ThermoFisher) to label impaled cells that displayed APs, over a 10-minute recording
956 period. Following the impalement and loading with Biocytin-AF488 the vessel was transferred to our
957 imaging apparatus for confocal imaging and 3D reconstruction using the Andor Dragonfly 200 and
958 IMARIS. Image stacks were taken with a 25x water objective at 0.5-micron intervals throughout the
959 diameter of the vessel.
960

961 **Light Activation of ChR2 to stimulate Popliteal Collecting Lymphatic Vessel Contractions**
962 As the IALV has a nearly continuous contractile cycle, we utilized the popliteal vessel for its much
963 slower contraction frequency in the experiments testing our ability to trigger a propagated contraction upon
964 stimulation of the enforced expression of ChR2. Popliteal vessels were isolated from *cKitCreER*^{T2}-
965 ChR2/tdTomato, *PdgfrαCreER*^{TM} -ChR2/tdTomato, or *Myh11CreER*^{T2}-ChR2/tdTomato mice as previously
966 described (Scallan and Davis, 2013), although we intentionally retained some connective tissue and adipose
967 tissue to ensure we had a sufficient population of recombined cells to test in the adventitia layer of the
968 vessel. Contractions were allowed to stabilize over a 30-min equilibration period with pressure set to 3
969 cmH_2O. If basal contraction frequency was too high, we applied pinacidil to the bath in 100 nM increments,
970 without exceeding 600 nM, to further slow contraction frequency to around 6 contractions per minute.
971 Pinacidil at sub 1 µM doses can slow contraction frequency without causing overt hyperpolarization of
972 membrane potential (Davis et al., 2020). Supplemental 100 nM doses of pinacidil were applied throughout
973 the experiment to maintain a spontaneous contraction frequency below 6 per minute to allow ample diastolic
974 time for ChR2 stimulation. Throughout this protocol the popliteal was allowed to contract spontaneously
975 to ensure we had not overly inhibited APs by the pacemaking cells with pinacidil. Occasionally,
976 spontaneous contractions occurred just prior to light-evoked contractions, resulting in a potential false
977 positive, so we performed multiple stimulations over a period of 5 - 10 min, typically waiting at least 3 s
978 after any spontaneous contraction before stimulating. Care was made to align the light fiber in such a way
979 that only part of the vessel would be directly illuminated and so target cells of interest would be directly
980 activated by 473 nm light using a Laser diode (Doric LD Fiber Light Source, Quebec, Canada), through an
981 optical probe with a 10-µm tip (Doric, OPT_200_0.22.010). To further limit the excitation field, the optical
982 probe was coated with black acrylic paint using an eyelash brush so that the uncoated opening was ~2-3
983 µm. With the probe positioned within 5 µm of one side of the vessel wall, the spread of light covered an
984 area ~10-100 µm wide on the back side of the vessel (depending on the diode amplitude setting). Light
985 pulses, 200 ms in length, were triggered by a Grass S9 stimulator (Harvard Apparatus, Holliston, MA)
986 connected to the external TTL input of the laser diode. Pulse amplitude was adjusted between 40-90 mA
987 using the Laser Diode Module Driver (Doric). A contraction was considered to be triggered if it occurred
988 within 50ms of stimulation. We performed photo-stimulation from 2-4 sites within each vessel, with 6-14
989 stimulations per site. If a photo-stimulation was triggered incidentally after the initiation of a "spontaneous
990 contraction" it was discarded from the analysis. For *Myh11CreER*^{T2}-ChR2-tdTomato 6 vessels from 3
991 separate mice were tested. For *PdgfrαCreER*^{TM}-ChR2-tdTomato 6 vessels from 4 separate mice were tested
992 with a max of two vessels per mouse. For *cKitCreER*^{T2}- ChR2-tdTomato 7 vessels from 3 separate mice
993 were assessed. Diameter was recorded to align photo-activation with the contraction cycle in a custom
994 Labview program.
995
996 **Solutions and Chemicals**.
997 Krebs buffer was composed of (in mM): 146.9 NaCl, 4.7 KCl, 2 $CaCl_2$, 1.2 $MgSO_4$, 1.2
998 NaH_2PO_4•H_2O, 3 $NaHCO_3$, 1.5 NaHEPES, and 5 d-glucose (pH = 7.4 at 37°C). Krebs-BSA buffer was
999 prepared with the addition of 0.5% (w/v) bovine serum albumin (BSA) while Krebs Ca^{2+}-free replaced
1000 $CaCl_2$ with 3mM EGTA. Tamoxifen was dissolved to 10mg/ml in a Safflower Oil-Ethanol (95%-5% v/v)
1001 solution with rocking agitation, separated into aliquots, and stored at -20 °C. Wortmannin was dissolved in
1002 DMSO to a stock solution of 1 mM. Pinacidil was dissolved in DMSO to a stock concentration of 1 µM.
1003 Nifedipine was dissolved in DMSO to a stock concentration of 1 mM. All chemicals were obtained from
1004 Sigma (St. Louis, MO), except for BSA (US Biochemicals; Cleveland, OH), $MgSO_4$ and NaHEPES (Fisher
1005 Scientific; Pittsburgh, PA).

1006 **Statistical Tests**

1007 Statistical differences in the isobaric contractile tests for popliteal cLVs isolated from
1008 *PdgfrαCreER*^{TM}-*Ano1*$^{fl/fl}$, *PdgfrαCreER*^{TM}-*Cx45*$^{fl/fl}$, and *PdgfrαCreER*^{TM}-*Cav1.2*$^{fl/fl}$ mice over the various

contractile parameters were assessed via 1) repeated measures two-way ANOVAs with Sidak's multiple comparison tests performed using Prism9 (Graphpad). Data are plotted as mean ± SEM and significance determined at $p < 0.05$ and $0.10 > p > 0.05$ were reported. Data from cLVs in which a negative tone value was recorded at any pressure, which typically indicated incomplete passivation or bubbles in the cannula, were not included in the tone analysis. Vessels that failed to contract at a given pressure had no value recorded for ejection fraction or normalized amplitude and REML mixed effects model was used in place of repeated measures 2-way ANOVA. We used a categorical Chi-squared statistical test for the experiments assessing our ability to trigger a contraction with activation of ChR2+ cells. Ca^{2+} particle area and frequency was compared using 1-way ANOVA with Tukey's post-hoc test. Significance was determined at a p value of < 0.05. A mixed effects analysis with Tukey's multiple comparison post-hoc test was used to compare AP parameters across pressure using Prism9 (Graphpad).

Acknowledgements
We would like to thank Stefan Offermanns for donation of the *Myh11CreER*^{T2} mice, Klaus Willecke for his donation of Cx45$^{f/f}$ mice, Dieter Sauer for his donation of *cKitCreER*^{T2} mice, Ralph Adams for his donation of the *PdgfrβCreER*^{T2} mice and to Young Hong (University of Southern California) for his donation of the *Prox1-eGFP* mice (Choi et al., 2011).

Author contributions: S.D. Zawieja, J.A. Castorena-Gonzalez and M. J. Davis conceived and designed the experiments. S.D. Zawieja, S.E. Broyhill, J.A. Castorena-Gonzalez, H.J. Kim, B. Drumm, M. Li, C.E. Norton, and M.J. Davis performed the studies, collected, and analyzed and interpreted the data. S.D. Zawieja and M.J. Davis drafted the manuscript and all authors participated in critically revising the manuscript for intellectual concepts and content. All authors have approved the final draft of the manuscript, and their contributions qualify them as authors.

The authors declare no competing financial interests. This work was supported by NIH HL-122608 and HL-122578 to MJD, HL-143198 and HL-175083 SDZ, and HL-141143 and HL-168568 to JAC-G, and AHA CDA-931652 to CEN. A. Patro was supported by MizzouForward Undergraduate Research Fellow.

Data availability
Single-cell mRNA sequencing data generated to support this study have been deposited in NCBI GEO under accession number GEO: GSE277843. The authors declare that all other data supporting the findings of this study are available within the paper, its supplementary information files, and the uploaded scRNAseq dataset.

References

Aalkjaer, C., D. Boedtkjer, and V. Matchkov. 2011. Vasomotion - what is currently thought? *Acta Physiol (Oxf)*. 202:253-269.
Andrae, J., R. Gallini, and C. Betsholtz. 2008. Role of platelet-derived growth factors in physiology and medicine. *Genes Dev*. 22:1276-1312.
Andrzejewska, A., B. Lukomska, and M. Janowski. 2019. Concise Review: Mesenchymal Stem Cells: From Roots to Boost. *Stem Cells*. 37:855-864.

1058 Atakpa-Adaji, P., A. Ivanova, K. Kujawa, and C.W. Taylor. 2024. KRAP regulates mitochondrial Ca2+
1059 uptake by licensing IP3 receptor activity and stabilizing ER-mitochondrial junctions. *J Cell Sci*.
1060 137.
1061 Baker, S.A., B.T. Drumm, D. Saur, G.W. Hennig, S.M. Ward, and K.M. Sanders. 2016. Spontaneous
1062 Ca(2+) transients in interstitial cells of Cajal located within the deep muscular plexus of the
1063 murine small intestine. *J Physiol*. 594:3317-3338.
1064 Baker, S.A., S.J. Hwang, P.J. Blair, C. Sireika, L. Wei, S. Ro, S.M. Ward, and K.M. Sanders. 2021a.
1065 Ca(2+) transients in ICC-MY define the basis for the dominance of the corpus in gastric
1066 pacemaking. *Cell Calcium*. 99:102472.
1067 Baker, S.A., W.A. Leigh, G. Del Valle, I.F. De Yturriaga, S.M. Ward, C.A. Cobine, B.T. Drumm, and
1068 K.M. Sanders. 2021b. Ca(2+) signaling driving pacemaker activity in submucosal interstitial cells
1069 of Cajal in the murine colon. *Elife*. 10.
1070 Basciani, S., S. Mariani, M. Arizzi, M. Brama, A. Ricci, C. Betsholtz, C. Bondjers, G. Ricci, A. Catizone,
1071 M. Galdieri, G. Spera, and L. Gnessi. 2004. Expression of platelet-derived growth factor (PDGF)
1072 in the epididymis and analysis of the epididymal development in PDGF-A, PDGF-B, and PDGF
1073 receptor beta deficient mice. *Biol Reprod*. 70:168-177.
1074 Behringer, E.J., J.P. Scallan, M. Jafarnejad, J.A. Castorena-Gonzalez, S.D. Zawieja, J.E. Moore, Jr., M.J.
1075 Davis, and S.S. Segal. 2017. Calcium and electrical dynamics in lymphatic endothelium. *J*
1076 *Physiol*. 595:7347-7368.
1077 Benoit, J.N., D.C. Zawieja, A.H. Goodman, and H.J. Granger. 1989. Characterization of intact mesenteric
1078 lymphatic pump and its responsiveness to acute edemagenic stress. *Am J Physiol*. 257:H2059-
1079 2069.
1080 Boedtkjer, D.M., V.V. Matchkov, E. Boedtkjer, H. Nilsson, and C. Aalkjaer. 2008. Vasomotion has
1081 chloride-dependency in rat mesenteric small arteries. *Pflugers Arch*. 457:389-404.
1082 Bolte, S., and F.P. Cordelieres. 2006. A guided tour into subcellular colocalization analysis in light
1083 microscopy. *J Microsc*. 224:213-232.
1084 Bridenbaugh, E.A., I.T. Nizamutdinova, D. Jupiter, T. Nagai, S. Thangaswamy, V. Chatterjee, and A.A.
1085 Gashev. 2013a. Lymphatic muscle cells in rat mesenteric lymphatic vessels of various ages.
1086 *Lymphat Res Biol*. 11:35-42.
1087 Bridenbaugh, E.A., W. Wang, M. Srimushnam, W.E. Cromer, S.D. Zawieja, S.E. Schmidt, D.C. Jupiter,
1088 H.C. Huang, V. Van Buren, and D.C. Zawieja. 2013b. An immunological fingerprint
1089 differentiates muscular lymphatics from arteries and veins. *Lymphat Res Biol*. 11:155-171.
1090 Briggs Boedtkjer, D., J. Rumessen, U. Baandrup, M. Skov Mikkelsen, N. Telinius, H. Pilegaard, C.
1091 Aalkjaer, and V. Hjortdal. 2013. Identification of interstitial Cajal-like cells in the human thoracic
1092 duct. *Cells Tissues Organs*. 197:145-158.
1093 Buechler, M.B., R.N. Pradhan, A.T. Krishnamurty, C. Cox, A.K. Calviello, A.W. Wang, Y.A. Yang, L.
1094 Tam, R. Caothien, M. Roose-Girma, Z. Modrusan, J.R. Arron, R. Bourgon, S. Muller, and S.J.
1095 Turley. 2021. Cross-tissue organization of the fibroblast lineage. *Nature*. 593:575-579.
1096 Castorena-Gonzalez, J.A., M. Li, and M.J. Davis. 2020. Effects of Elevated Downstream Pressure and the
1097 Role of Smooth Muscle Cell Coupling through Connexin45 on Lymphatic Pacemaking.
1098 *Biomolecules*. 10.
1099 Castorena-Gonzalez, J.A., J.P. Scallan, and M.J. Davis. 2018a. Methods for Assessing the Contractile
1100 Function of Mouse Lymphatic Vessels Ex Vivo. *Methods in molecular biology*. 1846:229-248.
1101 Castorena-Gonzalez, J.A., S.D. Zawieja, M. Li, R.S. Srinivasan, A.M. Simon, C. de Wit, R. de la Torre,
1102 L.A. Martinez-Lemus, G.W. Hennig, and M.J. Davis. 2018b. Mechanisms of Connexin-Related
1103 Lymphedema. *Circ Res*. 123:964-985.
1104 Chakraborty, R., F.Z. Saddouk, A.C. Carrao, D.S. Krause, D.M. Greif, and K.A. Martin. 2019. Promoters
1105 to Study Vascular Smooth Muscle. *Arterioscler Thromb Vasc Biol*. 39:603-612.
1106 Chakraborty, S., S.D. Zawieja, W. Wang, Y. Lee, Y.J. Wang, P.Y. von der Weid, D.C. Zawieja, and M.
1107 Muthuchamy. 2015. Lipopolysaccharide modulates neutrophil recruitment and macrophage

polarization on lymphatic vessels and impairs lymphatic function in rat mesentery. *Am J Physiol Heart Circ Physiol*.ajpheart 00467 02015.

Chatterjee, V., and A.A. Gashev. 2012. Aging-associated shifts in functional status of mast cells located by adult and aged mesenteric lymphatic vessels. *Am J Physiol Heart Circ Physiol*. 303:H693-702.

Chen, T.W., T.J. Wardill, Y. Sun, S.R. Pulver, S.L. Renninger, A. Baohan, E.R. Schreiter, R.A. Kerr, M.B. Orger, V. Jayaraman, L.L. Looger, K. Svoboda, and D.S. Kim. 2013. Ultrasensitive fluorescent proteins for imaging neuronal activity. *Nature*. 499:295-300.

Cheng, X., J. Liu, M. Asuncion-Chin, E. Blaskova, J.P. Bannister, A.M. Dopico, and J.H. Jaggar. 2007. A novel Ca(V)1.2 N terminus expressed in smooth muscle cells of resistance size arteries modifies channel regulation by auxiliary subunits. *J Biol Chem*. 282:29211-29221.

Choi, I., H.K. Chung, S. Ramu, H.N. Lee, K.E. Kim, S. Lee, J. Yoo, D. Choi, Y.S. Lee, B. Aguilar, and Y.K. Hong. 2011. Visualization of lymphatic vessels by Prox1-promoter directed GFP reporter in a bacterial artificial chromosome-based transgenic mouse. *Blood*. 117:362-365.

Clayton, D.R., W.G. Ruiz, M.G. Dalghi, N. Montalbetti, M.D. Carattino, and G. Apodaca. 2022. Studies of ultrastructure, gene expression, and marker analysis reveal that mouse bladder PDGFRA(+) interstitial cells are fibroblasts. *Am J Physiol Renal Physiol*. 323:F299-F321.

Cobine, C.A., E.E. Hannah, M.H. Zhu, H.E. Lyle, J.R. Rock, K.M. Sanders, S.M. Ward, and K.D. Keef. 2017. ANO1 in intramuscular interstitial cells of Cajal plays a key role in the generation of slow waves and tone in the internal anal sphincter. *J Physiol*. 595:2021-2041.

Davis, M.J., J.A. Castorena-Gonzalez, H.J. Kim, M. Li, M. Remedi, and C.G. Nichols. 2023. Lymphatic contractile dysfunction in mouse models of Cantu Syndrome with K(ATP) channel gain-of-function. *Function (Oxf)*. 4:zqad017.

Davis, M.J., H.J. Kim, M. Li, and S.D. Zawieja. 2022. A vascular smooth muscle-specific integrin-alpha8 Cre mouse for lymphatic contraction studies that allows male-female comparisons and avoids visceral myopathy. *Front Physiol*. 13:1060146.

Davis, M.J., H.J. Kim, S.D. Zawieja, J.A. Castorena-Gonzalez, P. Gui, M. Li, B.T. Saunders, B.H. Zinselmeyer, G.J. Randolph, M.S. Remedi, and C.G. Nichols. 2020. Kir6.1-dependent KATP channels in lymphatic smooth muscle and vessel dysfunction in mice with Kir6.1 gain-of-function. *J Physiol*.

Davis, M.J., E. Rahbar, A.A. Gashev, D.C. Zawieja, and J.E. Moore, Jr. 2011. Determinants of valve gating in collecting lymphatic vessels from rat mesentery. *Am J Physiol Heart Circ Physiol*. 301:H48-60.

Davis, M.J., J.P. Scallan, J.H. Wolpers, M. Muthuchamy, A.A. Gashev, and D.C. Zawieja. 2012. Intrinsic increase in lymphangion muscle contractility in response to elevated afterload. *Am J Physiol Heart Circ Physiol*. 303:H795-808.

Drumm, B.T., G.W. Hennig, S.A. Baker, and K.M. Sanders. 2019. Applications of spatio-temporal mapping and particle analysis techniques to quantify intracellular Ca 2+ signaling in situ. *Journal of Visualized Experiments*. 2019:1-13.

Drumm, B.T., G.W. Hennig, M.J. Battersby, E.K. Cunningham, T.S. Sung, S.M. Ward, K.M. Sanders, and S.A. Baker. 2017. Clustering of Ca2+ transients in interstitial cells of Cajal defines slow wave duration. *The Journal of General Physiology*. 149:703-725.

Drumm, B.T., B.E. Rembetski, C.A. Cobine, S.A. Baker, G.P. Sergeant, M.A. Hollywood, K.D. Thornbury, and K.M. Sanders. 2018. Ca(2+) signalling in mouse urethral smooth muscle in situ: role of Ca(2+) stores and Ca(2+) influx mechanisms. *J Physiol*. 596:1433-1466.

Engeset, A., W. Olszewski, P.M. Jaeger, J. Sokolowski, and L. Theodorsen. 1977. Twenty-four hour variation in flow and composition of leg lymph in normal men. *Acta physiologica Scandinavica*. 99:140-148.

Ferrusi, I., J. Zhao, D. van Helden, and P.Y. von der Weid. 2004. Cyclopiazonic acid decreases spontaneous transient depolarizations in guinea pig mesenteric lymphatic vessels in endothelium-dependent and -independent manners. *Am J Physiol Heart Circ Physiol*. 286:H2287-2295.

1158 Forte, E., M. Ramialison, H.T. Nim, M. Mara, J.Y. Li, R. Cohn, S.L. Daigle, S. Boyd, E.G. Stanley, A.G.
1159 Elefanty, J.T. Hinson, M.W. Costa, N.A. Rosenthal, and M.B. Furtado. 2022. Adult mouse
1160 fibroblasts retain organ-specific transcriptomic identity. *Elife*. 11.
1161 Gaengel, K., G. Genove, A. Armulik, and C. Betsholtz. 2009. Endothelial-mural cell signaling in vascular
1162 development and angiogenesis. *Arterioscler Thromb Vasc Biol*. 29:630-638.
1163 Gashev, A.A., M.J. Davis, M.D. Delp, and D.C. Zawieja. 2004. Regional variations of contractile activity
1164 in isolated rat lymphatics. *Microcirculation*. 11:477-492.
1165 Gashev, A.A., M.J. Davis, and D.C. Zawieja. 2002. Inhibition of the active lymph pump by flow in rat
1166 mesenteric lymphatics and thoracic duct. *J Physiol*. 540:1023-1037.
1167 Geng, X., B. Cha, M.R. Mahamud, K.C. Lim, R. Silasi-Mansat, M.K.M. Uddin, N. Miura, L. Xia, A.M.
1168 Simon, J.D. Engel, H. Chen, F. Lupu, and R.S. Srinivasan. 2016. Multiple mouse models of
1169 primary lymphedema exhibit distinct defects in lymphovenous valve development. *Dev Biol*.
1170 409:218-233.
1171 Gerl, K., L. Miquerol, V.T. Todorov, C.P. Hugo, R.H. Adams, A. Kurtz, and B. Kurt. 2015. Inducible
1172 glomerular erythropoietin production in the adult kidney. *Kidney Int*. 88:1345-1355.
1173 Gomez-Pinilla, P.J., S.J. Gibbons, M.R. Bardsley, A. Lorincz, M.J. Pozo, P.J. Pasricha, M. Van de Rijn,
1174 R.B. West, M.G. Sarr, M.L. Kendrick, R.R. Cima, E.J. Dozois, D.W. Larson, T. Ordog, and G.
1175 Farrugia. 2009. Ano1 is a selective marker of interstitial cells of Cajal in the human and mouse
1176 gastrointestinal tract. *Am J Physiol Gastrointest Liver Physiol*. 296:G1370-1381.
1177 Gonzalez-Loyola, A., E. Bovay, J. Kim, T.W. Lozano, A. Sabine, F. Renevey, S. Arroz-Madeira, A.
1178 Rapin, T.P. Wypych, G. Rota, S. Durot, D. Velin, B. Marsland, G. Guarda, M. Delorenzi, N.
1179 Zamboni, S.A. Luther, and T.V. Petrova. 2021. FOXC2 controls adult lymphatic endothelial
1180 specialization, function, and gut lymphatic barrier preventing multiorgan failure. *Sci Adv*. 7.
1181 Grainger, N., C.C. Shonnard, S.K. Quiggle, E.B. Fox, H. Presley, R. Daugherty, M.C. Shonnard, B.T.
1182 Drumm, and K.M. Sanders. 2022. Propagation of Pacemaker Activity and Peristaltic Contractions
1183 in the Mouse Renal Pelvis Rely on Ca(2+)-activated Cl(-) Channels and T-Type Ca(2+)
1184 Channels. *Function (Oxf)*. 3:zqac041.
1185 Hald, B.O., J.A. Castorena-Gonzalez, S.D. Zawieja, P. Gui, and M.J. Davis. 2018. Electrical
1186 Communication in Lymphangions. *Biophys J*. 115:936-949.
1187 Hao, Y., S. Hao, E. Andersen-Nissen, W.M. Mauck, 3rd, S. Zheng, A. Butler, M.J. Lee, A.J. Wilk, C.
1188 Darby, M. Zager, P. Hoffman, M. Stoeckius, E. Papalexi, E.P. Mimitou, J. Jain, A. Srivastava, T.
1189 Stuart, L.M. Fleming, B. Yeung, A.J. Rogers, J.M. McElrath, C.A. Blish, R. Gottardo, P. Smibert,
1190 and R. Satija. 2021. Integrated analysis of multimodal single-cell data. *Cell*. 184:3573-3587
1191 e3529.
1192 Hao, Y., T. Stuart, M.H. Kowalski, S. Choudhary, P. Hoffman, A. Hartman, A. Srivastava, G. Molla, S.
1193 Madad, C. Fernandez-Granda, and R. Satija. 2024. Dictionary learning for integrative,
1194 multimodal and scalable single-cell analysis. *Nat Biotechnol*. 42:293-304.
1195 Hashitani, H., R. Mitsui, S. Masaki, and D.F. Van Helden. 2015. Pacemaker role of pericytes in
1196 generating synchronized spontaneous Ca2+ transients in the myenteric microvasculature of the
1197 guinea-pig gastric antrum. *Cell Calcium*. 58:442-456.
1198 Heger, K., B. Seidler, J.C. Vahl, C. Schwartz, M. Kober, S. Klein, D. Voehringer, D. Saur, and M.
1199 Schmidt-Supprian. 2014. CreER(T2) expression from within the c-Kit gene locus allows efficient
1200 inducible gene targeting in and ablation of mast cells. *Eur J Immunol*. 44:296-306.
1201 Hill, R.A., L. Tong, P. Yuan, S. Murikinati, S. Gupta, and J. Grutzendler. 2015. Regional Blood Flow in
1202 the Normal and Ischemic Brain Is Controlled by Arteriolar Smooth Muscle Cell Contractility and
1203 Not by Capillary Pericytes. *Neuron*. 87:95-110.
1204 Huizinga, J.D., L. Thuneberg, M. Kluppel, J. Malysz, H.B. Mikkelsen, and A. Bernstein. 1995. W/kit
1205 gene required for interstitial cells of Cajal and for intestinal pacemaker activity. *Nature*. 373:347-
1206 349.
1207 Hwang, S.J., P.J. Blair, F.C. Britton, K.E. O'Driscoll, G. Hennig, Y.R. Bayguinov, J.R. Rock, B.D. Harfe,
1208 K.M. Sanders, and S.M. Ward. 2009. Expression of anoctamin 1/TMEM16A by interstitial cells

1209 of Cajal is fundamental for slow wave activity in gastrointestinal muscles. *J Physiol*. 587:4887-
1210 4904.
1211 Imtiaz, M.S., J. Zhao, K. Hosaka, P.Y. von der Weid, M. Crowe, and D.F. van Helden. 2007. Pacemaking
1212 through Ca2+ stores interacting as coupled oscillators via membrane depolarization. *Biophys J*.
1213 92:3843-3861.
1214 Jolly, A.J., S. Lu, K.A. Strand, A.M. Dubner, M.F. Mutryn, R.A. Nemenoff, M.W. Majesky, K.S.
1215 Moulton, and M.C.M. Weiser-Evans. 2022. Heterogeneous subpopulations of adventitial
1216 progenitor cells regulate vascular homeostasis and pathological vascular remodelling. *Cardiovasc*
1217 *Res*. 118:1452-1465.
1218 Kang, S.H., M. Fukaya, J.K. Yang, J.D. Rothstein, and D.E. Bergles. 2010. NG2+ CNS glial progenitors
1219 remain committed to the oligodendrocyte lineage in postnatal life and following
1220 neurodegeneration. *Neuron*. 68:668-681.
1221 Kenney, H.M., R.D. Bell, E.A. Masters, L. Xing, C.T. Ritchlin, and E.M. Schwarz. 2020. Lineage tracing
1222 reveals evidence of a popliteal lymphatic muscle progenitor cell that is distinct from skeletal and
1223 vascular muscle progenitors. *Sci Rep*. 10:18088.
1224 Kenney, H.M., C.L. Wu, A.E. Loiselle, L. Xing, C.T. Ritchlin, and E.M. Schwarz. 2022. Single-cell
1225 transcriptomics of popliteal lymphatic vessels and peripheral veins reveals altered lymphatic
1226 muscle and immune cell populations in the TNF-Tg arthritis model. *Arthritis Res Ther*. 24:64.
1227 Kimura, K., K. Ramirez, T.A.V. Nguyen, Y. Yamashiro, A. Sada, and H. Yanagisawa. 2021.
1228 Contribution of PDGFRalpha-positive cells in maintenance and injury responses in mouse large
1229 vessels. *Sci Rep*. 11:8683.
1230 Koval, M., S.A. Molina, and J.M. Burt. 2014. Mix and match: investigating heteromeric and heterotypic
1231 gap junction channels in model systems and native tissues. *FEBS Lett*. 588:1193-1204.
1232 Kramann, R., R.K. Schneider, D.P. DiRocco, F. Machado, S. Fleig, P.A. Bondzie, J.M. Henderson, B.L.
1233 Ebert, and B.D. Humphreys. 2015. Perivascular Gli1+ progenitors are key contributors to injury-
1234 induced organ fibrosis. *Cell Stem Cell*. 16:51-66.
1235 Kurahashi, M., Y. Nakano, L.E. Peri, J.B. Townsend, S.M. Ward, and K.M. Sanders. 2013. A novel
1236 population of subepithelial platelet-derived growth factor receptor alpha-positive cells in the
1237 mouse and human colon. *Am J Physiol Gastrointest Liver Physiol*. 304:G823-834.
1238 Kurahashi, M., H. Zheng, L. Dwyer, S.M. Ward, S.D. Koh, and K.M. Sanders. 2011. A functional role for
1239 the 'fibroblast-like cells' in gastrointestinal smooth muscles. *J Physiol*. 589:697-710.
1240 Leak, L.V., and J.F. Burke. 1968. Ultrastructural studies on the lymphatic anchoring filaments. *The*
1241 *Journal of cell biology*. 36:129-149.
1242 Lee, Y., S. Chakraborty, and M. Muthuchamy. 2020. Roles of sarcoplasmic reticulum Ca(2+) ATPase
1243 pump in the impairments of lymphatic contractile activity in a metabolic syndrome rat model. *Sci*
1244 *Rep*. 10:12320.
1245 Lendahl, U., L. Muhl, and C. Betsholtz. 2022. Identification, discrimination and heterogeneity of
1246 fibroblasts. *Nat Commun*. 13:3409.
1247 Li, S.W., C.Y. Wang, Y.J. Jou, T.C. Yang, S.H. Huang, L. Wan, Y.J. Lin, and C.W. Lin. 2016. SARS
1248 coronavirus papain-like protease induces Egr-1-dependent up-regulation of TGF-beta1 via
1249 ROS/p38 MAPK/STAT3 pathway. *Sci Rep*. 6:25754.
1250 Luo, H., X. Xia, L.B. Huang, H. An, M. Cao, G.D. Kim, H.N. Chen, W.H. Zhang, Y. Shu, X. Kong, Z.
1251 Ren, P.H. Li, Y. Liu, H. Tang, R. Sun, C. Li, B. Bai, W. Jia, Y. Liu, W. Zhang, L. Yang, Y. Peng,
1252 L. Dai, H. Hu, Y. Jiang, Y. Hu, J. Zhu, H. Jiang, Z. Li, C. Caulin, J. Park, and H. Xu. 2022a. Pan-
1253 cancer single-cell analysis reveals the heterogeneity and plasticity of cancer-associated fibroblasts
1254 in the tumor microenvironment. *Nat Commun*. 13:6619.
1255 Luo, Y., J. Wang, K. Li, M. Li, S. Xu, X. Liu, Z. Zhang, X. Xu, Y. Zhang, J. Pan, P. Liu, S. Gao, Z.
1256 Miao, and Y. Yu. 2022b. Single-cell genomics identifies distinct B1 cell developmental pathways
1257 and reveals aging-related changes in the B-cell receptor repertoire. *Cell Biosci*. 12:57.
1258 Madisen, L., T. Mao, H. Koch, J.M. Zhuo, A. Berenyi, S. Fujisawa, Y.W. Hsu, A.J. Garcia, 3rd, X. Gu, S.
1259 Zanella, J. Kidney, H. Gu, Y. Mao, B.M. Hooks, E.S. Boyden, G. Buzsaki, J.M. Ramirez, A.R.

1260 Jones, K. Svoboda, ..., and H. Zeng. 2012. A toolbox of Cre-dependent optogenetic transgenic
1261 mice for light-induced activation and silencing. *Nat Neurosci*. 15:793-802.
1262 Maeda, H., A. Yamagata, S. Nishikawa, K. Yoshinaga, S. Kobayashi, K. Nishi, and S. Nishikawa. 1992.
1263 Requirement of c-kit for development of intestinal pacemaker system. *Development*. 116:369-
1264 375.
1265 Majesky, M.W., H. Horita, A. Ostriker, S. Lu, J.N. Regan, A. Bagchi, X.R. Dong, J. Poczobutt, R.A.
1266 Nemenoff, and M.C. Weiser-Evans. 2017. Differentiated Smooth Muscle Cells Generate a
1267 Subpopulation of Resident Vascular Progenitor Cells in the Adventitia Regulated by Klf4. *Circ*
1268 *Res*. 120:296-311.
1269 Malysz, J., S.J. Gibbons, S.A. Saravanaperumal, P. Du, S.T. Eisenman, C. Cao, U. Oh, D. Saur, S. Klein,
1270 T. Ordog, and G. Farrugia. 2017. Conditional genetic deletion of Ano1 in interstitial cells of Cajal
1271 impairs Ca(2+) transients and slow waves in adult mouse small intestine. *Am J Physiol*
1272 *Gastrointest Liver Physiol*. 312:G228-G245.
1273 McCloskey, K.D., M.A. Hollywood, K.D. Thornbury, S.M. Ward, and N.G. McHale. 2002. Kit-like
1274 immunopositive cells in sheep mesenteric lymphatic vessels. *Cell Tissue Res*. 310:77-84.
1275 Mitsui, R., and H. Hashitani. 2020. Synchrony of spontaneous Ca(2+) activity in microvascular mural
1276 cells. *Journal of smooth muscle research = Nihon Heikatsukin Gakkai kikanshi*. 56:1-18.
1277 Mohanakumar, S., J. Majgaard, N. Telinius, N. Katballe, E. Pahle, V.E. Hjortdal, and D.M.B. Boedtkjer.
1278 2018. Spontaneous and alpha-adrenoceptor-induced contractility in human collecting lymphatic
1279 vessels require chloride. *Am J Physiol Heart Circ Physiol*.
1280 Muhl, L., G. Genove, S. Leptidis, J. Liu, L. He, G. Mocci, Y. Sun, S. Gustafsson, B. Buyandelger, I.V.
1281 Chivukula, A. Segerstolpe, E. Raschperger, E.M. Hansson, J.L.M. Bjorkegren, X.R. Peng, M.
1282 Vanlandewijck, U. Lendahl, and C. Betsholtz. 2020. Single-cell analysis uncovers fibroblast
1283 heterogeneity and criteria for fibroblast and mural cell identification and discrimination. *Nat*
1284 *Commun*. 11:3953.
1285 Muzumdar, M.D., B. Tasic, K. Miyamichi, L. Li, and L. Luo. 2007. A global double-fluorescent Cre
1286 reporter mouse. *Genesis*. 45:593-605.
1287 Olszewski, W.L. 2002. Contractility patterns of normal and pathologically changed human lymphatics.
1288 *Ann N Y Acad Sci*. 979:52-63; discussion 76-59.
1289 Olszewski, W.L. 2008. Contractility patterns of human leg lymphatics in various stages of obstructive
1290 lymphedema. *Ann N Y Acad Sci*. 1131:110-118.
1291 Ordog, T., S.M. Ward, and K.M. Sanders. 1999. Interstitial cells of cajal generate electrical slow waves in
1292 the murine stomach. *J Physiol*. 518:257-269.
1293 Petkova, M., M. Kraft, S. Stritt, I. Martinez-Corral, H. Ortsater, M. Vanlandewijck, B. Jakic, E. Baselga,
1294 S.D. Castillo, M. Graupera, C. Betsholtz, and T. Makinen. 2023. Immune-interacting lymphatic
1295 endothelial subtype at capillary terminals drives lymphatic malformation. *J Exp Med*. 220.
1296 Pitulescu, M.E., and R.H. Adams. 2014. Regulation of signaling interactions and receptor endocytosis in
1297 growing blood vessels. *Cell Adh Migr*. 8:366-377.
1298 Popescu, L.M., and M.S. Faussone-Pellegrini. 2010. TELOCYTES - a case of serendipity: the winding
1299 way from Interstitial Cells of Cajal (ICC), via Interstitial Cajal-Like Cells (ICLC) to
1300 TELOCYTES. *J Cell Mol Med*. 14:729-740.
1301 Sanders, K.M., S.A. Baker, B.T. Drumm, and M. Kurahashi. 2022. Ca(2+) Signaling Is the Basis for
1302 Pacemaker Activity and Neurotransduction in Interstitial Cells of the GI Tract. *Adv Exp Med Biol*.
1303 1383:229-241.
1304 Sanders, K.M., T. Ordog, S.D. Koh, S. Torihashi, and S.M. Ward. 1999. Development and plasticity of
1305 interstitial cells of Cajal. *Neurogastroenterol Motil*. 11:311-338.
1306 Sanders, K.M., S.M. Ward, and S.D. Koh. 2014. Interstitial cells: regulators of smooth muscle function.
1307 *Physiol Rev*. 94:859-907.
1308 Sanketi, B.D., M. Mantri, L. Huang, M.A. Tavallaei, S. Hu, M.F.Z. Wang, I. De Vlaminck, and N.A.
1309 Kurpios. 2024. Villus myofibroblasts are developmental and adult progenitors of mammalian gut
1310 lymphatic musculature. *Dev Cell*. 59:1159-1174 e1155.

1311 Sasmono, R.T., D. Oceandy, J.W. Pollard, W. Tong, P. Pavli, B.J. Wainwright, M.C. Ostrowski, S.R.
1312 Himes, and D.A. Hume. 2003. A macrophage colony-stimulating factor receptor-green
1313 fluorescent protein transgene is expressed throughout the mononuclear phagocyte system of the
1314 mouse. *Blood*. 101:1155-1163.
1315 Scallan, J.P., and M.J. Davis. 2013. Genetic removal of basal nitric oxide enhances contractile activity in
1316 isolated murine collecting lymphatic vessels. *J Physiol*. 591:2139-2156.
1317 Scallan, J.P., S.D. Zawieja, J.A. Castorena-Gonzalez, and M.J. Davis. 2016. Lymphatic pumping:
1318 Mechanics, mechanisms and malfunction. *J Physiol*.
1319 Sidney, L.E., M.J. Branch, S.E. Dunphy, H.S. Dua, and A. Hopkinson. 2014. Concise review: evidence
1320 for CD34 as a common marker for diverse progenitors. *Stem Cells*. 32:1380-1389.
1321 Singh, R.D., S.J. Gibbons, S.A. Saravanaperumal, P. Du, G.W. Hennig, S.T. Eisenman, A. Mazzone, Y.
1322 Hayashi, C. Cao, G.J. Stoltz, T. Ordog, J.R. Rock, B.D. Harfe, J.H. Szurszewski, and G. Farrugia.
1323 2014. Ano1, a Ca2+-activated Cl- channel, coordinates contractility in mouse intestine by Ca2+
1324 transient coordination between interstitial cells of Cajal. *J Physiol*. 592:4051-4068.
1325 Song, K., Y. Qing, Q. Guo, E.K. Peden, C. Chen, W.E. Mitch, L. Truong, and J. Cheng. 2020. PDGFRA
1326 in vascular adventitial MSCs promotes neointima formation in arteriovenous fistula in chronic
1327 kidney disease. *JCI Insight*. 5.
1328 Spandidos, A., X. Wang, H. Wang, S. Dragnev, T. Thurber, and B. Seed. 2008. A comprehensive
1329 collection of experimentally validated primers for Polymerase Chain Reaction quantitation of
1330 murine transcript abundance. *BMC Genomics*. 9:633.
1331 Spandidos, A., X. Wang, H. Wang, and B. Seed. 2010. PrimerBank: a resource of human and mouse PCR
1332 primer pairs for gene expression detection and quantification. *Nucleic Acids Res*. 38:D792-799.
1333 Stolarz, A.J., M. Sarimollaoglu, J.C. Marecki, T.W. Fletcher, E.I. Galanzha, S.W. Rhee, V.P. Zharov,
1334 V.S. Klimberg, and N.J. Rusch. 2019. Doxorubicin Activates Ryanodine Receptors in Rat
1335 Lymphatic Muscle Cells to Attenuate Rhythmic Contractions and Lymph Flow. *J Pharmacol Exp*
1336 *Ther*. 371:278-289.
1337 Thillaiappan, N.B., H.A. Smith, P. Atakpa-Adaji, and C.W. Taylor. 2021. KRAP tethers IP(3) receptors
1338 to actin and licenses them to evoke cytosolic Ca(2+) signals. *Nat Commun*. 12:4514.
1339 To, K.H.T., P. Gui, M. Li, S.D. Zawieja, J.A. Castorena-Gonzalez, and M.J. Davis. 2020. T-type, but not
1340 L-type, voltage-gated calcium channels are dispensable for lymphatic pacemaking and
1341 spontaneous contractions. *Sci Rep*. 10:70.
1342 Toland, H.M., K.D. McCloskey, K.D. Thornbury, N.G. McHale, and M.A. Hollywood. 2000. Ca(2+)-
1343 activated Cl(-) current in sheep lymphatic smooth muscle. *Am J Physiol Cell Physiol*. 279:C1327-
1344 1335.
1345 Torihashi, S., S.M. Ward, S. Nishikawa, K. Nishi, S. Kobayashi, and K.M. Sanders. 1995. c-kit-
1346 dependent development of interstitial cells and electrical activity in the murine gastrointestinal
1347 tract. *Cell Tissue Res*. 280:97-111.
1348 Truett, G.E., P. Heeger, R.L. Mynatt, A.A. Truett, J.A. Walker, and M.L. Warman. 2000. Preparation of
1349 PCR-quality mouse genomic DNA with hot sodium hydroxide and tris (HotSHOT).
1350 *Biotechniques*. 29:52, 54.
1351 Van Helden, D.A., P.Y. Von Der Weid, and M. Crowe. 1996. Intracellular Ca Release: A basis for
1352 electrical pacemaking in lymphatic smooth muscle. *In* Smooth muscle excitation. T.B. Ed. Bolton
1353 and T. Tomita, editors. London: Academic Press. 355–373.
1354 Van Helden, D.F. 1991. Spontaneous and noradrenaline-induced transient depolarizations in the smooth
1355 muscle of guinea-pig mesenteric vein. *J Physiol*. 437:511-541.
1356 Van Helden, D.F. 1993. Pacemaker potentials in lymphatic smooth muscle of the guinea-pig mesentery. *J*
1357 *Physiol*. 471:465-479.
1358 van Helden, D.F., K. Hosaka, and M.S. Imtiaz. 2006. Rhythmicity in the microcirculation. *Clin*
1359 *Hemorheol Microcirc*. 34:59-66.
1360 van Helden, D.F., and M.S. Imtiaz. 2019. Venous Vasomotion. *Adv Exp Med Biol*. 1124:313-328.

1361 Van Helden, D.F., and J. Zhao. 2000. Lymphatic vasomotion. *Clin Exp Pharmacol Physiol*. 27:1014-
1362 1018.
1363 Van, S., S. Pal, B.R. Garner, K. Steed, V. Sridharan, S. Mu, N.J. Rusch, and A.J. Stolarz. 2021.
1364 Dantrolene Prevents the Lymphostasis Caused by Doxorubicin in the Rat Mesenteric Circulation.
1365 *Front Pharmacol*. 12:727526.
1366 Vannucchi, M.G., C. Traini, M. Manetti, L. Ibba-Manneschi, and M.S. Faussone-Pellegrini. 2013.
1367 Telocytes express PDGFRalpha in the human gastrointestinal tract. *J Cell Mol Med*. 17:1099-
1368 1108.
1369 von der Weid, P.Y., S. Lee, M.S. Imtiaz, D.C. Zawieja, and M.J. Davis. 2014. Electrophysiological
1370 properties of rat mesenteric lymphatic vessels and their regulation by stretch. *Lymphat Res Biol*.
1371 12:66-75.
1372 von der Weid, P.Y., M. Rahman, M.S. Imtiaz, and D.F. van Helden. 2008. Spontaneous transient
1373 depolarizations in lymphatic vessels of the guinea pig mesentery: pharmacology and implication
1374 for spontaneous contractility. *Am J Physiol Heart Circ Physiol*. 295:H1989-2000.
1375 Wang, X., and B. Seed. 2003. A PCR primer bank for quantitative gene expression analysis. *Nucleic*
1376 *Acids Res*. 31:e154.
1377 Wang, Y., Y. Jin, M.A. Mae, Y. Zhang, H. Ortsater, C. Betsholtz, T. Makinen, and L. Jakobsson. 2017.
1378 Smooth muscle cell recruitment to lymphatic vessels requires PDGFB and impacts vessel size but
1379 not identity. *Development*. 144:3590-3601.
1380 Ward, S.M., A.J. Burns, S. Torihashi, and K.M. Sanders. 1994. Mutation of the proto-oncogene c-kit
1381 blocks development of interstitial cells and electrical rhythmicity in murine intestine. *J Physiol*.
1382 480 (Pt 1):91-97.
1383 Warthi, G., J.L. Faulkner, J. Doja, A.R. Ghanam, P. Gao, A.C. Yang, O.J. Slivano, C.T. Barris, T.C.
1384 Kress, S.D. Zawieja, S.H. Griffin, X. Xie, A. Ashworth, C.K. Christie, W.B. Bryant, A. Kumar,
1385 M.J. Davis, X. Long, L. Gan, E.J. Belin de Chantemele, Q. Lyu, and J.M. Miano. 2022.
1386 Generation and Comparative Analysis of an Itga8-CreER (T2) Mouse with Preferential Activity
1387 in Vascular Smooth Muscle Cells. *Nat Cardiovasc Res*. 1:1084-1100.
1388 Wirth, A., Z. Benyo, M. Lukasova, B. Leutgeb, N. Wettschureck, S. Gorbey, P. Orsy, B. Horvath, C.
1389 Maser-Gluth, E. Greiner, B. Lemmer, G. Schutz, J.S. Gutkind, and S. Offermanns. 2008. G12-
1390 G13-LARG-mediated signaling in vascular smooth muscle is required for salt-induced
1391 hypertension. *Nat Med*. 14:64-68.
1392 Xiao, J., F. Wang, Z. Liu, and C. Yang. 2013. Telocytes in liver: electron microscopic and
1393 immunofluorescent evidence. *J Cell Mol Med*. 17:1537-1542.
1394 Yang, L., Y. Zhu, D. Tian, S. Wang, J. Guo, G. Sun, H. Jin, C. Zhang, W. Shi, M.E. Gershwin, Z. Zhang,
1395 Y. Zhao, and D. Zhang. 2021. Transcriptome landscape of double negative T cells by single-cell
1396 RNA sequencing. *J Autoimmun*. 121:102653.
1397 Yoon, J.H., H. Jin, H.J. Kim, S.P. Hong, M.J. Yang, J.H. Ahn, Y.C. Kim, J. Seo, Y. Lee, D.M.
1398 McDonald, M.J. Davis, and G.Y. Koh. 2024. Nasopharyngeal lymphatic plexus is a hub for
1399 cerebrospinal fluid drainage. *Nature*. 625:768-777.
1400 Young, M.D., and S. Behjati. 2020. SoupX removes ambient RNA contamination from droplet-based
1401 single-cell RNA sequencing data. *Gigascience*. 9.
1402 Zawieja, D.C., K.L. Davis, R. Schuster, W.M. Hinds, and H.J. Granger. 1993. Distribution, propagation,
1403 and coordination of contractile activity in lymphatics. *Am J Physiol*. 264:H1283-1291.
1404 Zawieja, S.D., J.A. Castorena, P. Gui, M. Li, S.A. Bulley, J.H. Jaggar, J.R. Rock, and M.J. Davis. 2019.
1405 Ano1 mediates pressure-sensitive contraction frequency changes in mouse lymphatic collecting
1406 vessels. *J Gen Physiol*. 151:532-554.
1407 Zawieja, S.D., J.A. Castorena-Gonzalez, J. Scallan, and M.J. Davis. 2018a. Differences in L-type calcium
1408 channel activity partially underlie the regional dichotomy in pumping behavior by murine
1409 peripheral and visceral lymphatic vessels. *Am J Physiol Heart Circ Physiol*.

1410 Zawieja, S.D., J.A. Castorena-Gonzalez, K.H.T. To, P. Gui, T.L. Domeier, and M.J. Davis. 2018b.
1411 Electrical Pacemaking in Lymphatic Vessels. *In* Signal Transduction in Smooth Muscle. M.
1412 Trebak and S. Earley, editors. CRC Press- Taylor & Francis Group. 324-359.
1413 Zawieja, S.D., G.A. Pea, S.E. Broyhill, A. Patro, K.H. Bromert, M. Li, C.E. Norton, J.A. Castorena-
1414 Gonzalez, E.J. Hancock, C.D. Bertram, and M.J. Davis. 2023. IP3R1 underlies diastolic ANO1
1415 activation and pressure-dependent chronotropy in lymphatic collecting vessels. *J Gen Physiol*.
1416 155.
1417 Zawieja, S.D., W. Wang, S. Chakraborty, D.C. Zawieja, and M. Muthuchamy. 2016. Macrophage
1418 alterations within the mesenteric lymphatic tissue are associated with impairment of lymphatic
1419 pump in metabolic syndrome. *Microcirculation*. 23:558-570.
1420 Zhou, Q., L. Wei, C. Zhong, S. Fu, Y. Bei, R.I. Huica, F. Wang, and J. Xiao. 2015. Cardiac telocytes are
1421 double positive for CD34/PDGFR-alpha. *J Cell Mol Med*. 19:2036-2042.
1422 Zhu, M.H., T.W. Kim, S. Ro, W. Yan, S.M. Ward, S.D. Koh, and K.M. Sanders. 2009. A Ca(2+)-
1423 activated Cl(-) conductance in interstitial cells of Cajal linked to slow wave currents and
1424 pacemaker activity. *J Physiol*. 587:4905-4918.
1425 Zhu, X., D.E. Bergles, and A. Nishiyama. 2008. NG2 cells generate both oligodendrocytes and gray
1426 matter astrocytes. *Development*. 135:145-157.
1427
1428

Table 1 Primer list for RT-PCR						
Gene	**Strand**	**Accession #**	**Sequence (5'-3')**	**Size**	**Exon**	**Source**
Prox1	s	NM_008937	GTA AGA CAT CAC CGC GTG C	218	1	NIH Primer Tool
	as		TCA TGG TCA GGC ATC ACT GG		2	
CD11b (Itgam)	s	NM_008401	ATG GAC GCT GAT GGC AAT ACC	203	13	MGH Primer Bank ID 668048a1
	as		TCC CCA TTC ACG TCT CCC A		14	
Pdgfrα	s	NM_011058	AGA GTT ACA CGT TTG AGC TGT C	252	8	MGH Primer Bank 26349287a1
	as		GTC CCT CCA CGG TAC TCC T		10	
						-
Myh11	s	NM_013607	AAG CTG CGG CTA GAG GTC A	238	33	MGH Primer Bank ID 7305295a1
	as		CCC TCC CTT TGA TGG CTG AG		34	
CD117 (cKit)	s	NM_021099	CGC CTG CCG AAA TGT ATG ACG	162	21	(Drumm et al., 2018)
	as		GGT TCT CTG GGT TGG GGT TGC		23	
Pdgfrβ	s	NM_008809	AGC TAC ATG GCC CCT TAT GA	367	16	(Basciani et al., 2004)
	as		GGA TCC CAA AAG ACC AGA CA		19	
CD144 (VE-cadherin)	s	NM_009868	CTT CCT TAC TGC CCT CAT TGT	313	3	IDT Primer Quest
	as		CTG TTT CTC TCG GTC CAA GTT		5	
Nos3 (eNOS)	s	NM_008713	ctg cca cct gat cct aac ttg	143	22	IDT Real time primer tool
	as		cag cca aac acc aaa gtc atg		23	
Acta2 (Smooth Muscle Actin)	s	NM_007392	GAG CTA CGA ACT GCC TGA C	129	7	IDT TaqMan Mm.PT.58.16320644
	as		CTG TTA TAG GTG GTT TCG TGG A		8	

CaV 1.2 exon1b	s	NM_001159533	ATG GTC AAT GAA AAC ACG AGG ATG		1	(Cheng et al., 2007)
	as		GGA ACT GAC GGT AGA GAT GGT TGC	234	2	
CD34	as	NM_001111059	GGT ACA GGA GAA TGC AGG TC	119	2	IDT Mm.PT.58.8626728
	s	NM_133654	CGT GGT AGC AGA AGT CAA GT		1	
Cspg4 (Ng2)	as	NM_139001	CTT CAC GAT CAC CAT CCT TCC	132	5	IDT Mm.PT.58.29461721
	s		CCC GAA TCA TTG TCT GTT CCC		6	
-	-	-	-	-	-	
Vimentin	s	NM_011701	CTG TAC GAG GAG GAG ATG CG	249	1	(Li et al., 2016)
	as		AAT TTC TTC CTG CAA GGA TT		3	
Desmin	s	NM_010043	GTG GAT GCA GCC ACT CTA GC	218	3	MGH Primer Bank ID 33563250a1
	as		TTA GCC GCG ATG GTC TCA TAC		4	
CD146 (Mcam)	s	NM_023061	CCC AAA CTG GTG TGC GTC TT	220	1	MGH Primer Bank 10566955a1
	as		GGA AAA TCA GTA TCT GCC TCT CC		3	
KLF4	s	NM_010637	ATT AAT GAG GCA GCC ACC TG	400	1	(Majesky et al., 2017)
	as		GGA AGA CGA GGA TGA AGC TG		3	
Ly6a (Sca1)	s	NM_001271416	CTC TGA GGA TGG ACA CTT CT	400	2	(Majesky et al., 2017)
	as		GGT CTG CAG GAG GAC TGA GC		4	
Gli1	s	NM_01029	ATC ACC TGT TGG GGA TGC TGG AT	316	8	(Kramann et al., 2015)
	as		CGT GAA TAG GAC TTC CGA CAG		10	
CD29 (Itgb1)	s	NM_010578	TCG ATC CTG TGA CCC ATT GC	170	14	NIH Primer Tool

	as		AAC AAT TCC AGC AAC CAC GC		15	
CD105 (Endoglin)	s	NM_007932	TGA GCG TGT CTC CAT TGA CC	416	11	NIH Primer Tool
	as		GGG GCC ACG TGT GTG AGA A		15	
CD44	as	NM_009851	CAC CAT TTC CTG AGA CTT GCT	148	19	IDT Mm.PT.58.12084136
	s		TCT GAT TCT TGC CGT CTG C		18	
CD31 (Pecam1)	s	NM_008816	CTG CCA GTC CGA AAA TGG AAC	218	7	MGH Primer Bank ID 6679273a1
	as		CTT CAT CCA CTG GGG CTA TC		8	
GJC1 (Connexin 45)	s	NM_008122	GGT AAC AGG AGT TCT GGT GAA	140	2	IDT Mm.PT.58.8383900
	as		TCG AAA GAC AAT CAG CAC AGT		3	
Anoctamin 1 (TMEM16A)	s	NM_178642	ggc att tgt cat tgt ctt cca g	141	25	IDT Real time primer tool
	as		tcc tca cgc ata aac agc tc		26	
CD45 (Ptprc)	s	NM_001111316	ATG CAT CCA TCC TCG TCC AC	225	29	NIH Primer Tool
	as		TGA CTT GTC CAT TCT GGG CG		31	
MGH Harvard Primer Bank (Wang and Seed, 2003; Spandidos et al., 2008; Spandidos et al., 2010)						

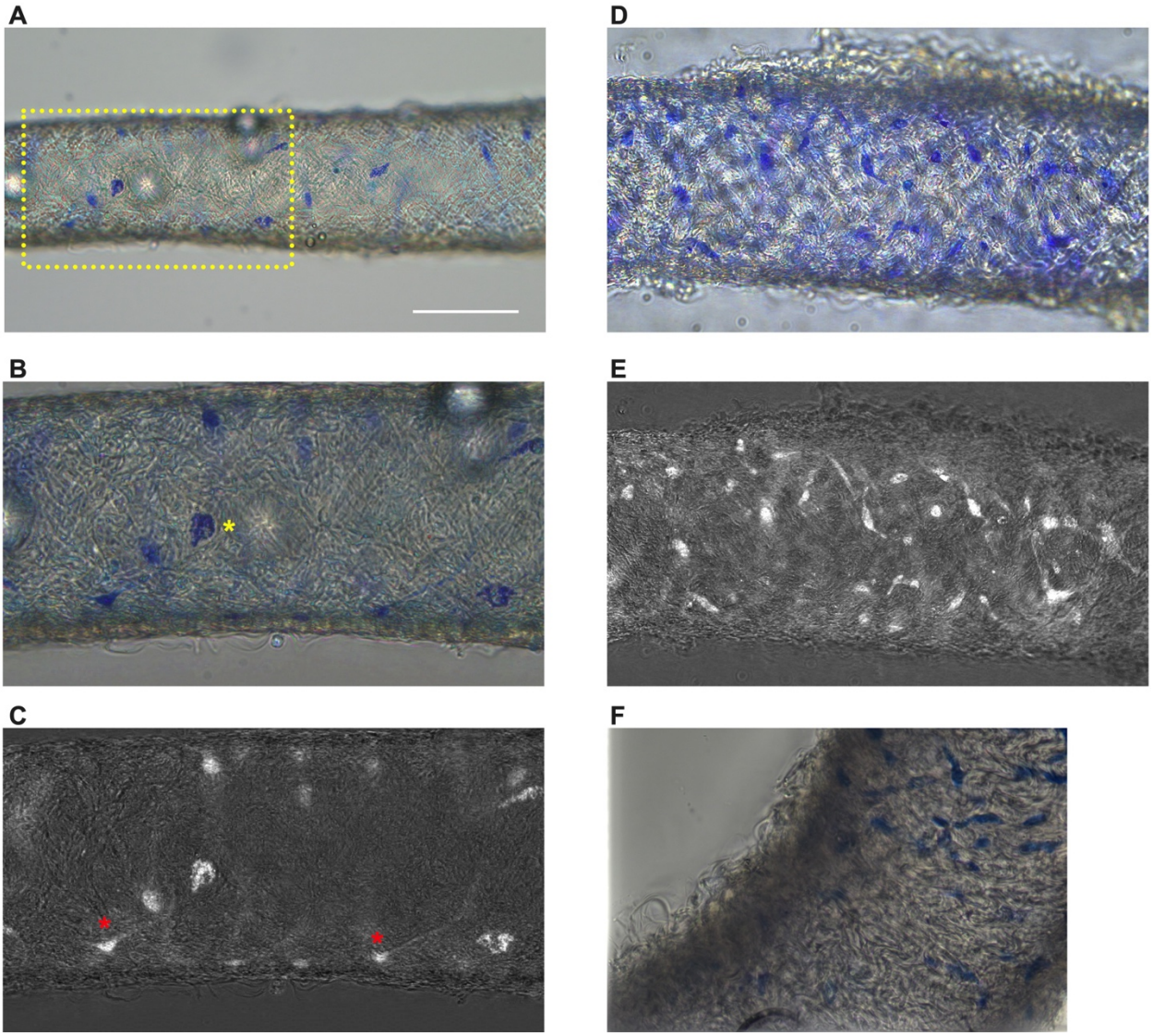

Figure 1 Methylene blue staining of isolated mouse IALVs
Representative image of an isolated and cleaned IALV after methylene blue staining which revealed cells of various morphology. (B) is the zoomed in image of the yellow dotted box in A which contained large ovoid cells with granular staining (B, yellow asterisks). Fine cellular extensions (red asterisks) stained by methylene blue in some cells were visualized with color channel separation and division (C). (D, E) Similar as B and C, but in a separate vessel which stained with a higher density of methylene blue stained cells some of which had limited cellular processes. F) Focal reconstruction from imaging a methylene blue stained IALV using an upright microscope and immersion objective.

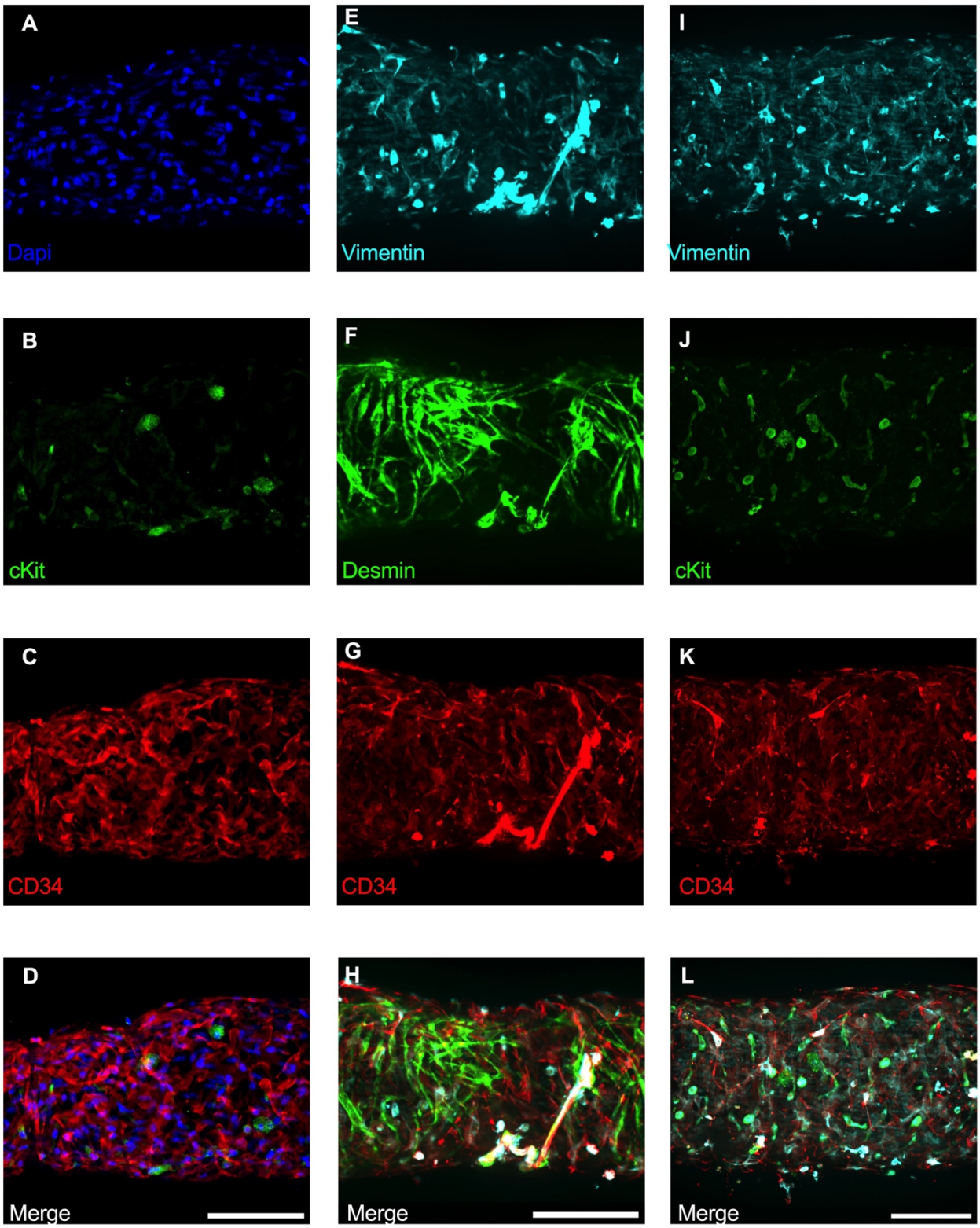

Figure 2 Staining Mouse IALVs for ICLC Markers

Representative immunofluorescent max projections of half vessel confocal image stacks imaged from mouse IALVs stained for ICLC markers. DAPI (A), cKit (B), and CD34 (C) and their merged image (D). Representative max projections of the intermediate filament vimentin (E), the intermediate filament desmin (F), CD34 (G) and their merged image (H). Representative max projection of vimentin (I), cKit (J), CD34 (K) and their merged image (L). Scale bar = 100 μm for all images.

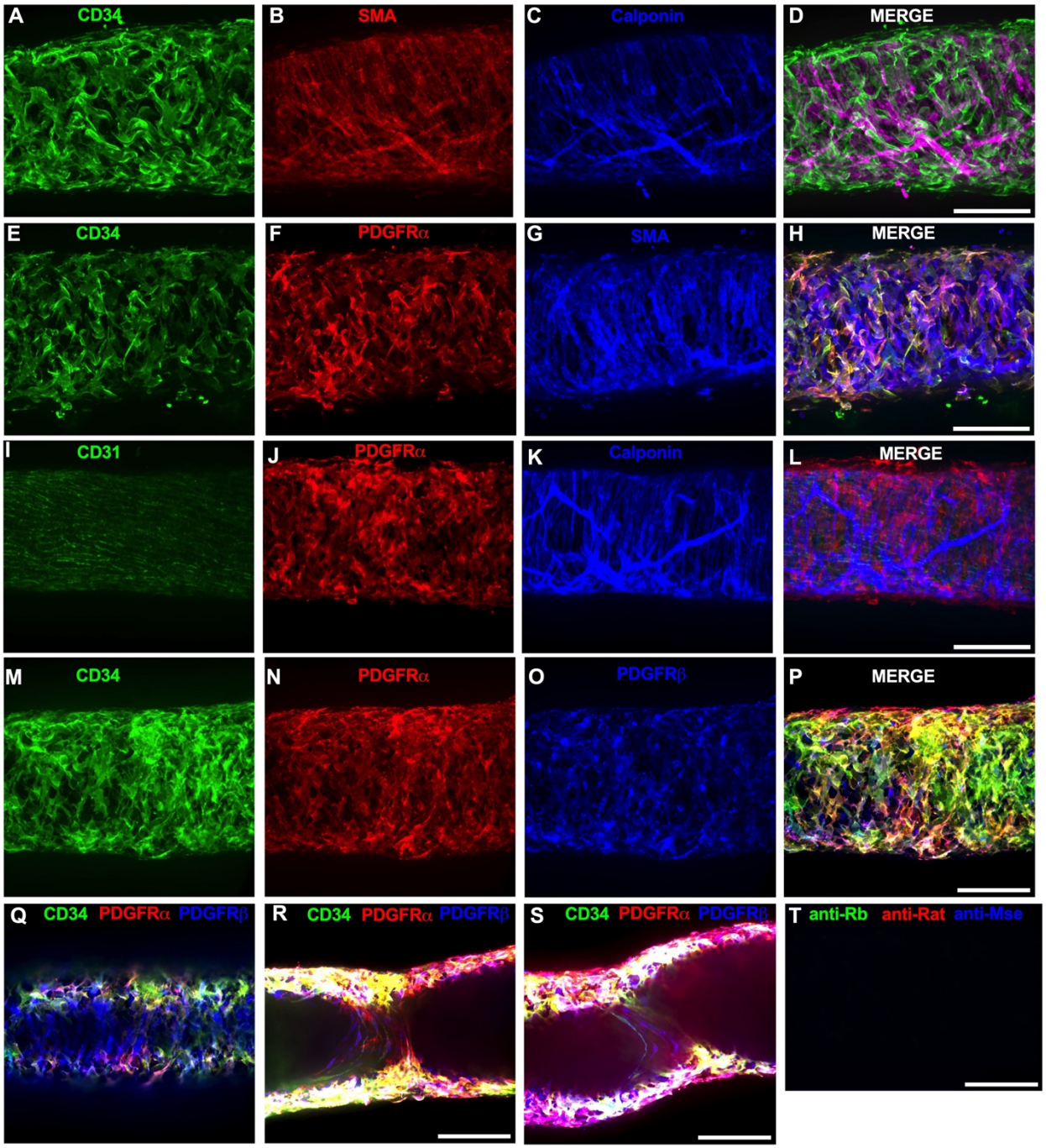

Figure 3 Immunofluorescence Labeling of Mouse IALVs with Markers for ICLC, LMC, LEC, and Immune Cell Populations

We stained isolated mouse IALVs with cellular markers used to differentiate various cell types observed in cLVs. Half vessel image stacks were taken with confocal microscopy and the resulting representative max projections are shown. (A) CD34 stained cells and LMC staining with SMA (B) and calponin (C) and the corresponding merged (D) image. There was significant overlap in (E) CD34 staining along with the fibroblast marker PDGFRα compared to LMC staining with SMA (G) and the merged (H) image. The endothelial marker CD31 (I) to delineate LECs with PDGFRα staining (J), and the LMC marker calponin (K) with the merged image (L) revealed 3 separate populations of cells. PDGFRβ (O) stained many cells that were CD34 (M) and PDGFRα (N) positive, as seen in the merge imaged (P), in addition to PDGFRβ

signal detected in the LMC layer (Q). Max projections of only the luminal frames of a z-stack at lymphatic valve locations revealed PDGFRβ, CD34, and PDGFRα labeling in bipolar shaped cells with long extensions that traveled throughout the valve leaflets (V, W). d Control IALV (Y) stained only with secondary antibody. Scale bar = 100 µm for all images.

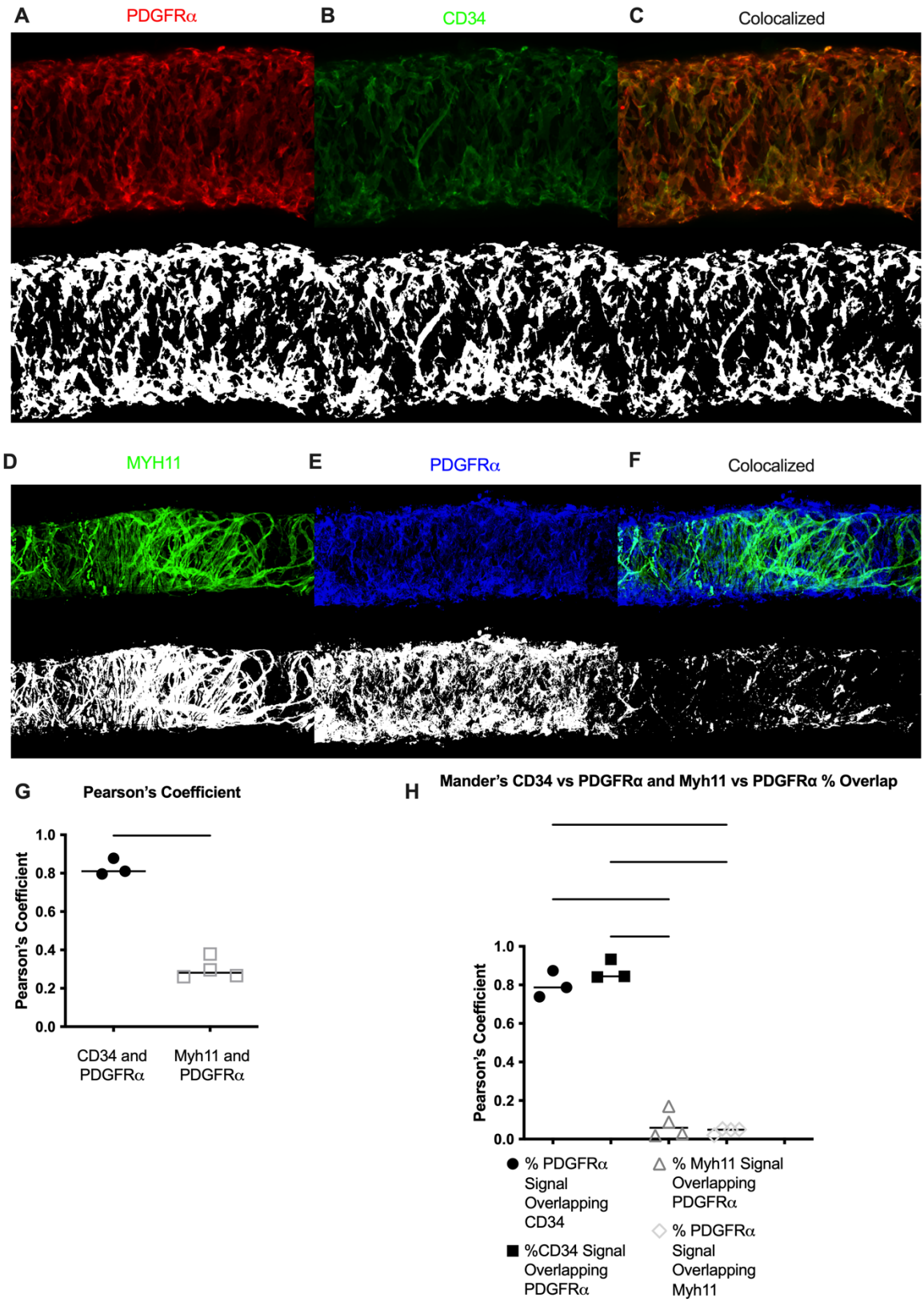

SuppFigure 1 Colocalization of CD34 and PDGFRα

Representative max projections and their corresponding threshold adjusted image for colocalization analysis for PDGFRα (A), CD34 (B), and their colocalized signal (C) and for comparison we tested Myh11 (D) and PDGFRα (E) colocalization (F) using the FIJI BIOP-JACoP colocalization plugin on the z-stacks acquired by confocal microscopy. Pearson's coefficient (G) and Mander's coefficients (H) were calculated from n=3 separate stained IALVS, each from a separate mouse for CD34 and PDGFRα and n=4 for Myh11 and PDGFRα. Magnification for A-C 40X and 25x for D-F. Significant differences in colocalization below 0.05 are signified by the overhead lines.

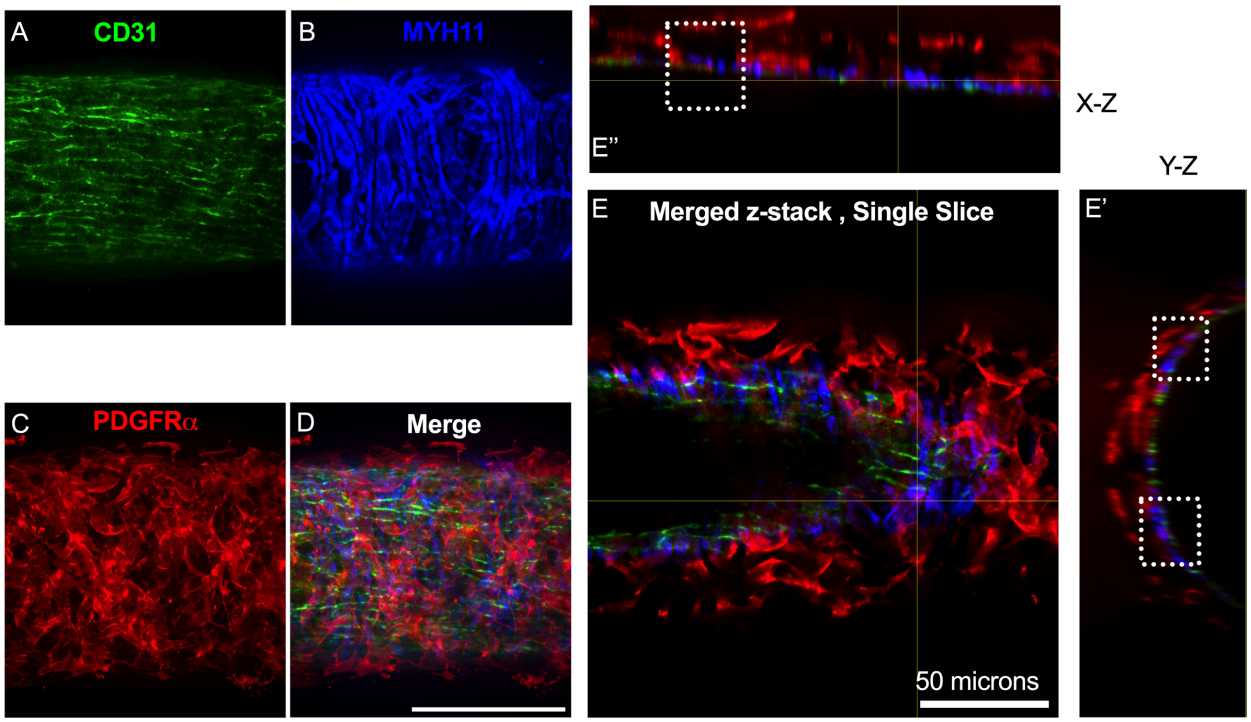

SuppFigure 2 PDGFRα^{+} Cells Reside Primarily in the Mouse Lymphatic Collecting Vessel Adventitia and Some in the Subendothelial Space

Max projection of confocal imaging of an IALV stained for LECs with CD31 (A), LMCs with MYH11(B), and for PDGFRα (C) with the corresponding merge file (D). Orthogonal views of the z-stack with (E) showing a single slice in the z stack and E' and E" the orthogonal views. White dotted boxes outline locations where PDGFRα signal is observed between LMC and LEC layers. Scale bar is 100 µm in (D) and 50 µm in (E).

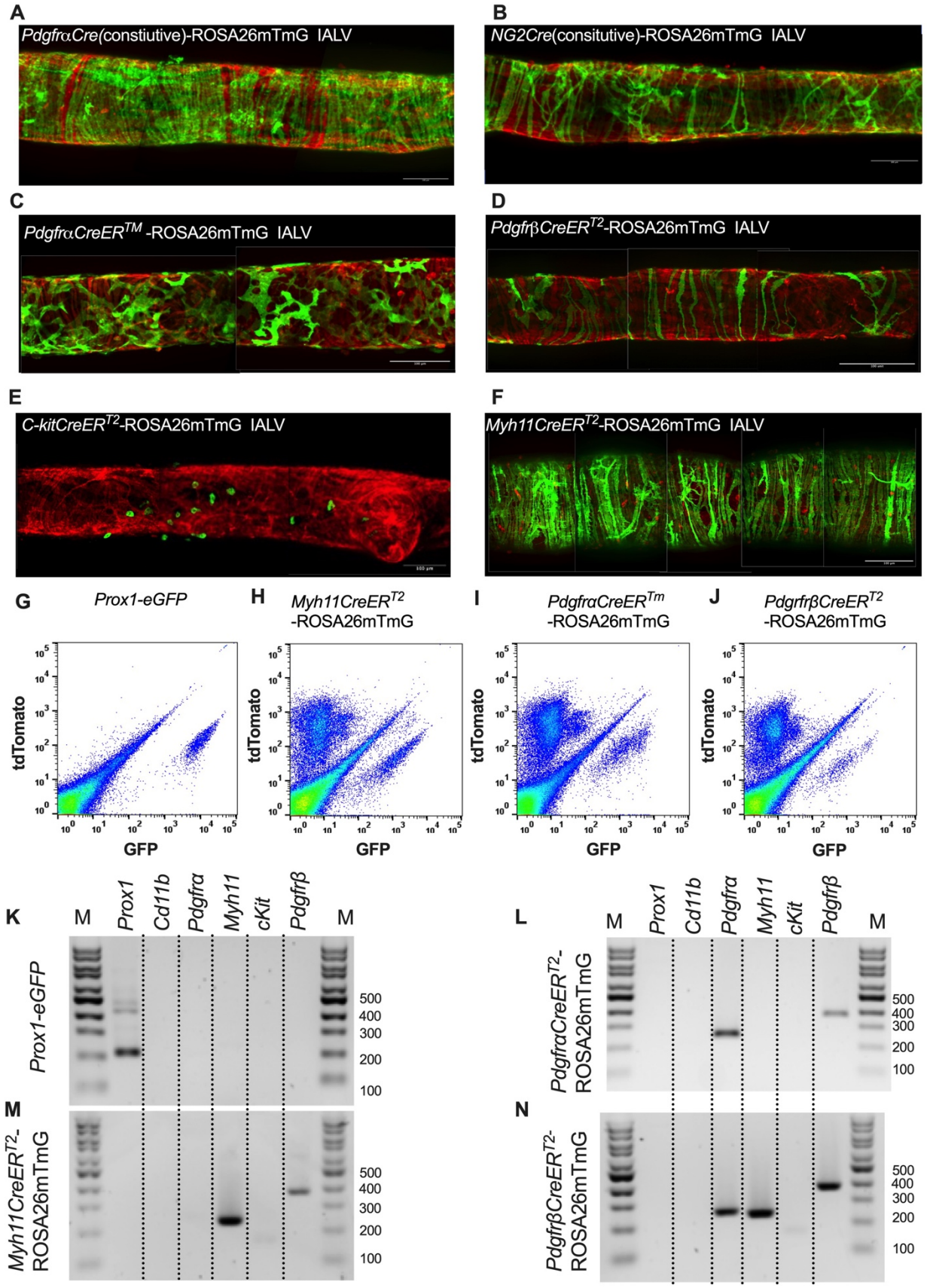
A
PdgfrαCre(constiutive)-ROSA26mTmG IALV
B
NG2Cre(consitutive)-ROSA26mTmG IALV
C
PdgfrαCreERTM -ROSA26mTmG IALV
D
PdgfrβCreERT2-ROSA26mTmG IALV
E
C-kitCreERT2-ROSA26mTmG IALV
F
Myh11CreERT2-ROSA26mTmG IALV
G
Prox1-eGFP
H
Myh11CreERT2 -ROSA26mTmG
I
PdgfrαCreERTm -ROSA26mTmG
J
PdgrfrβCreERT2 -ROSA26mTmG
tdTomato
GFP
K
M
Prox1
Cd11b
Pdgfrα
Myh11
cKit
Pdgfrβ
M
Prox1-eGFP
500
400
300
200
100
L
PdgfrαCreERT2-ROSA26mTmG
M
Myh11CreERT2-ROSA26mTmG
N
PdgfrβCreERT2-ROSA26mTmG

Figure 4 iCre-ROSA26mTmG Labelling and Fidelity to Target Putative Pacemaker Cell Populations
Stitched montages of serial max projections of GFP and tdTomato signal from live IALVs isolated from *PdgfrαCre*-ROSA26mTmG (A), *Ng2Cre*-ROSA26mTmG (B), *PdgfrαCreER*^{TM}-ROSA26mTmG (C), *PdgfrβCreER*^{T2}-ROSA26mTmG (D), *cKitCreER*^{T2}-ROSA26mTmG (E), and *Myh11CreER*^{T2}-ROSA26mTmG (F). IALVs were digested into single cells and GFP^{+} cells were purified via FACS from *Prox1-eGFP* (G), *Myh11CreER*^{T2}-ROSA26mTmG (H), *PdgfrαCreER*^{TM}-ROSA26mTmG (I), and *PdgfrβCreER*^{T2}-ROSA26mTmG (J) mice. Representative gels demonstrating RT-PCR products corresponding to the respective genes used in the promoter of each specific transgene employed to drive either eGFP or Cre mediated recombination of ROSA26mTmG from each GFP^{+} sorted population (K-N) to assess fidelity. Images are representative of IALVs from at least 3 separate mice. FACs and RT-PCR was repeated at least 3 times for each mouse.

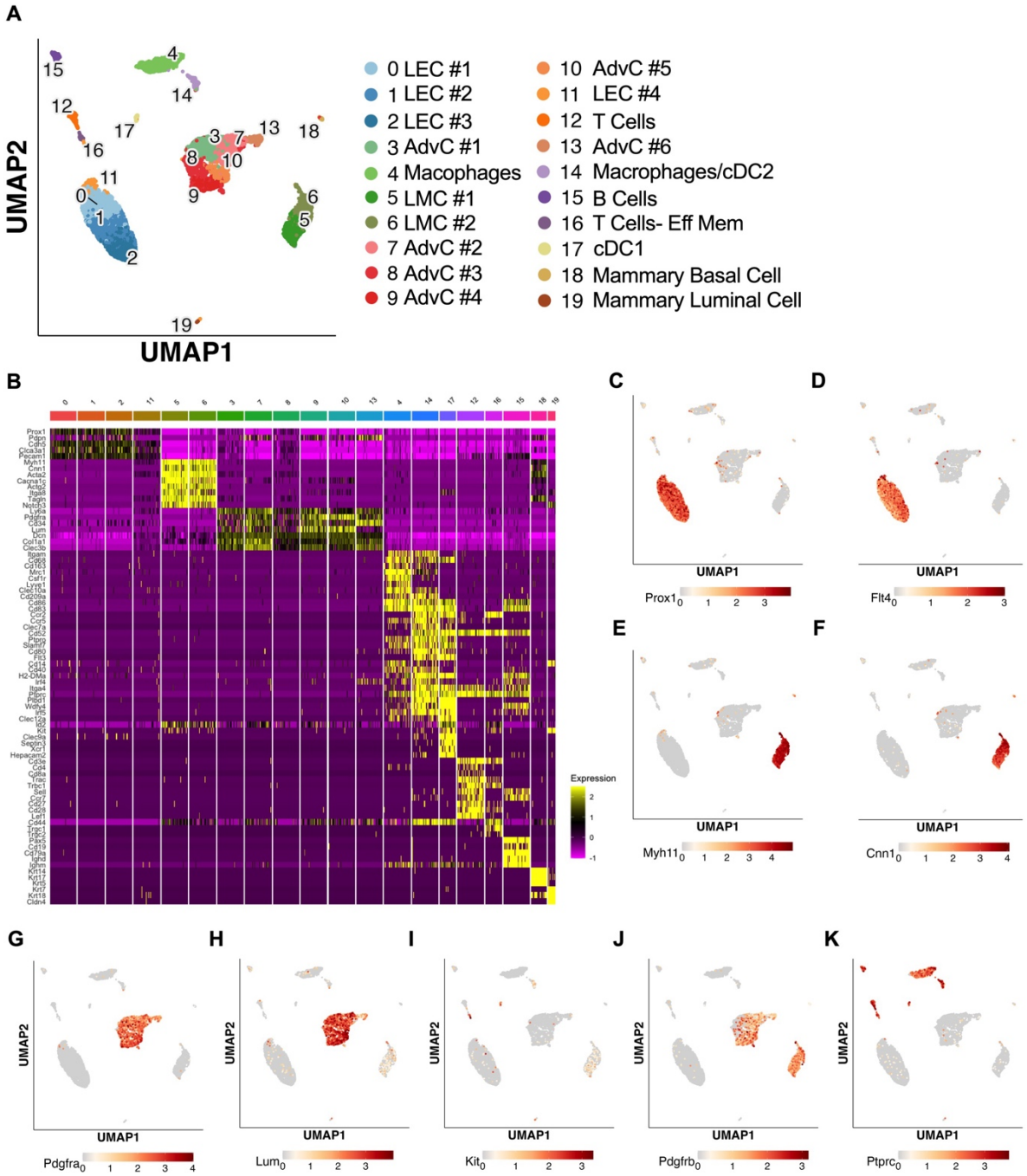

Figure 5 scRNAseq analysis of mouse IALVs from ROSA26mTmG mice.
IALVs were cleaned and isolated from 8 ROSA26mTmG mice and digested into a single cell suspension for scRNAseq analysis with the 10X platform. A) UMAP of the various cell populations that compromise the mouse IALV though some mammary epithelia contamination was present (populations 18,19). B) Heat map of commonly used genes for cell identification for each of the cell clusters. Dot plots to assess cell cluster expression of the genes shown in Figure 4 using a dot plot for the LEC markers *Prox1* (C) and *Flt4* (D, VEGFR3), LMC markers *Myh11* (E) and caponin1 (F, *Cnn1*), fibroblast markers *Pdgfrα* (G) and *Lum* (H, *Lumican*), ICC marker *Kit* (I), the pericyte and smooth muscle precursor marker (*Pdgfrβ*), and the hematopoietic marker *Ptprc* (K, CD45).

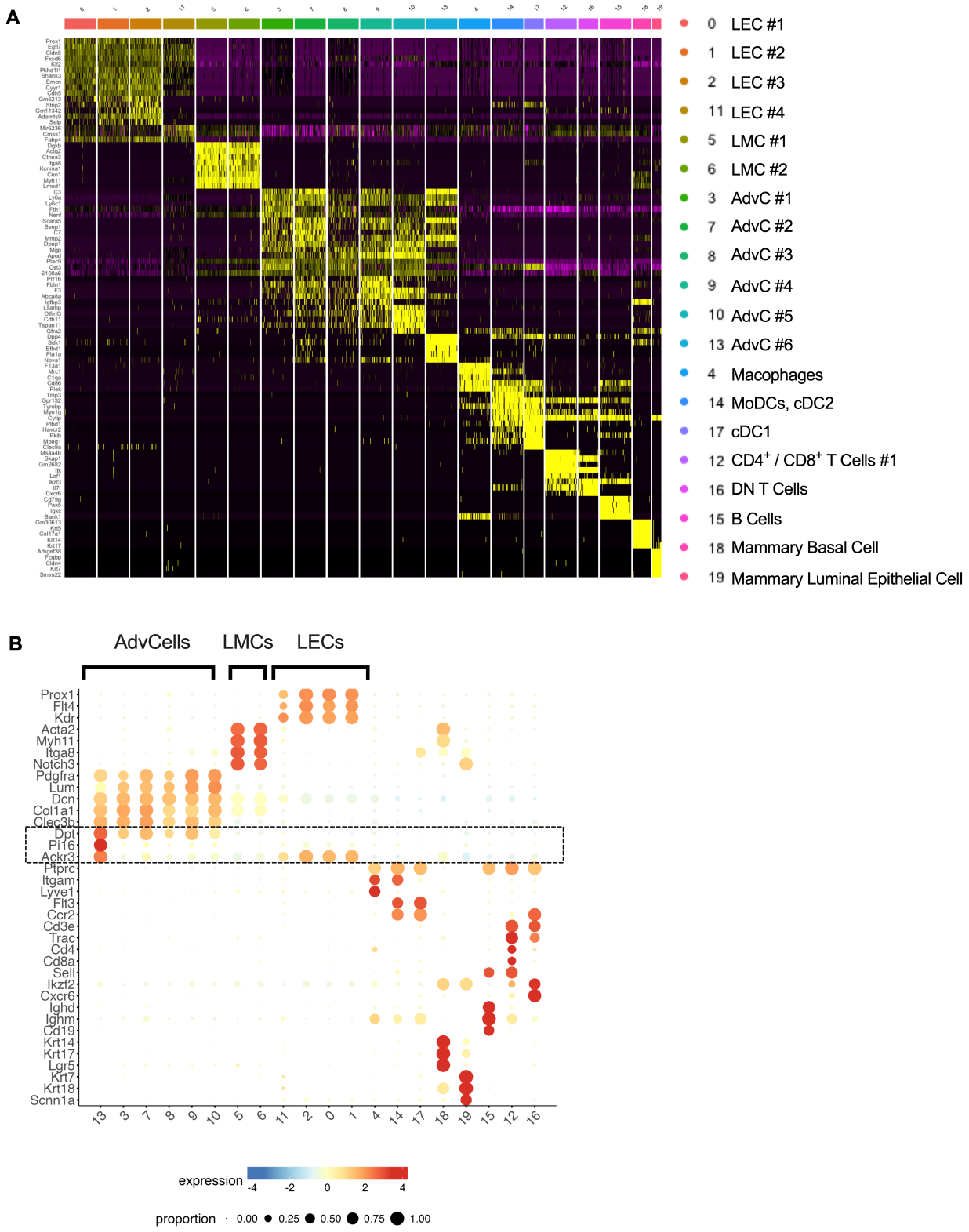

SuppFigure 3. scRNASeq Analysis of the mouse IALV cell populations.
Heatmap of top 4-5 differentially expressed genes, based on p value, for each major cell cluster identified. LECs (Clusters 0,1,2, 11), LMCs (Cluster 5,6), and IALV adventitial cells (AdvC, 3,7,8,9,10,13) were

comprised of multiple clusters. B) Bubble plot of common identification genes reveal that the previous reported LMC transcriptome markers Dpt, Pi16, and Ackr3 are specific for a sub population of the Adv and not LMCs.

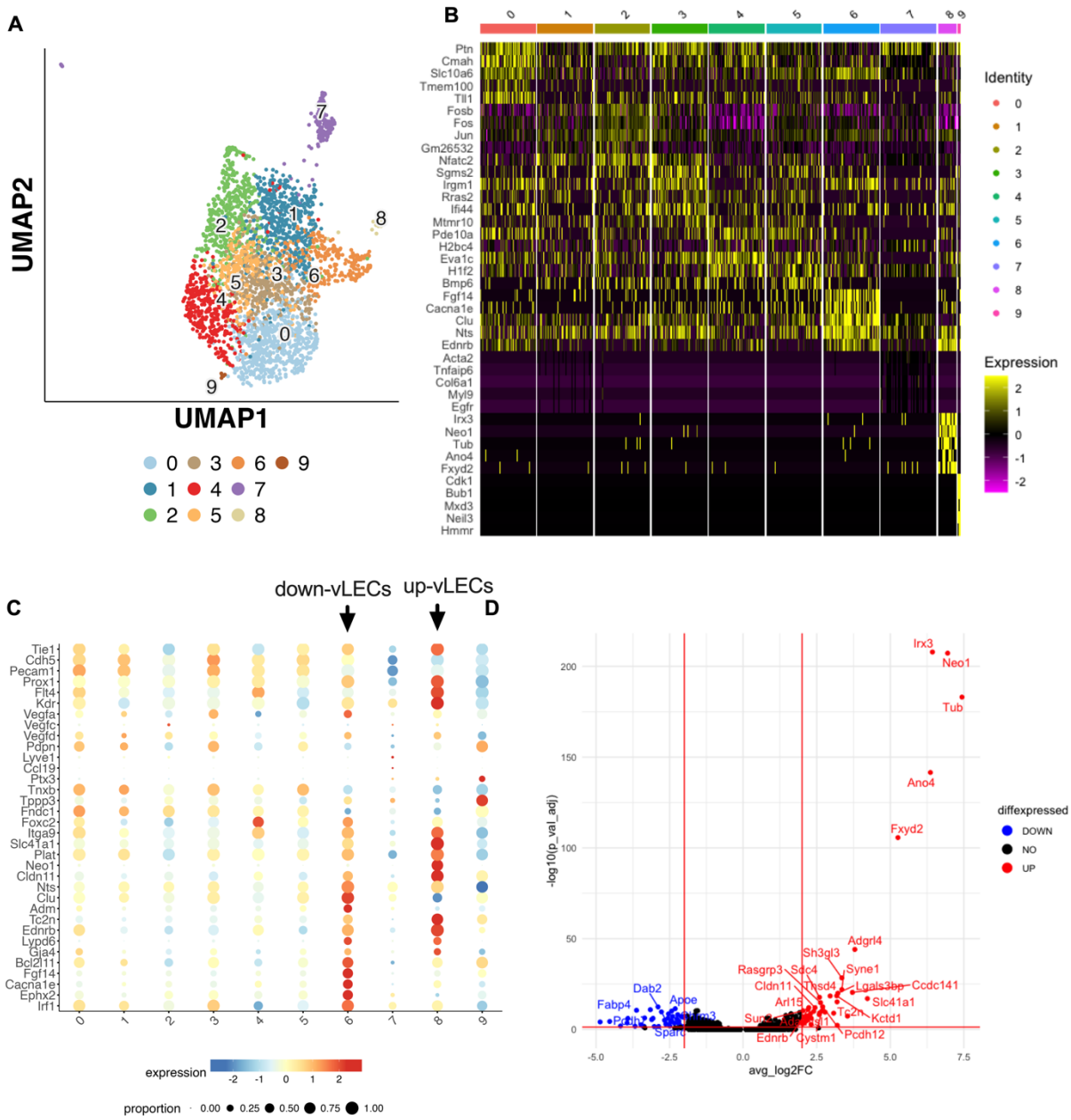

SuppFigure 4. Subclusters of IALV LECs revealed by scRNAseq.
The LECs were further sub-clustered to reveal 10 putative LEC subclusters (0-9) as shown in the UMAP (A) and the top differentially expressed genes amongst those sub-clusters are provided in the adjacent heatmap (B). (C) Bubble plot showing sub-cluster 8 was significantly enriched for previously documented lymphatic endothelial cell up valve genes including *Itga9*, *Cldn11*, and *Neo1* and Cluster 6 had down valve gene signature including *Clu* and *Adm*. The top 30 differentially expressed genes in cluster 8, both positive and negative fold change regulated, are labeled in the volcano plot(D).

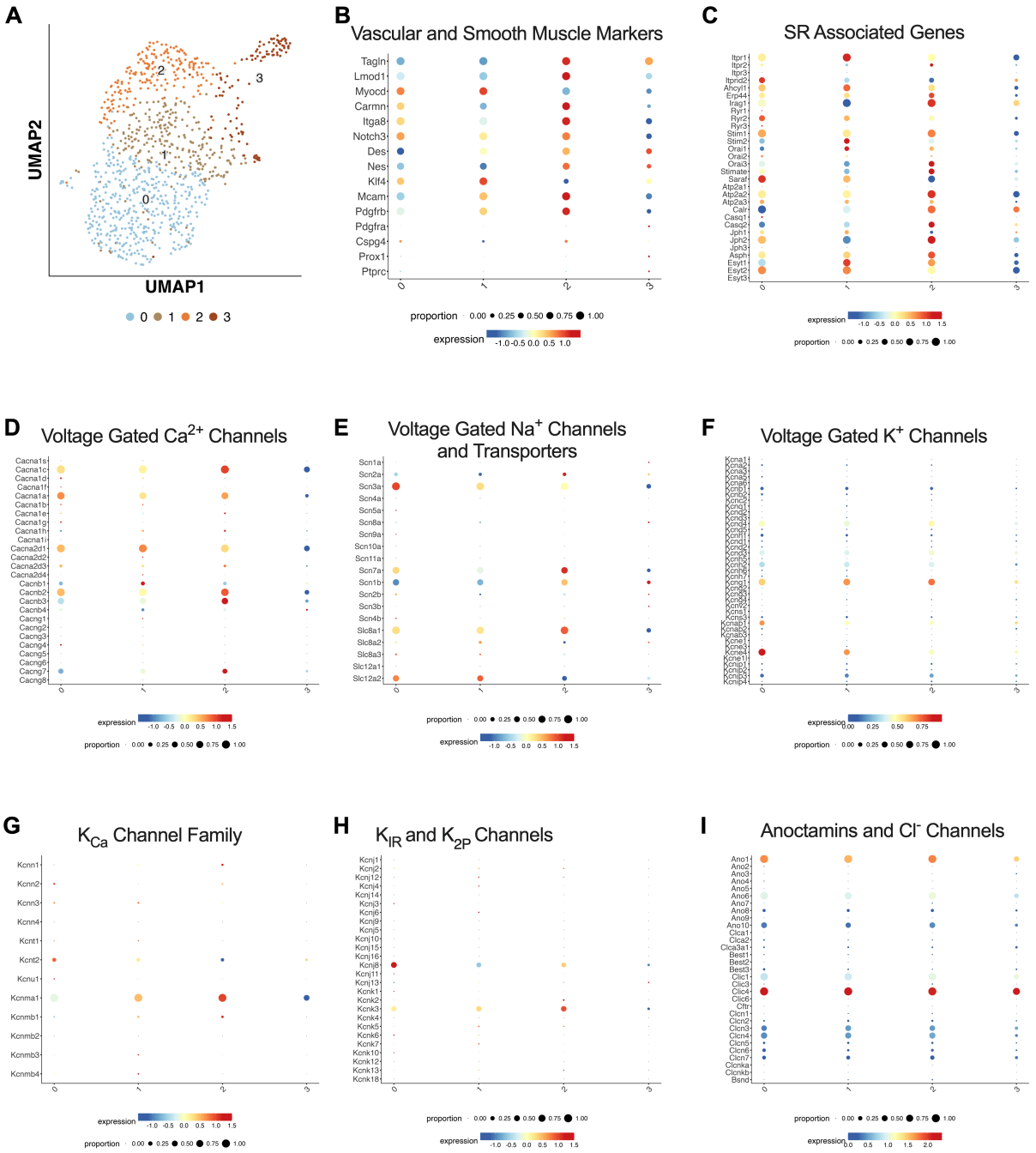

SuppFigure 5. Subclusters of IALV LMCs revealed by scRNAseq.
The LMCs could be subclustered into 4 putative subclusters (0-3) as shown in the UMAP (A). We profiled these subclusters based on their expression of the typical smooth muscle markers (B), SR associated genes (C), voltage gated Ca^{2+} channels, (D) Voltage gated Na^{+} channels and Na^{+} transporters implicated in lymphatic pacemaking (E), voltage gated K^{+} channels (F), Ca^{2+} activated K^{+} channels (G), inward rectifying K^{+} channels and two-pore domain K^{+} channels (H), and Cl^{-} channels (I).

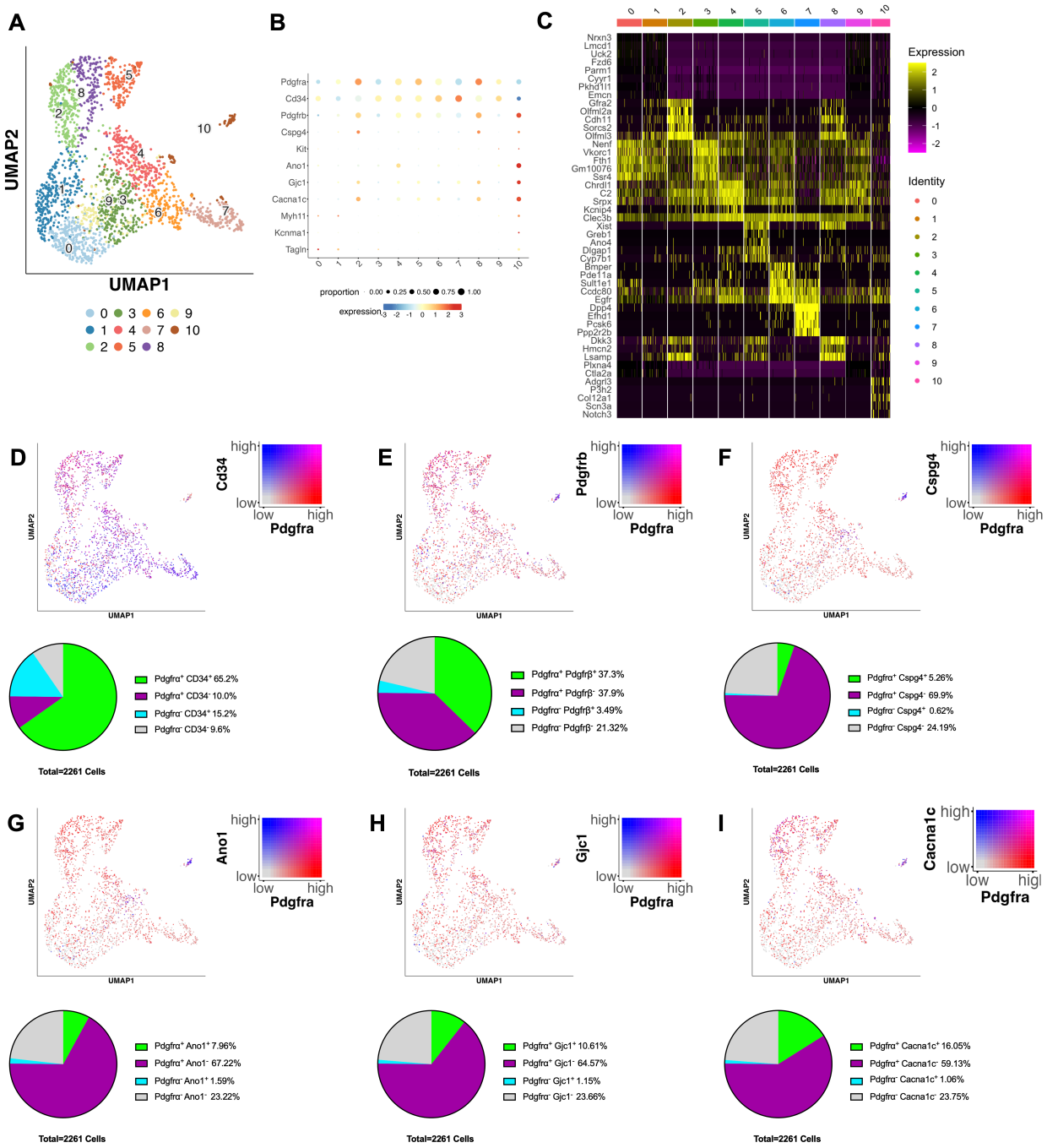

SuppFigure 6. Subclusters of IALV AdvCs revealed by scRNAseq.
AdvCs also could be further subclustered into multiple populations as shown in the UMAP (A). Bubble plot of genes used as Cre drivers and genes associated with pacemaking revealed subcluster 10 had expression of *Ano1*, *Cx45*, and *Cacna1c (CaV1.2)* but with only minimal evidence of LMC contamination as indicated by muscle signature genes *Myh11*, *Kcnma1*, and *Tagln*. C) Heatmap of the top differentially expressed genes among each of the subclusters. We assessed co-expression of *Pdgfrα* with CD34 (D) to confirm our immunofluorescence imaging (Sugg Figure 1), and assessed the co-expression of *Pdgfrα* with the pericyte markers *Pdgfrβ* (E) and *Cspg4* (F). We further assessed co-expression of *Pdgfrα* the genes linked with contractile dysfunction *Ano1* (G), *Gcj1* (H), and *Cacna1c* (I) to ensure *PdgfrαCreER*^{TM} would

target the AdvCs expressing these genes. The cyan colored slice of the pie chart indicates the minor population of cells expressing these genes that did not express *Pdgfrα.*

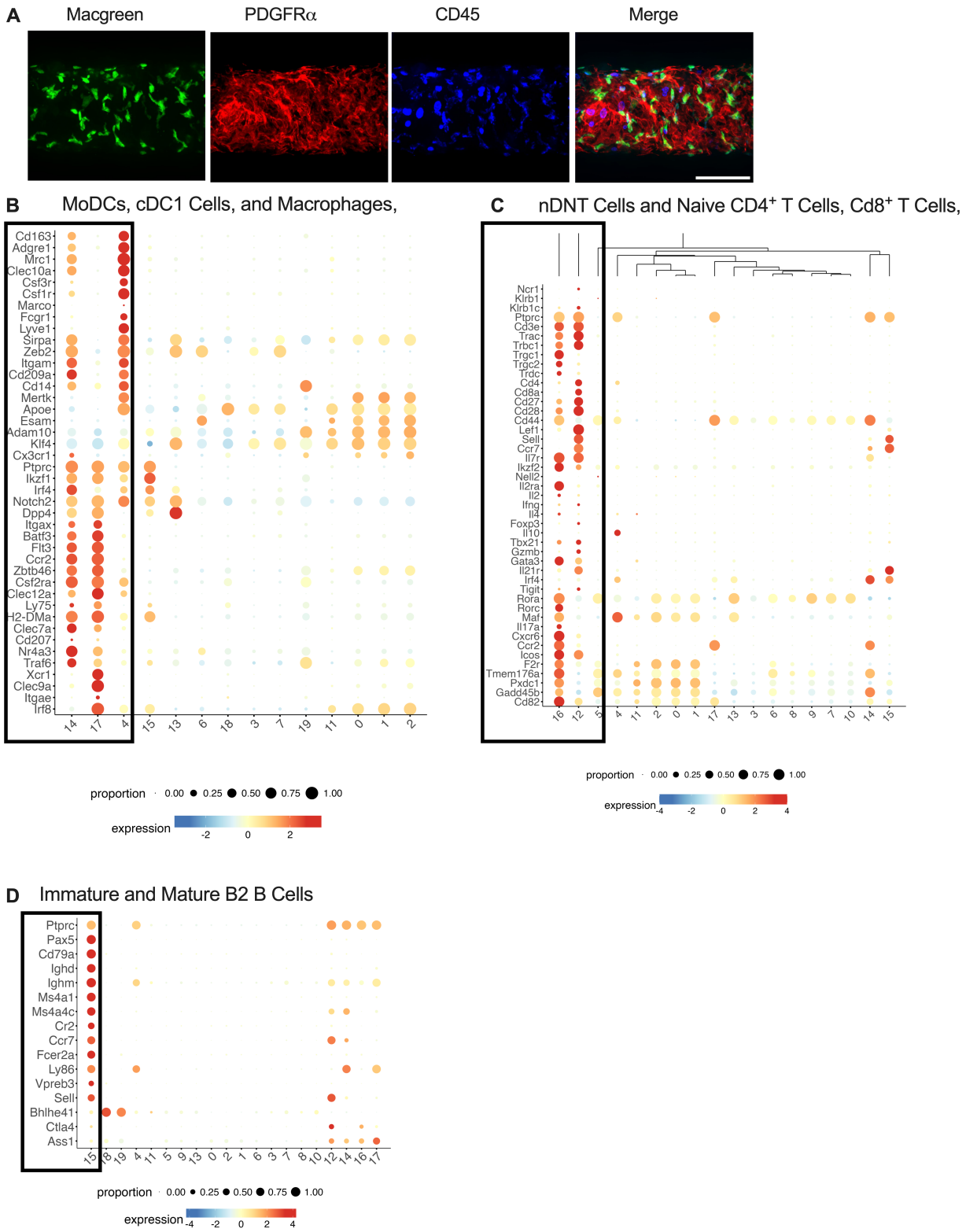

SuppFigure 7. Immune cell populations associated with the mouse IALV.
Lymphatic vessels are host to numerous immune cell populations, including monocyte, macrophage, and dendritic cell populations are revealed by immunofluorescent staining for eGFP in the "Macgreen" (Csf1r-eGFP) reporter mice (A). Staining for Pdgfrα (B) demonstrates that AdvCs are distinct from the

GFP$^+$ cells nor do they stain for the hematopoietic marker *Ptprc* (CD45) (C, D). Bubble plot of our scRNASeq analysis of IALVs revealed macrophages (cluster 4), moDCs (cluster14) and cDC1 cells (17) based off identifying gene markers (B). C) Bubble plot of T-cell markers revealed multiple populations of T cells including naive double negative T-cells (Yang et al., 2021) and naive *CD4*$^+$ and *CD8*$^+$ T-cells. A bubble plot for B-cell markers showed that cluster 15 had an expression profile for immature and mature B2 B-cells (D)(Luo et al., 2022b).

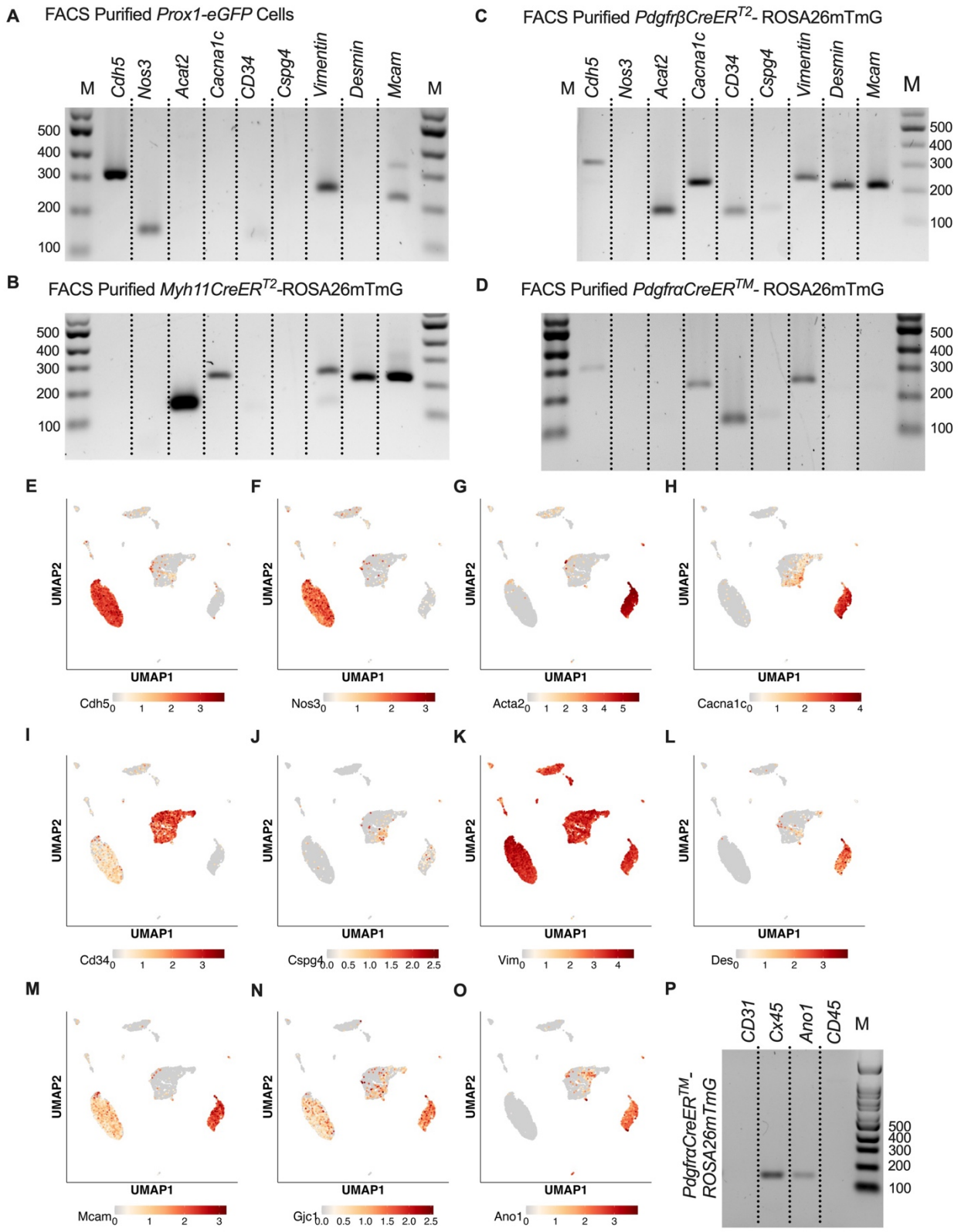

Figure 6 RT-PCR Profiling of FACs Purified Cells from iCre-ROSA26mTmG

Expanded RT-PCR profiling of genes to discriminate LECs, LMCs, and other cell types in our GFP^+ sorted cells from *Prox1-eGFP* (A), *Myh11CreER*^{T2}-ROSA26mTmG (B), *PdgfrβCreER*^{T2}-ROSA26mTmG (C), and *PdgfrαCreER*^{TM}-ROSA26mTmG (D). Dot plots for the genes assessed in A-D in our IALV scRNAseq analysis confirmed those results. In addition to a population of AdvCs expressing Cacna1c, we also noted expression of Cx45 (N) which was also observed in LECs) and Ano1 (O) in the AdvC clusters. We confirmed this expression using GFP^+ cells sorted from *PdgfrαCreER*^{TM}-ROSA26mTmG IALVs for RT-PCR (P) and ruled out hematopoietic or LEC contamination. All RT-PCRs were performed 2-4 times for each gene over each sorted cell population collected from different mice.

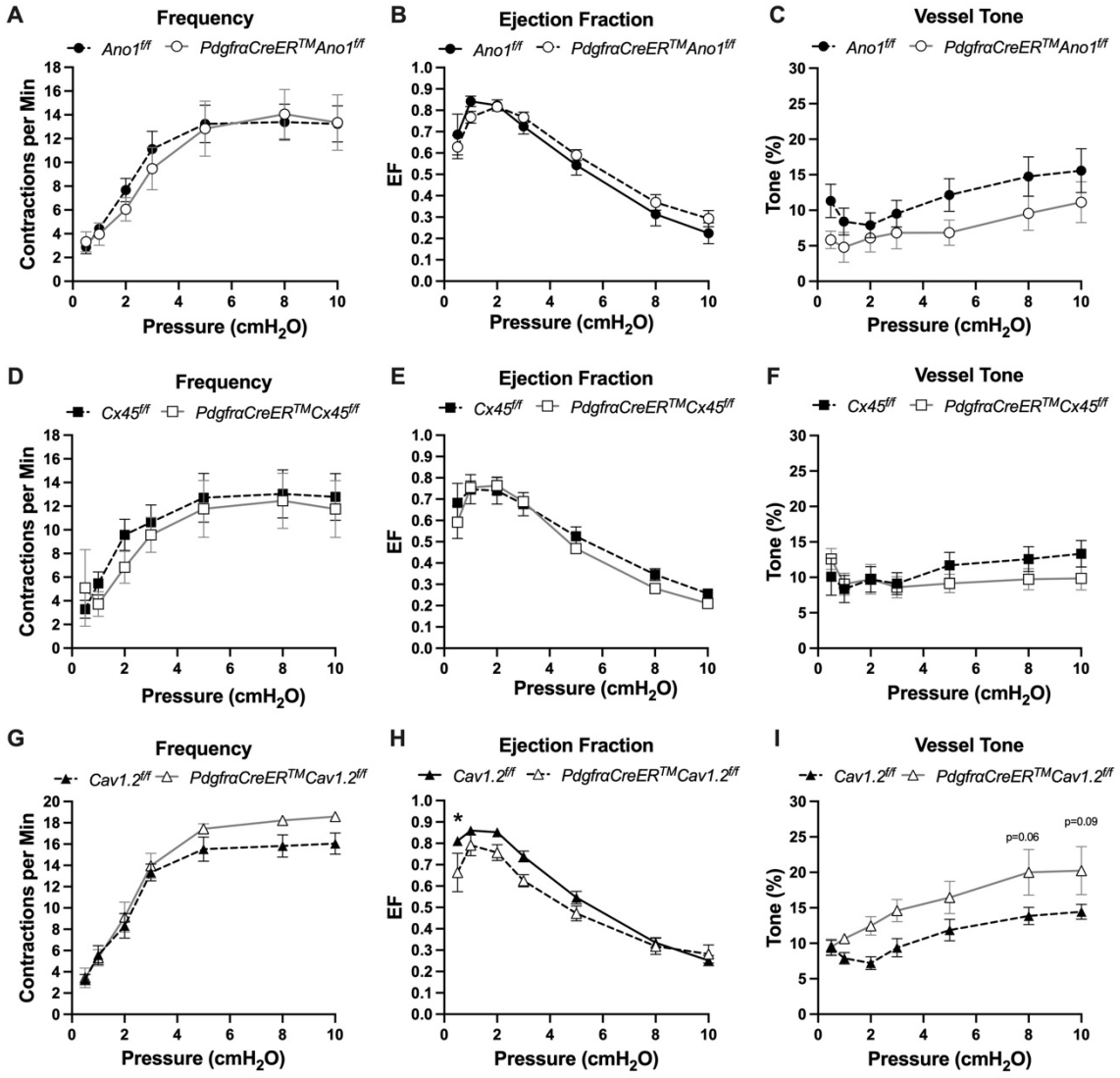

Figure 7 Isobaric contractile Assessment of popliteal cLV from *PdgfrαCreER^{TM}* driven deletion of *Ano1*, *CX45*, and *CaV1.2*

Summary of the contractile parameters recorded from popliteal cLVs in *PdgfrαCreER^{TM}-Ano1*$^{fl/fl}$, *PdgfrαCreER^{TM}-Cx45*$^{fl/fl}$ mice, *PdgfrαCreER^{TM}-Cav1.2*$^{fl/fl}$ mice. Contraction frequency (A, D, G), ejection fraction (B, E, H), and vessel tone (C, F, I) were assessed. No statically significant differences observed in cLVs isolated from *PdgfrαCreER^{TM}-Ano1*$^{fl/fl}$ and *PdgfrαCreER^{TM}-Cx45*$^{fl/fl}$ mice across these three parameters. Mean and SEM shown, n=6 popliteal vessels from 3 mice *PdgfrαCreER^{TM}-Ano1*$^{fl/fl}$ mice and n=10 popliteal vessels from 6 mice *Ano1*$^{fl/fl}$ mice. Mean and SEM shown, n=5 popliteal vessels from 3 mice *PdgfrαCreER^{TM}-CX45*$^{fl/fl}$ mice and n=8 popliteal vessels from 11 mice *CX45*$^{fl/fl}$ mice. Mean and SEM shown, n=6 popliteal vessels from 3 mice *PdgfrαCreER^{TM}-Cav1.2*$^{fl/fl}$ mice and n=9 popliteal vessels from 20 mice *Cav1.2*$^{fl/fl}$ mice. The contractile data from control *Cav1.2*$^{fl/fl}$ vessels was previously published but was separated by sex (Davis et al., 2022) while they are combined here. * Denotes significance at $p < 0.05$ which $0.10 > p > 0.05$ are reported as text. Normalized contraction amplitude, fractional pump flow, end diastolic diameter can be found in SuppFigure 8.

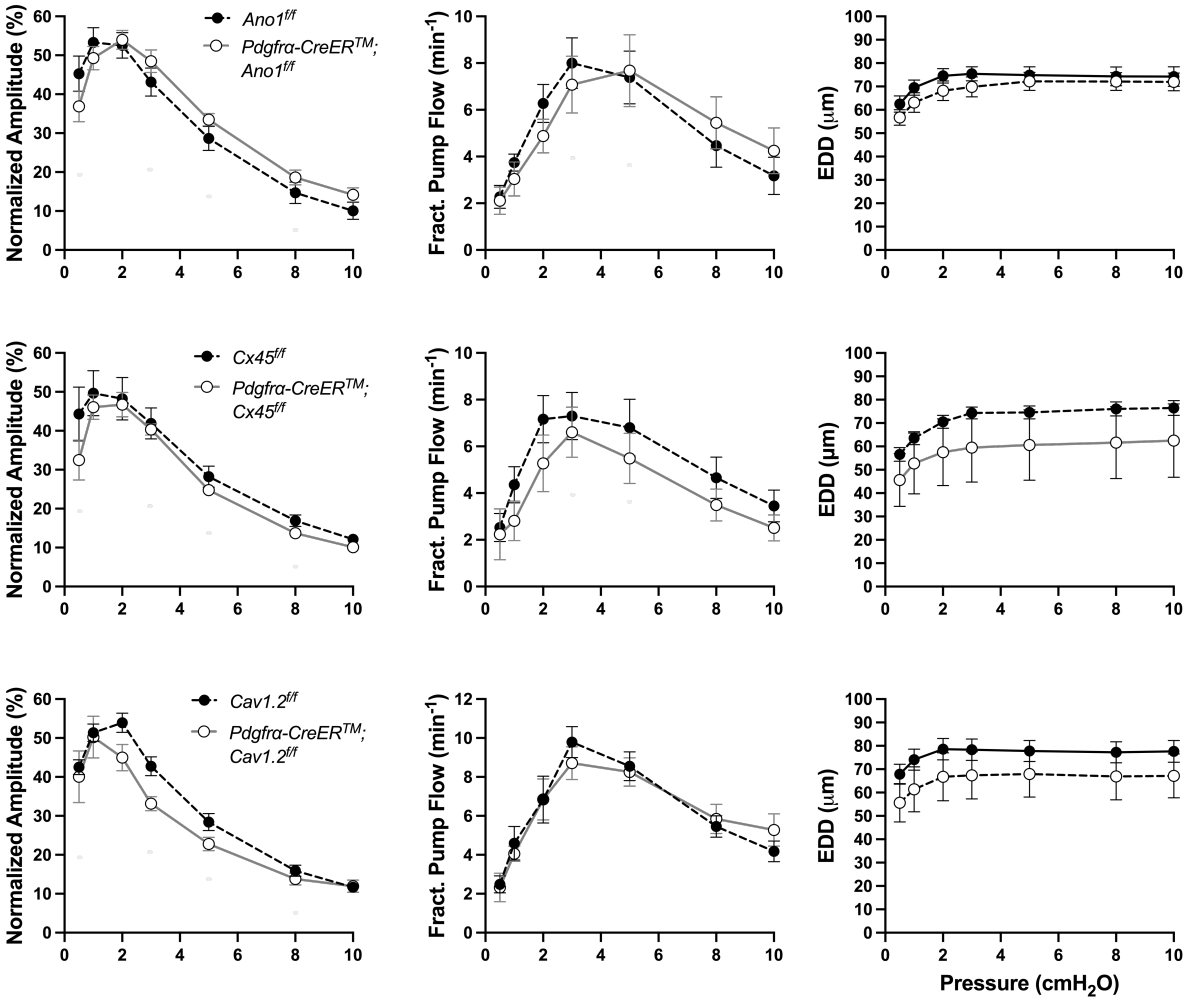

SuppFigure 8 Contractile indices from isobaric myography on cLVs from *PdgfrαCreER^{TM}* driven deletion of *Ano1*, *CX45*, and *CaV1.2*

Summary of the contractile parameters recorded from popliteal cLVs in *PdgfrαCreER^{TM}-Ano1*$^{fl/fl}$, *PdgfrαCreER^{TM}-Cx45*$^{fl/fl}$ mice, *PdgfrαCreER^{TM}-Cav1.2*$^{fl/fl}$ mice. No differences in normalized contraction amplitude (A, D, G), fractional pump flow (B, E, H), or end diastolic diameter (C, F, I) were observed. The contractile data from control *Cav1.2*$^{fl/fl}$ vessels was previously published but was separated by sex (Davis et al., 2022) while they are combined here.

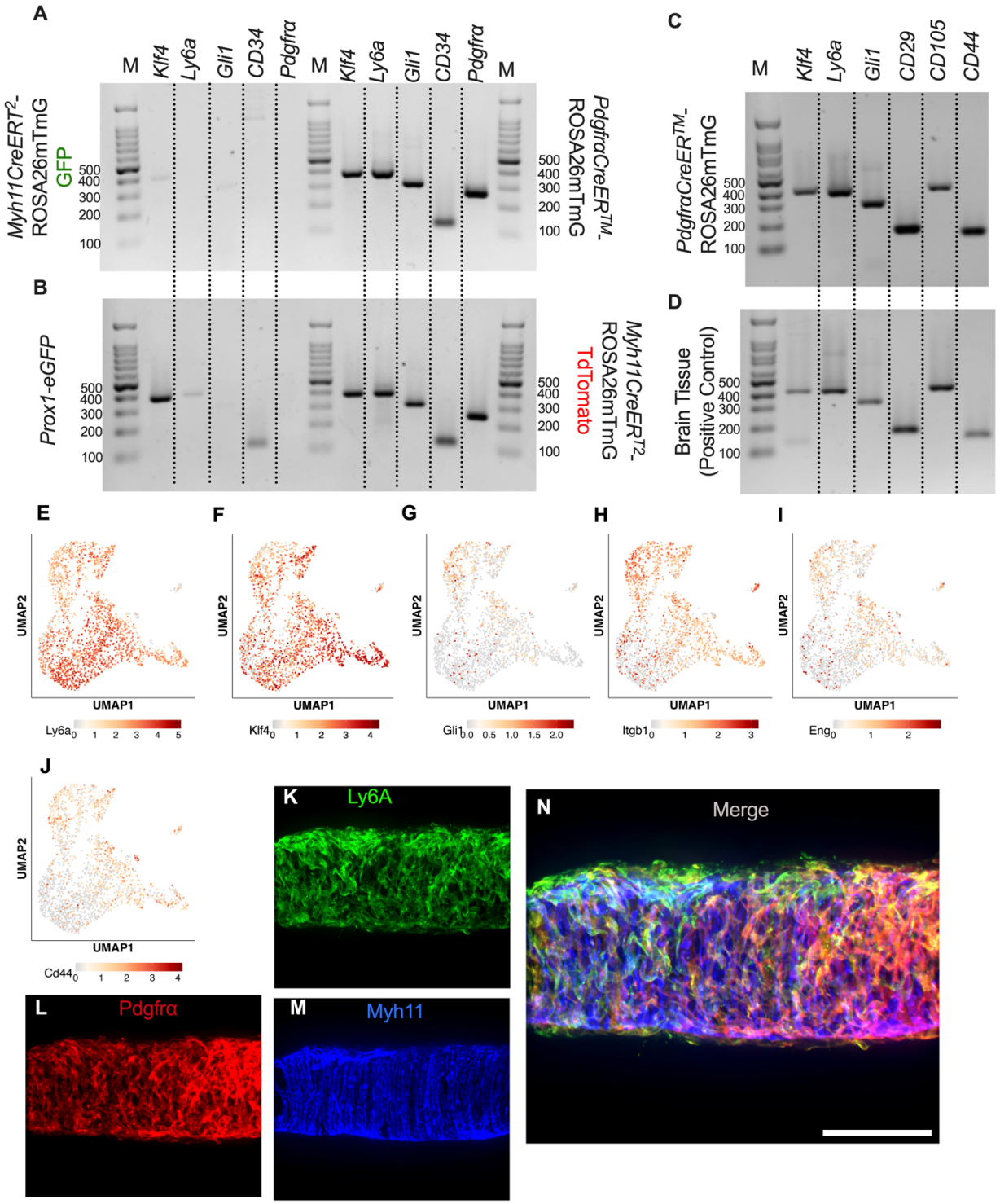

SuppFigure 9 PDGFRα AdvCs Include Multipotent Cell

Representative RT-PCR results profiling purified GFP$^+$ cells purified from IALVs isolated from *PdgfrαCreER*TM-ROSA26mTmG via FACS. PDGFRα cells expressed the multipotent markers Klf4, Sca1, Gli1, CD29, CD105, and CD44 (A) with total brain cDNA serving as a positive control (B). Representative RT-PCR results showing lack of expression of some of these markers in the GFP$^+$ cells purified from *Myh11CreER^{T2}*--ROSA26mTmG (C) or *Prox1-eGFP* mice, in contrast to the RFP$^+$ population from

Myh11CreER^{T2}--ROSA26mTmG mice (D). RT-PCRs were repeated at least 2 times from separate purified cells populations from different mice. Dot plots of only the AdvCs cluster highlights populations of cells that express genes associated with multipotency such as Ly6a (E), Klf4 (F), Gli1 (G), Itgb1 (H, CD29), Eng (I, CD105), CD44 (J). Expression of protein for Ly6a was confirmed with immunofluorescence. Representative max projections of IALVs stained for Sca1 (K), PDGFRα (L), Myh11 (M) and the corresponding merged file (N). Scale bar is 100 μm.

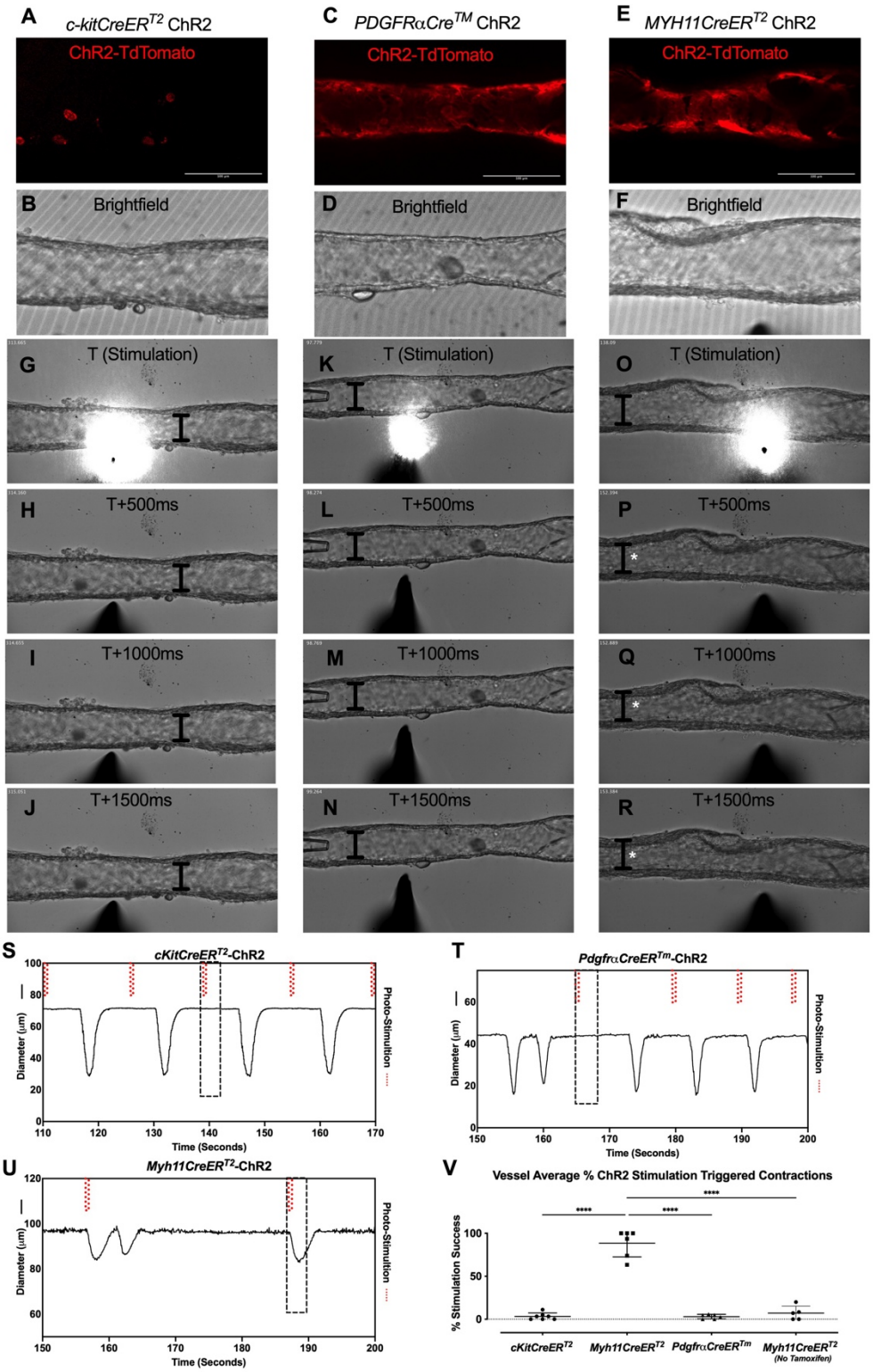

Figure 8 ChR2-Mediated Depolarization Only in LMCs Triggers Contraction
Representative max projections of tdTomato-ChR2 signal in popliteal cLVs isolated from *cKitCreER*^{T2}-ChR2-tdTomato (A), *PdgfrαCreER*^{TM}-ChR2-tdTomato (C), and *Myh11CreER*^{T2}- ChR2-tdTomato (E) with their corresponding brightfield image (B, D, F) respectively. Time-lapse brightfield images every 0.5 s starting at stimulation t=0 for *cKitCreER*^{T2}-ChR2-tdTomato (G-J), *PdgfrαCreER*^{TM}-ChR2-tdTomato (K-

N), and *Myh11CreER*^{T2}- ChR2-tdTomato (O-R). The I bar denotes the inner diameter at t=0 over time and white asterisks denote the contraction. Representative diameter trace for the popliteal cLV demonstrate spontaneous contractions with the dotted boxes indicating the optical stimulation event in the respective brightfield images of the time lapse images. Isolated cLVs from *cKitCreER*^{T2}-ChR2-tdTomato (S), *PdgfrαCreER*^{TM}-ChR2-tdTomato (T), and *Myh11CreER*^{T2}- ChR2-tdTomato (U) were stimulated with light pulses (red dashed lines) and the summation of contraction triggering for each genotype (V). Mean and SEM are shown, **** denotes $p<0.0001$. Contraction recorded from at least 6 popliteal cLVs from 3 mice per genotype.

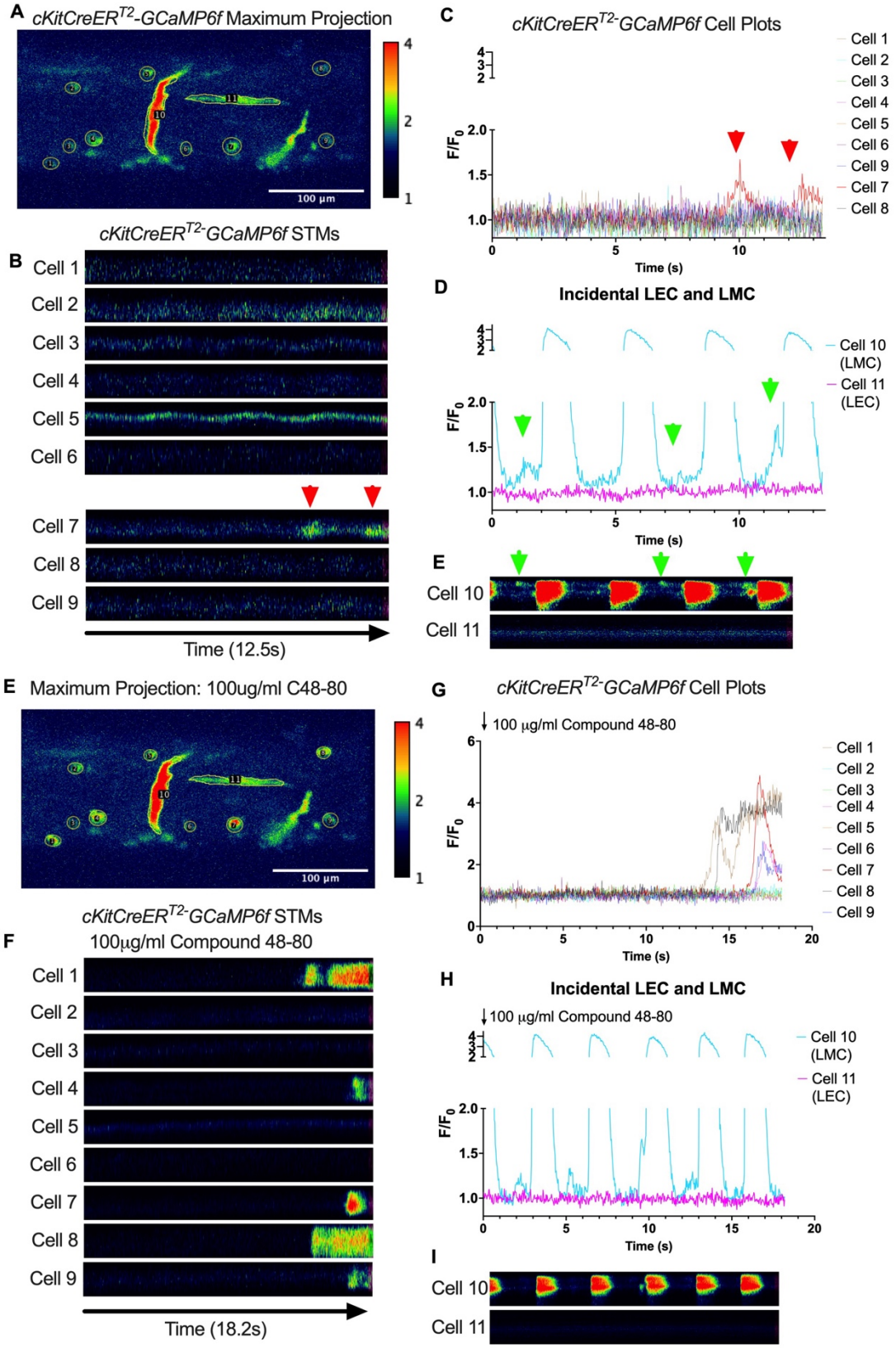

Figure 9 *cKitCreER*T2 Drives GCaMP6f Expression Primarily in Mast Cells in Mouse IALVs

Representative max projection of GCaMP6f signal over time in an IALV isolated from a *cKitCreER*^{T2}-GCaMP6f mouse with ROI indicated around individual cells, primarily large ovoid cells, but also including a circumferential LMC (Cell10) and a horizontal LEC (Cell 11). Of cells 1-9, only cell 7 had any Ca^{2+} activity (red arrows) during the recording time as indicated by the STMs from each ROI (B) and their normalized F/F_0 plots in (C). In contrast, the LMC in ROI 10 had both rhythmic global Ca^{2+} events (D) that spanned the cell axis (vertical axis) in the STM (E) in addition to localized Ca^{2+} events intervening the time between global events (green arrows). Representative max projection of GCaMP6f signal over time after stimulation with C48-80 (F) with many large ovoid cells displaying long lasting global Ca^{2+} events (G, H) while not immediately affecting the LMC Ca^{2+} dynamics (I, J).

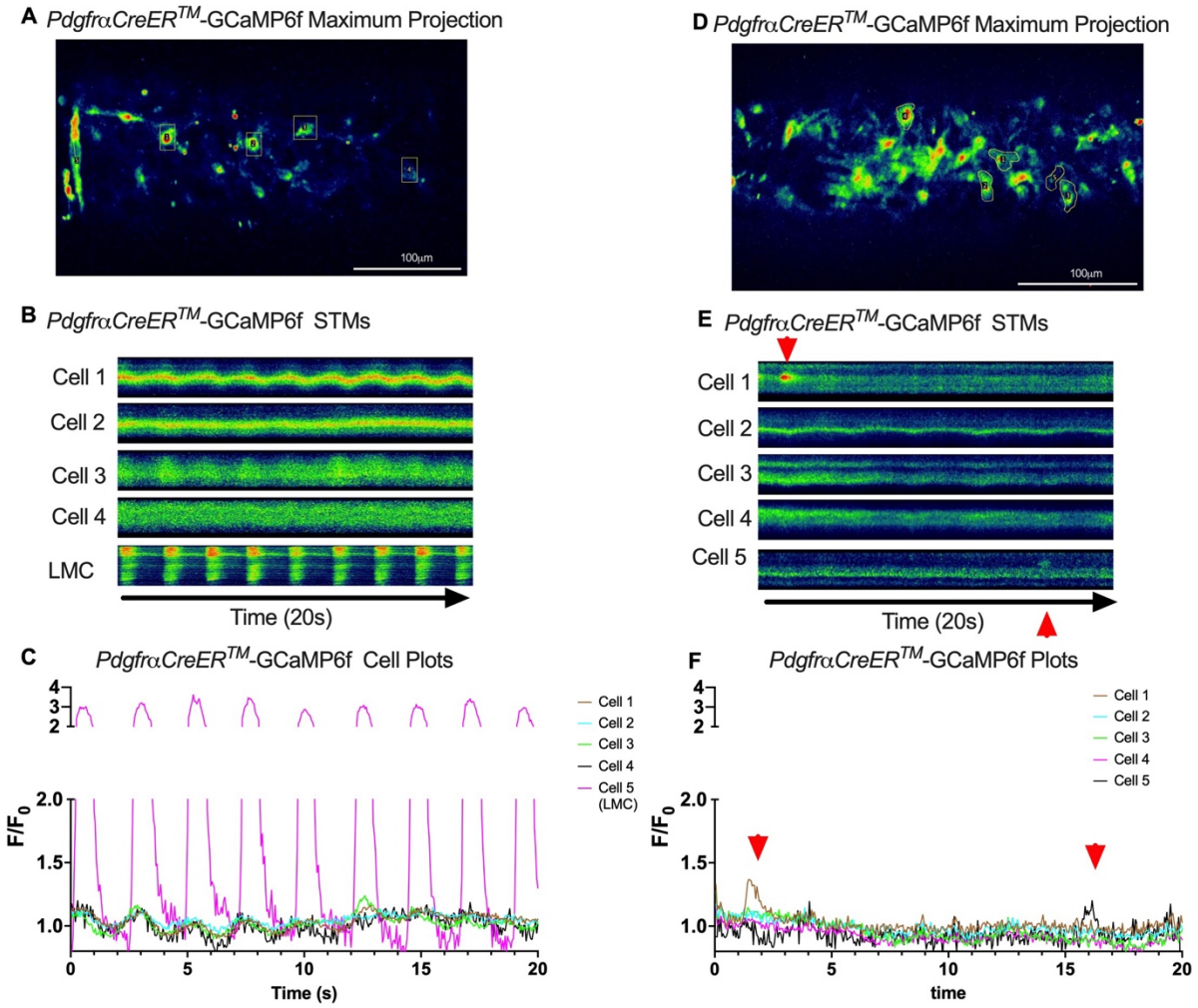

Figure 10 Lack of coordinated Ca^{2+} Activity Across Contraction Cycle in PDGFRα Cells
Representative max projections of GCaMP6f signal over time in an IALVs isolated from *PdgfrαCreER^{TM}*-GCaMP6f mice (A, D). ROIs were made around cells and GCaMP6f recorded over time to generate the corresponding STMs (B, E) for each cell and plots (C, F) respectively. Once again, incidental recombination occurred in a LMC which displayed rhythmic Ca^{2+} flashes (C) while the slight undulation in the other cells is due to movement artifact (B). Red arrows indicate the limited local Ca^{2+} activity observed in two cells from a *PdgfrαCreER^{TM}*-GCaMP6f IALV.

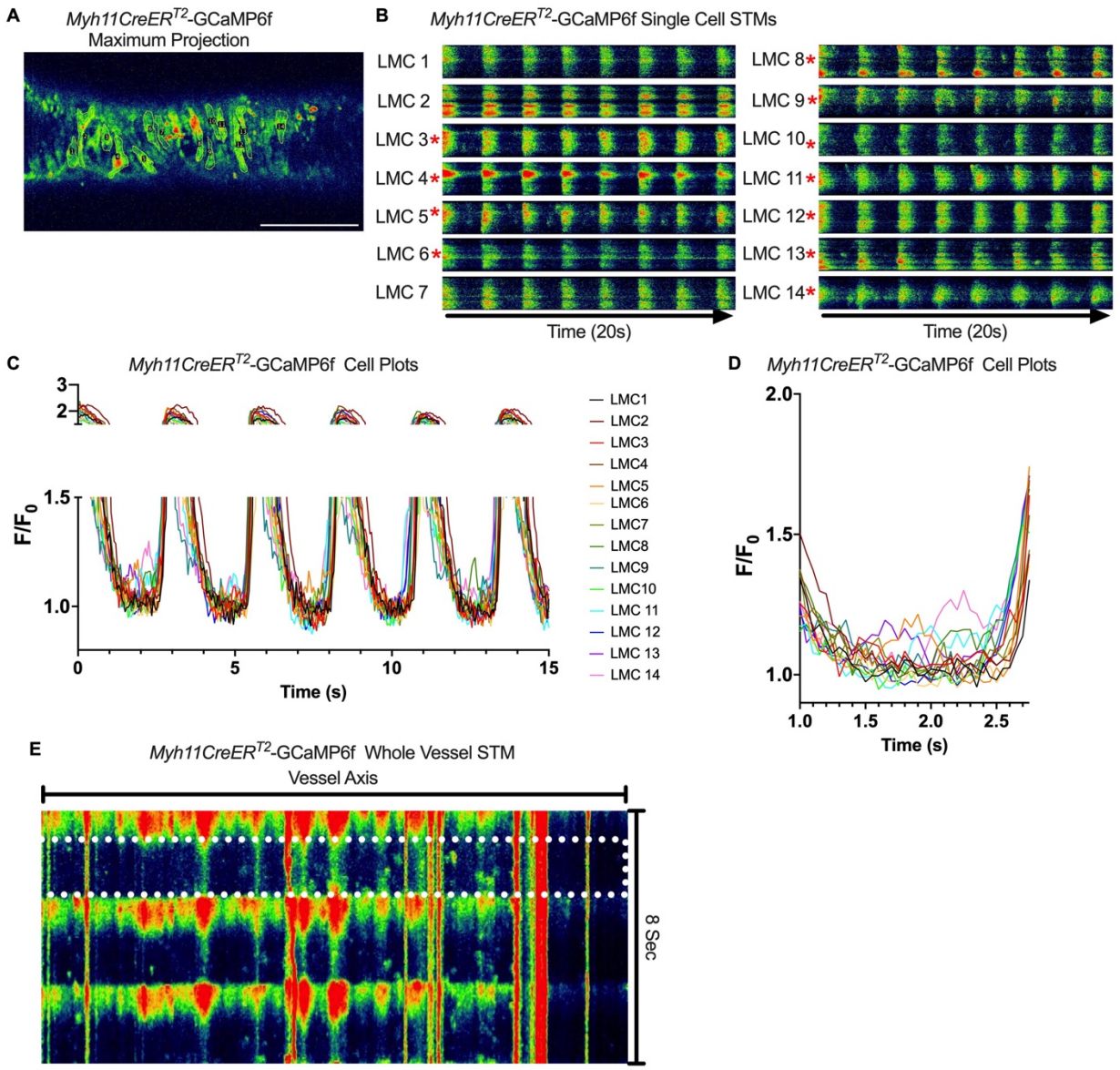

Figure 11 Heterogeneous Diastolic Ca^{2+} Transient Activity in LMCs
Representative max projections of GCaMP6f signal over time in an IALVs isolated from *Myh11CreER^{T2}*-GCaMP6f mice (A). LMCs were outlined with ROIs to assess GCaMp6F signal over time. Rhythmic global flashes (B) were entrained across all the LMCs in the FOV (C) with many cells exhibiting diastolic Ca^{2+} release events. Cells exhibiting at least one diastolic Ca^{2+} event, within the context of our focal plane constraints, over the recorded time were denoted by the red asterisks. The plot in (D) magnifies the first diastolic period, seconds 1-3 of C to assist in visualizing the lack of coordination of the diastolic events. (E) Max projection of the pseudo-linescan analysis across the axis of the vessel to highlight diastolic Ca^{2+} transients in all cells in the field of view and their lack of coordination across the cells (x-axis). The white dotted box shows the first diastolic period plotted in (D).

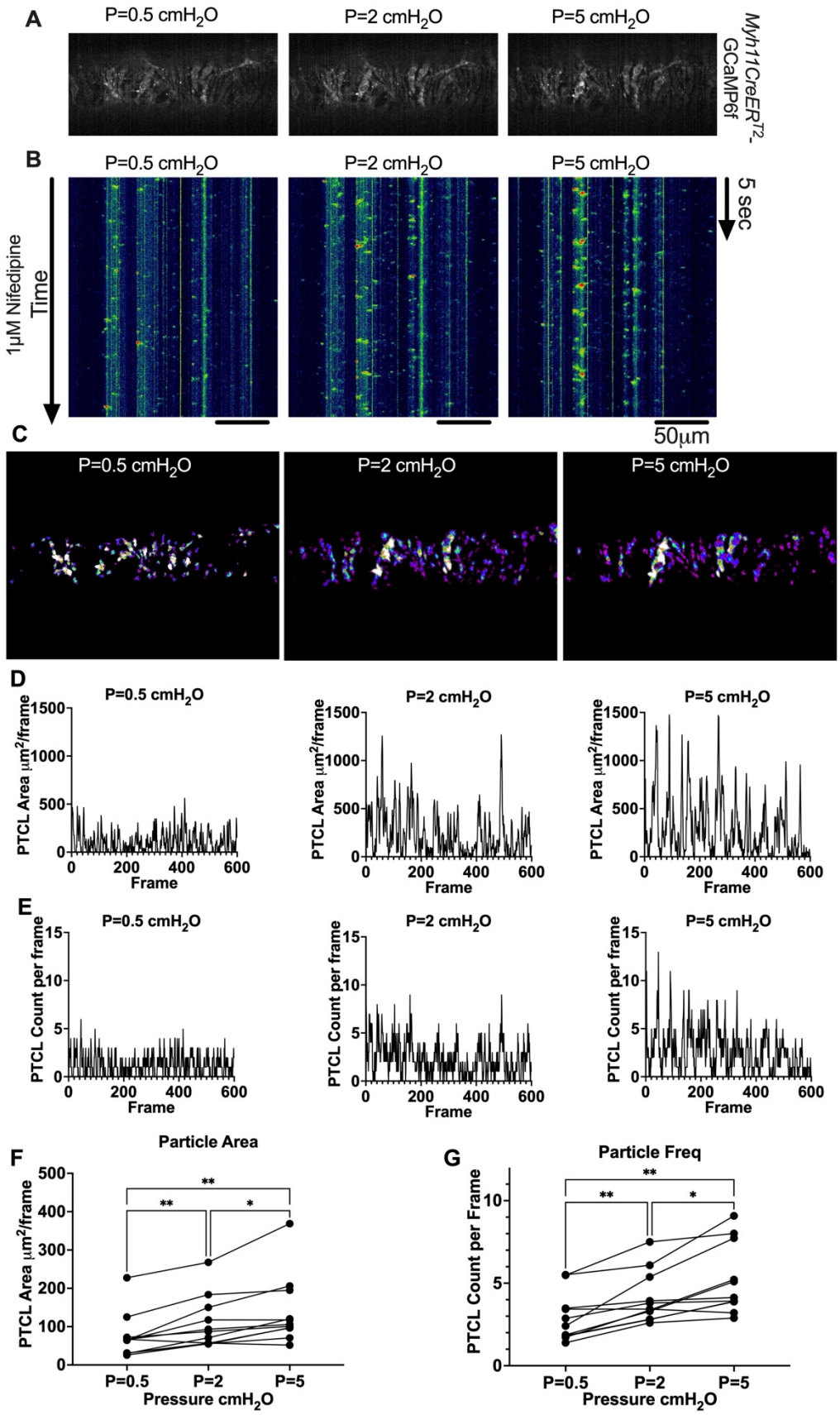
A
P=0.5 cmH2O
P=2 cmH2O
P=5 cmH2O
Myh11CreERT2-GCaMP6f
B
P=0.5 cmH2O
P=2 cmH2O
P=5 cmH2O
5 sec
1μM Nifedipine
Time
50μm
C
P=0.5 cmH2O
P=2 cmH2O
P=5 cmH2O
D
P=0.5 cmH2O
P=2 cmH2O
P=5 cmH2O
PTCL Area μm2/frame
Frame
E
P=0.5 cmH2O
P=2 cmH2O
P=5 cmH2O
PTCL Count per frame
Frame
F
Particle Area
PTCL Area μm2/frame
Pressure cmH2O
P=0.5
P=2
P=5
G
Particle Freq
PTCL Count per Frame
Pressure cmH2O
P=0.5
P=2
P=5

Figure 12 Pressure Dependency of Mouse LMC Diastolic Ca^{2+} Transients
Representative max projection of GCaMP6f signal over 20 s in an IALVs isolated from *Myh11CreER^{T2}*-GCaMP6f mice in the presence of the L-type blocker nifedipine (1μM) (A) pressurized to 0.5 cmH_2O, 2 cmH_2O, 5 cmH_2O. The local diastolic Ca^{2+} transients persist in the presence of nifedipine and increase with increasing pressure as demonstrated in the whole vessel STMs (B). Particle occurrence maps highlight the Ca^{2+} activity in each LMC as pressure is raised (C). Representative particle analysis plots for particle area (D) and particle counts/frame at each pressure (E). Summary files for particle area (F) and count /frame (G0. * Denotes $p<0.05$, Mean and SEM shown with n=12 separate IALVs from 8 MYH11-CreER^{T2}-GCaMP6f

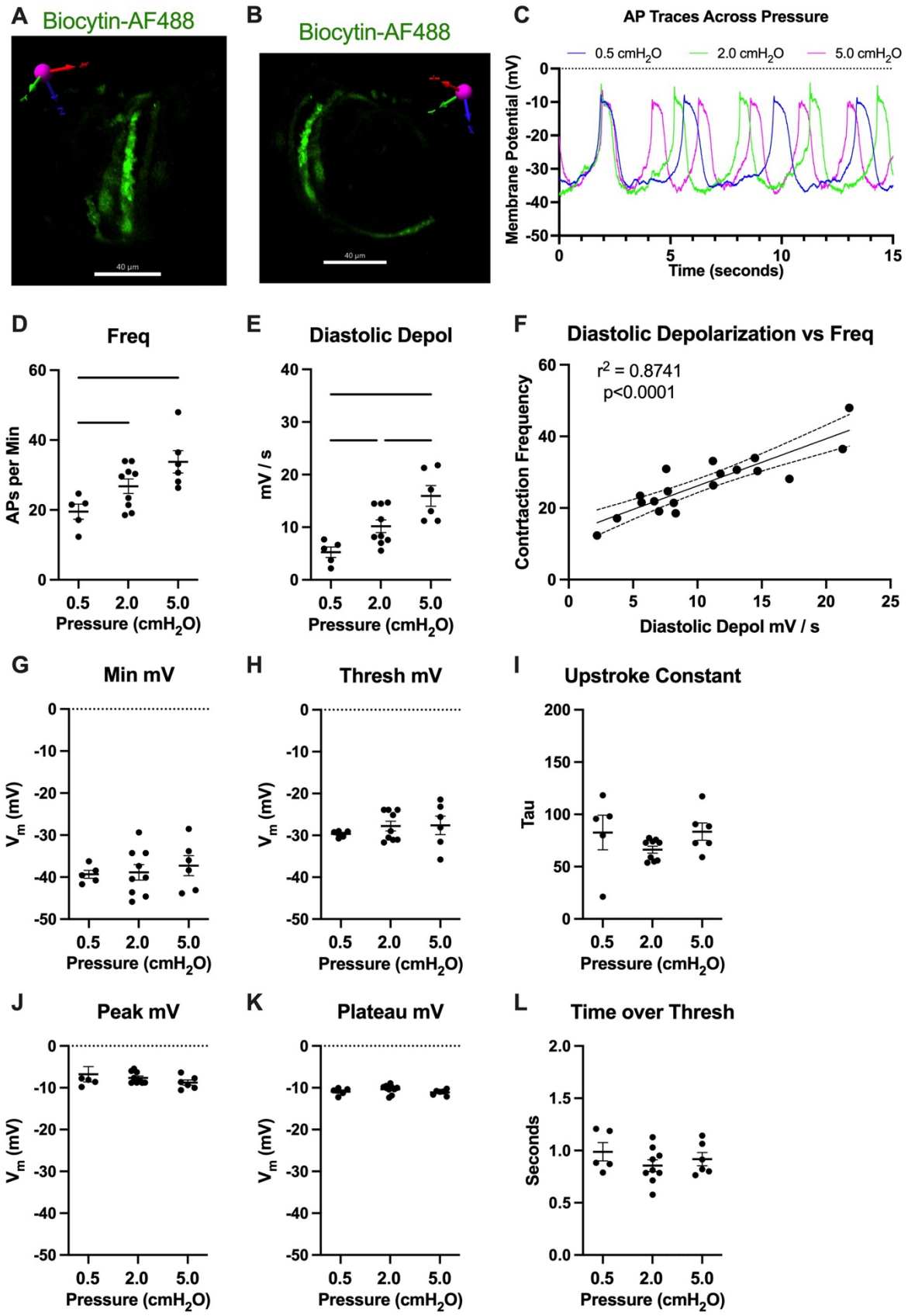

Figure 13 Pressure Dependent Diastolic Depolarization in LMCs

Intracellular recordings of LMC action potentials (AP) were confirmed by loading (greater than 10minutes) the impaling electrode with 1M KCl 100ug/ml AF488-Biocytin while recording APs followed by imaging on a spinning disk confocal microscope. 3D reconstruction of the z-stack confirmed the circumferential pattern of the impaled LMC that was strongly labeled by AF488-Biocytin (A, B), which also labeled neighboring LMCs, likely through gap junctions as AF488-Biocytin is <1kDa. In a separate set of experiments APs were recorded at 3 different pressures, 0.5 cmH_2O, 2 cmH_2O, and 5cmH_2O. We plotted the representative recordings from 1 cell at each pressure (C). AP frequency was significantly increased with pressure (D) as was the diastolic depolarization rate. Plotting the AP frequency and diastolic depolarization rate from all recordings at each pressure (F) highlights the significant effect diastolic depolarization rate has on the AP frequency. Minimum membrane potential (G), threshold membrane potential of AP initiation (H), upstroke constant (I), peak membrane potential (J), plateau membrane potential (K), and time over threshold (L) are also reported, although not significant.